Magnetic Skyrmions and Topological Insulators for Spintronics Applications

Hamed Vakili

A Dissertation Presented to the
Graduate Faculty of the
University of Virginia
in Candidacy for the Degree of
Doctor of Philosophy

Department of Physics

University of Virginia
April 2022

Committee Members:
Avik W. Ghosh
Diana Vaman
Gia Wei Chern
Prasanna Balachandran

Abstract

To increase the memory storage and processing capabilities of computers, the density of transistors need to be scaled up. One of the main bottlenecks of increasing the density is the heat generation and energy consumption of the devices, which limit how small we can go. One alternative is to use spins instead of electrons to process and store information. The field of using spins for computing is known as spintronics. However, there are challenges in generating spin current and high density spintronics devices. Topological phases of matter offer exciting properties that can be used in spintronics and address some of the challenges.

We develop and use a range of tools to cover the analysis of the devices going from material level to transport and dynamics to circuit level analysis. At the material level we use ab-initio results as an input for Non Equilibrium Green Function (NEGF) formalism and Landau Lifshitz Gilbert (LLG) equation to study quantum transport and magnetodynamics, which in turn act as an input for circuit level analysis.

Using LLG, we study the magnetic skyrmions, which are topological quasiparticles in magnetic moment space. We propose and investigate the underlying physics of a type of self-focusing skyrmions and their possible applications as reconfigurable logic units. Also, we propose an unconventional application for skyrmion for temporal computing using the dynamical properties of skyrmions. We design and study the control circuit and its energy consumption, going all the way from LLG calculations

to circuit simulation and compact modeling. In addition, to control and tune the motions of skyrmions, we develop a numerical tool based on mathematical models to investigate the positional lifetime of skyrmions in the presence of notches and imperfections of their host material. We turn to topological insulators (TI) as an option to generate spin current. We use tight binding models fitted to ab-initio calculations from literature as our toy model and use it in the NEGF formalism to simulate the quantum transport of TI channels. Finally, we study FM/TI heterostrucres and propose a device based on their reciprocal interaction. We solve NEGF-LLG equations self consistently and combine it with Fokker-Planck equations to estimate the device performance.

Acknowledgements

For this long journey, I want to express my gratitude to my advisor, Prof. Avik W. Ghosh, for giving me the opportunity to research and develop my ideas and for the guidance he provided me throughout. I also want to thank Prof. Diana Vaman and Prof. Gia Wei Chern for serving on my yearly research review and defense committee and providing me with constructive feedback. I have taken courses from both of them and was impressed by their knowledge and devotion to teaching. I also thank Prof. Prasanna Balachandran for agreeing to be on my defense committee. I would like to thank Prof. S. Joseph Poon, Mark Stiles, and Prof. Mircea Stan for their dedication to research and for sharing with me their unique scientific intuition and viewpoints. I also appreciate their insightful feedback on my search for post doctoral positions. I would like to also thank all of my co-authors for helping me with my research. Without them, this thesis would not have existed.

I want to thank my fellow group members for their companionship and feedbacks. Finally, but most importantly, I would like to thank my family. I thank my parents for instilling in me my love of science. I thank my grandfather for showing me the joy of creative endeavors.

Table of Contents

List of Figures

List of Tables

List of Acronyms

DW	Domain Wall
FM	Ferromagnet
LLG	Landau Lifshitz Gilbert
MEP	Minimum Energy Path
NEGF	Non Equilibrium Green Function
SOT	Spin Orbit Torque
STT	Spin Transfer Torque
TI	Topological Insulator
TSS	Topological Surface State
3DTI	Three Dimensional Topological Insulator

Chapter 1

Introduction

Digital electronics has been driven for several decades by sustained hardware scaling and Moore's law. With the recent slowdown in advances in Complementary Metal Oxide Semiconductor (CMOS) hardware and rapid growth of software, along with the migration from cloud computing towards edge devices, there is a strong impetus to re-examine the limits of computing. In conventional Von Neumann computer architecture, the processor needs to access data stored in separate memory banks in order to perform logic operations. Unfortunately, the speed of memory scaling ($1.1\times$ in every two years) has not kept up with the drastically increased speed of processor scaling ($2\times$ in every two years). This increasing gap between memory and processor performance, the so-called *memory wall problem*, is considered one of the main bottlenecks to increasing computer performance.

Magnet-based non-volatile memory has a rich history, with field-switched magnetic RAMs (MRAMs), spin-transfer and spin orbit torque based RAMs (STT and SOT-RAMs) now commercialized [3, 4, 5]. In magnetic memory, the different directions of magnetization can be used to store data as digital bits (e.g., up equals one, down is zero). The energy required to switch a magnet is fairly low. However, energy is dissipated in the overhead/control circuitry due to the need for currents generated to create the switching fields. Field switched MRAMs are hard to scale because the scaling of the drive circuit requires increasing current densities with increasing energy dissipation. STT-RAMs have better-scaling properties, as the switching is due to spin-polarized currents directly injected into a magnet across the oxide of a magnetic tunnel junction (MTJ).

STT and SOT-RAMs has garnered a lot of attention both from academia and industry due to its compatibility with CMOS processes and voltages, zero standby leakage (non-volatility), scalability, high endurance and retention time, and overall reliability. In fact, STT-RAM has evolved from the discovery of giant magnetoresistance in the late 1980s [6, 7] and theoretical ideas soon after [8, 9, 10], to a dark horse in the 2000s [11, 12] to becoming now a commercially viable candidate for on-chip cache memory [13], with both the integration density of DRAM and comparable performance to SRAM[14].

Recent experimental observation of magnetic skyrmions and the new class of topological materials known as three dimensional topological insulators (3DTI), has paved a path forward in addressing some of the challenges and fundamental limitations of STT and SOT RAMs. Skyrmions have similar properties to magnetic domains but can be smaller and operate faster, which means they can replace magnetic domains in the devices under the right circumstances. The 3DTI materials have been shown to host metallic surface states which are completely spin polarized. The spin current generated by the surface of 3DTI can be used for STT and SOT RAMs to manipulate the magnetization directions.

1.1 Dissertation Organization

In this dissertation, we first focus on magnetic skyrmions. We look at their fundamental physics and their dynamic properties. We introduce the Landau-Lifshitz-Gilbert (LLG) equation for studying magnetodynamics. Afterward, we look at possible device concepts for memory and logic applications based on skyrmions. Finally, we look at the skyrmion-based devices' limitations and propose possible workarounds. We develop the string method to achieve skyrmion's minimum energy path (MEP) between two possible local minimums. We employ the calculated MEP to study the positional stability of skyrmions in the context of skyrmion racetrack devices. After skyrmions, we focus on 3DTIs and their applications. In particular, we study FM/3DTI heterostructures and propose a RAM based on such a device. We introduce Non-Equilibrium-Green-Function (NEGF) formalism to study the quantum transport in the 3DTI channel and combine it with LLG and solve the NEGF-LLG self-consistently to analyze the device performance.

Chapter 2

Magnetic Skyrmions

Magnetic Skyrmions are topological quasi-particles that exist in ferromagnets (FM), ferrimagnets (FiM) and antiferromagnets (AFM). To see what the 'topological protection' means and how they are formed, we first need to look at the energy profile of magnets. After, we look at the dynamics of skyrmions and how it relates to the topology. Finally, we discuss the computational tools to simulate the magnetic skyrmions. This chapter is partially reproduced from Ref. [1] co-authored with Jun-Wen Xu, Wei Zhou, Mohammad Nazmus Sakib, Md Golam Morshed, Timothy Hartnett, Yassine Quessab, Kai Litzius, Chung T. Ma, Samiran Ganguly, Mircea R. Stan, Prasanna V. Balachandran, Geoffrey S. D. Beach, S. Joseph Poon, Andrew D. Kent and Avik W. Ghosh

2.1 Energy and Effective Fields

The skyrmions are a result of the competition between different energy terms in the magnetic system. There are several contributions to the energy like the exchange energy, the anisotropy energy, the Zeeman energy and the demagnetization energy. The evolution of the magnetization in the system is then described by the change of these energy terms, which are captured by the effective fields. In this section, we discuss these energy terms and their corresponding effective fields.

Exchange Energy

The exchange energy gives an approximate representation of the quantum mechanical exchange interaction between electrons of neighboring sites in the crystal lattice. Considering only nearest neighbours, it can be written as (also called the Heisenberg model):

$$E_{ex} = -J \sum_{<i,j>} \mathbf{S}_i.\mathbf{S}_j \tag{2.1}$$

Where the summation is taken over all the neighboring sites. J is the exchange integral. $\mathbf{S}_i$ is the spin of the atomic site i. For $J > 0$ system is in ferromagnetic state, for $J < 0$ it is in anti- or ferri- magnetic state. In the semi-classical approximation we can replace $\mathbf{S}$ with a continuous function $\mathbf{M}$. This approximation holds when the characteristic length of magnetization spatial gradient is large compared to the distance between the atomic sites. Furthermore, $\mathbf{M}$ can be written as $S\mathbf{m}$, where $\mathbf{m}$ is a unit vector in direction of M. Using m, we can write the exchange energy as :

$$E_{ex} = -JS^2 \sum_i \sum_n (\mathbf{m}(\mathbf{r_i}).\mathbf{m}(\mathbf{r_i} + \mathbf{a_n})) \approx -JS^2 \sum_i \sum_n (\mathbf{m}(\mathbf{r_i}).\mathbf{m}(\mathbf{r_i}) + \mathbf{m}_i.(\mathbf{a}_n.\nabla)\mathbf{m}_i) \tag{2.2}$$

In the last step we have used first order Taylor expansion for $\mathbf{m}(\mathbf{r_i} + \mathbf{a_n})$). i is for the atomic site, and n is for the nearest neighbors. $\mathbf{a}_n$ is the distance from an atomic site to its neighbor. For cubic lattice with a lattice constant of c and taking into account $\mathbf{m}^2 = 1$, the continuous form of the exchange energy becomes:

$$E_{ex} = JS^2c^2 \sum_i \left((\frac{\partial \mathbf{m}}{\partial x})^2 + (\frac{\partial \mathbf{m}}{\partial z})^2 + (\frac{\partial \mathbf{m}}{\partial z})^2 \right) \tag{2.3}$$

For n atoms per site (1 for simple cubic, 2 for body centered, 4 for face centered) the density of atoms per unit cell is n/c^3. The exchange energy becomes for a volume V becomes:

$$\frac{nJc^2S^2}{c^3}\int\left((\frac{\partial\mathbf{m}}{\partial x})^2+(\frac{\partial\mathbf{m}}{\partial z})^2+(\frac{\partial\mathbf{m}}{\partial z})^2\right)dV = A_{ex}\int\left((\frac{\partial\mathbf{m}}{\partial x})^2+(\frac{\partial\mathbf{m}}{\partial z})^2+(\frac{\partial\mathbf{m}}{\partial z})^2\right)dV \tag{2.4}$$

Where A_{ex} is called the exchange stiffness.

Anisotropy Energy

The anisotropy energy makes the magnets polarization prefer a specific direction or a plane. The origin of the anisotropy can be both from bulk and the interfacial properties of the material or the heterostructure. In the case of materials with a principal axis pointing out of the plane (z direction), demonstrate a uniaxial anisotropy. This is usually caused from a layered structure or interfacial interactions (or, in general, breaking symmetry in z direction). The uniaxial anisotropy can be written as:

$$E_{anis} = -\sum_i K_i\mathbf{S}.\mathbf{z}^2 = -\int K_u M_s^2 m_z^2 dV \tag{2.5}$$

K_i and K_u are uniaxial anisotropy coefficients in atomic and continuous representations. For the planar anisotropy, the only difference is that K_u is smaller than zero, which makes the axis unfavorable and the plane perpendicular to it be the favorable direction.

Zeeman Energy

The Zeeman energy originates from the magnetization coupling to the external magnetic field $\mathbf{H}$. It can be written as:

$$E_{Zeeman} = -\int \mu_0 M_s\mathbf{H}.\mathbf{m}\ dV \tag{2.6}$$

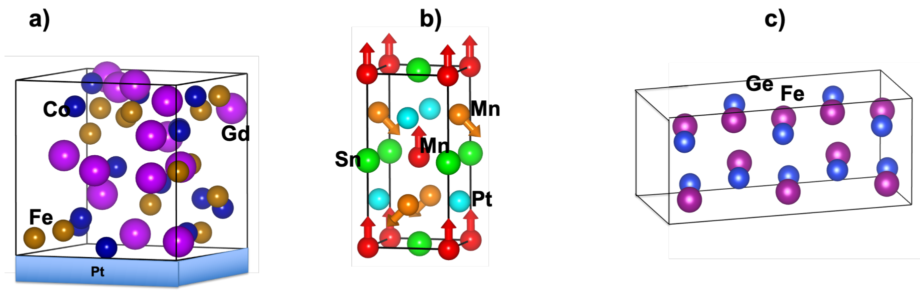

Figure 2.1: Structures with broken spatial inversion symmetry: (a) An amorphous ferrimagnets (CoFeGd) on top of a heavy metal (Pt) with interfacial DMI supporting Néel skyrmions; (b) D_{2d} tetragonal unit cells like Mn_2PtSn supporting antiskyrmions; (c) B20 FeGe supporting Bloch skyrmions.

Dzyaloshinskii-Moriya Interaction Energy

The Dzyaloshinskii-Moriya (DMI) energy, is the energy coming from the anisotropic exchange energy term. This energy term comes from symmetric breaking in the lattice. The symmetry breaking (Fig. 2.1) can come from bulk inversion asymmetry, such as in B20 solids like MnSe and FeGe, giving rise to Bloch skyrmions whose spins progressively flip spatially from up outside to down inside the skyrmion moving in a plane perpendicular to the radial axis. An alternate way to break the inversion asymmetry is with a heavy metal underlayer, where the interfacial spin-orbit coupling creates the DMI resulting in Néel skyrmions, whose spins flip in the plane containing the radial axis. We can also get antiskyrmions in solids with D_{2d} symmetry, such as tetragonal Heuslers. The DMI energy can be written in the atomistic representation as:

$$E_{DMI} = \sum_{<i,j>} \mathbf{D_{i,j}}.(\mathbf{S_i} \times \mathbf{S_j}) \tag{2.7}$$

Where depending on the source of DMI energy, $D_{i,j}$ has different forms:

$$\boldsymbol{D} = \begin{cases} \hat{z} \times \boldsymbol{r}_{ij} \quad \text{Interfacial} \\ \boldsymbol{r}_{ij} \quad \text{B20} \\ \sigma_z.\boldsymbol{r}_{ij} \quad D_{2d} \end{cases} \tag{2.8}$$

r_{ij} is the displacement vector connecting the two i,j sites. Writing it in the continuous form, the DMI energy density can be written as:

$$\epsilon_{\mathrm{DMI}} = \begin{cases} D\boldsymbol{m} \cdot [(\boldsymbol{z} \times \boldsymbol{\nabla}) \times \boldsymbol{m}], \quad \text{Interfacial DMI} \\ D\boldsymbol{m} \cdot (\boldsymbol{\nabla} \times \boldsymbol{m}), \text{ B20 DMI} \\ D\left[\dfrac{\partial m_z}{\partial y} m_x + \dfrac{\partial m_z}{\partial x} m_y \right. \\ \qquad \left. - m_z \left(\dfrac{\partial m_y}{\partial x} + \dfrac{\partial m_x}{\partial y}\right)\right], \ D_{2d} \text{ DMI} \end{cases} \tag{2.9}$$

With the DMI energy being written as: $E_{DMI} = \int \epsilon_{DMI} \, dV$.

Demagnetization Energy

The origin of demagnetization energy is the long range dipolar interaction between two sites in the crystal lattice. In simple terms, this energy is the Zeeman energy from spins of each site interacting with the magnetic field generated by the rest of the spins of the magnetic material. This can be written as:

$$E_{demag} = -\frac{1}{2}\mu_0 M_s \int \mathbf{H_s}.\mathbf{m} \tag{2.10}$$

Where $H_s = M_s\mathbf{h}$ is magnetic field generated by the spins.

Skyrmion Configuration

Putting all the energy terms, the total energy E then becomes:

$$E = E_{ex} + E_{DMI} + E_{Zeeman} + E_{anis} + E_{demag} \tag{2.11}$$

The competition between these energy terms determines what state our magnet would be in. One of the possible states is the magnetic domain wall. Before going into the skyrmion state, it is helpful to look at the domain wall energetics. A domain wall is when we have two regions of opposing polarization in the magnet next to each other. The magnetization vector can be written as $\mathbf{m} = (\sin\theta\cos\psi, \sin\theta\sin\psi, \cos\theta)$ where both of θ and Ψ are position dependent. The energy of a one dimensional domain wall can be written as (ignoring DMI and demagnetization energy terms):

$$E_{DW} = \int \left(A_{ex}(\frac{\partial\theta}{\partial x})^2 + K_u \cos^2(\theta) \right) dV \tag{2.12}$$

Solving this equation with boundary conditions $d\theta/dx|_{x=\infty} = 0$ gives us the equation for a 1-D domain wall as $\theta(x) = 2\tan^{-1}\left[e^{(x-x_0)/\Delta_0}\right]$ where x_0 is the center of the domain wall and $\Delta = \sqrt{A/K}$ is generally known as the domain wall width. As for the Ψ it is taken to be constant ψ_0, $\psi_0 = 0$ is a Bloch domain wall, and $\psi_0 = \pi/2$ is a Néel domain wall.

A skyrmion can be seen as two opposing domain walls at antipodal locations. If we move from x coordinate to radial coordinate r we have an ansatz for skyrmion profile :

$$\begin{aligned}\theta_{2\pi} &= 2\arctan\left[e^{\frac{-r+r_0}{\Delta}}\right] + 2\arctan\left[e^{\frac{-r-r_0}{\Delta}}\right] = 2\arctan\left(\frac{\cosh\frac{r_0}{\Delta}}{\sinh\frac{r}{\Delta}}\right)\\ &\rightarrow 2\arctan\left(\frac{\sinh\frac{R_{sk}}{\Delta}}{\sinh\frac{r}{\Delta}}\right)\end{aligned} \tag{2.13}$$

In the last step, we changed the form a little bit ($\cosh\frac{r_0}{\Delta} - \rightarrow \sinh\frac{R}{\Delta}$) so that the parameter R_{sk} directly correspond the skyrmion radius of our definition - $\theta(r = R_{sk}) = \pi/2$. Since the models above are derived from 1D Hamiltonian, the solution $\Delta = \sqrt{A/K}$ does not apply to the skyrmions. Therefore we treat the 2π model as a shape function with parameters R_{sk} and Δ to be determined by minimizing the total energy of skyrmion Hamiltonian. Furthermore, the 2π model only describes the radial part of skyrmion. We need another parameter Ψ to describe the in-plane tilt angle of the skyrmion (Fig. 2.2). If we assume there is a vortex-like rotation, then the azimuthal angle θ must not vary around the circumference for a skyrmion and depend on radial coordinate alone, $\theta = \theta(r)$, while the tilt angle Ψ should increase linearly around the circle until it covers an integer multiple of 2π, so that $\Psi = N_{sk}\phi + \psi$, with vorticity N_{sk} an integer and ψ the domain angle or helicity. The topological index for a skyrmion is given by its winding number set by the orientation of the magnetization unit vector $\mathbf{m}$ in the 2-D (x, y) plane

$$N_{sk} = \frac{1}{4\pi}\int dxdy\ \mathbf{m}\cdot\left(\partial\mathbf{m}/\partial x \times \partial\mathbf{m}/\partial y\right) \tag{2.14}$$

The integral N_{sk} (Eq. 2.14) then simplifies to $[m_z(r = \infty) - m_z(r = 0)] \times [\Psi(\phi = 2\pi) - \Psi(\phi = 0)] = pN_{sk}$, where $m_z(r) = \cos\theta(r)$ and $[m_z(r = \infty) - m_z(r = 0)]$ is the polarity $p = \pm 1$. For simplicity, we take the polarization $p = 1$ onward unless otherwise is mentioned. Substituting the $\theta(r)$ and $\Psi(\phi)$ in $\mathbf{m}$, we can evaluate all

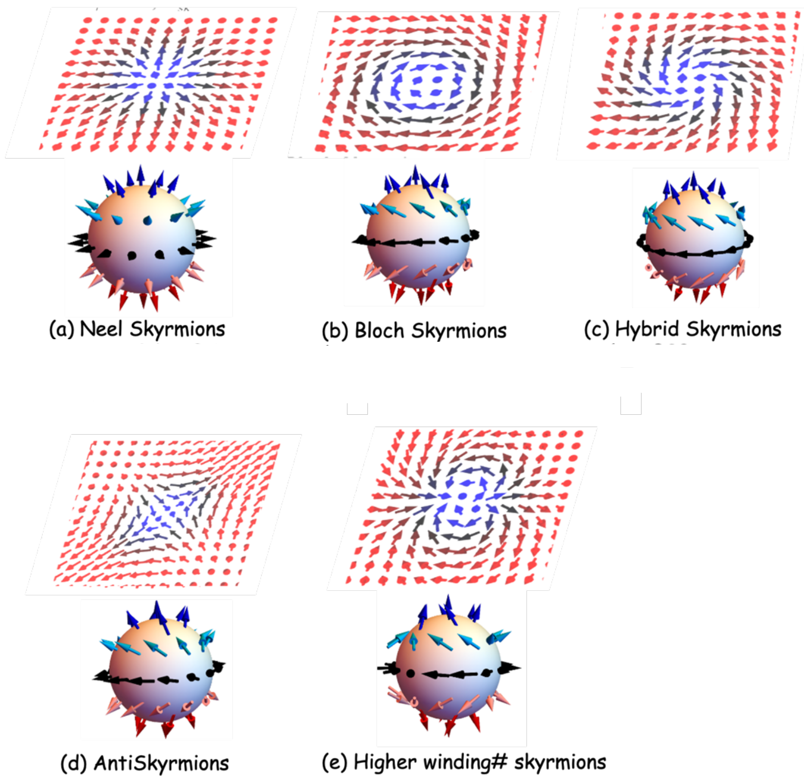

Figure 2.2: 3-D spherical arrangement of spins that generate 2-D skyrmions through stereographic projection. The north pole becomes the skyrmion core while the south pole maps to the background spin texture. The figure shows skyrmions of various winding numbers N_{sk} with same polarization $p = 1$ (Eq. 2.14) and domain angles/helicities ψ, along with typical materials supporting them. (a) Neel skyrmions (e.g. CoGd on Pt), $\psi = 0, N_{sk} = 1$ (b) Bloch skyrmions (B20 solids, e.g. FeGe), $\psi = \pi/2, N_{sk} = 1$ (c) Hybrid skyrmions (e.g. B20 on Pt), $\psi = \pi/4, N_{sk} = 1$ (d) AntiSkyrmions (D2d tetragonal inverse Heuslers e.g. MnPtSn), $\psi = \pi/2, N_{sk} = -1$ (e) Higher winding number skyrmions (Frustrated FM, merging of two skyrmions with opposite vorticities), $\psi = 0, N_{sk} = 2$. These excitations map onto the usual classification of 2-D linear excitations– stars for Néel skyrmions, cycles for Bloch skyrmions, spirals for hybrids and saddle points for antiskyrmions. In this picture, skyrmion spins wind anticlockwise as we move anticlockwise around a circle, while antiskyrmion spins wind in the opposite way. For higher m values skyrmions create cycloids along the circle while antiskyrmions trace out astroids. In general, a skyrmion of winding number N_{sk} has $N_{sk} - 1$ kinks (lines of 180^0 spin reversal) while an antiskyrmion of winding number $-N_{sk}$ has $|N_{sk}| + 1$ lines of singularity.

the energy integrals [15, 16, 17]:

$$\begin{aligned}
E_{\text{ex}} &= (2\pi A_{ex} t_F)\left(\frac{2R_{sk}}{\Delta} + \frac{2\Delta}{R_{sk}} N_{sk}^2\right) f_{\text{ex}}(\rho) \\
E_{\text{DMI}} &= -(2\pi R_{sk} t_F)\, \pi D f_{\text{DMI}}(\rho) \\
E_{\text{ani}} &= (4\pi K_u t_F)\, R_{sk} \Delta f_{\text{ani}}(\rho) \\
E_{\text{Zeeman}} &= \left(\pi R_{sk}^2 t_F\right) \times (2\mu_0 M_S H_z)\, f_{\text{Zeeman}}(\rho) \\
E_{\text{demag}} &= -\left(2\pi\mu_0 M_s^2 t_F\right) R_{sk}\Delta \times \\
&\quad (f_{\text{s}}(\rho, t_{FM}/\Delta) - \cos\psi^2 f_{\text{v}}(\rho, t_{FM}/\Delta)) \\
\text{with} \quad D &\equiv \left(D_{\text{int}}\cos\psi - D_{\text{bulk}}\sin\psi\right),
\end{aligned} \tag{2.15}$$

where ψ is once again the domain tilt angle. $f_{\text{s}}(\rho, t_{FM}/\Delta)$ and $f_{\text{s}}(\rho, t_{FM}/\Delta)$ are surface and volume demagnetization form factors respectively. For ultra thin film limit, $t_{FM} \ll \Delta, R_{skm}$, $f_{\text{s}} \simeq f_{\text{ani}}$ and f_{v} can be ignored[18]. The form factors for small size, obtained by fitting numerical simulations, are given by

$$\begin{aligned}
f_{\text{ex}}(\rho) &\approx \left[1 + 1.93\frac{\rho(\rho - 0.65)}{\rho^2 + 1} e^{-1.48(\rho - 0.65)}\right] \\
f_{\text{ani}}(\rho) &\approx \left[1 - \frac{1}{6\rho} e^{-\rho/\sqrt{2}}\right] \\
f_{\text{DMI}}(\rho) &\approx \left[N_{sk} + \frac{1}{2\pi\rho} e^{-\rho}\right] \\
f_{\text{Zeeman}}(\rho) &\approx \left[1 + \frac{\pi^2}{12\rho^2} - \frac{0.42}{\rho^2} e^{-\rho^2}\right]
\end{aligned} \tag{2.16}$$

Where the exponential terms are the correction for small skyrmions ($\rho \lesssim 1$). It would be useful to see how ψ and N_{sk} can be determined from the energetics. The

DMI energy terms using the θ and Φ of the skyrmion can be simplified to:

$$\epsilon_{\mathrm{DMI}} = \begin{cases} D_0 \cos\Big[(N_{sk}-1)\phi + \psi\Big]\Big(\partial_r\theta + \dfrac{N_{sk}}{r}\sin\theta\cos\theta\Big) \\ \qquad \text{(Interfacial DMI, Néel skyrmion)} \\ D_0 \sin\Big[(N_{sk}-1)\phi + \psi\Big]\Big(\partial_r\theta + \dfrac{N_{sk}}{r}\sin\theta\cos\theta\Big) \\ \qquad \text{(B20 bulk DMI, Bloch skyrmion)} \\ D_0 \sin\Big[(N_{sk}+1)\phi + \psi\Big]\Big(-\partial_r\theta\cos 2\theta \\ \qquad\qquad\qquad\qquad + \dfrac{N_{sk}}{r}\sin\theta\cos\theta\Big) \\ \qquad (D_{2d}\text{ DMI, antiskyrmion}) \end{cases} \tag{2.17}$$

with $D_0 = 2\pi t_F D$ and t_F the film thickness. The $N_{sk}\sin\theta\cos\theta/r$ term, has a much smaller contribution to the energy than the other terms. This would make $N_{sk} > 1$ unfavorable, as the term in exchange energy related to the winding number changes as N_{sk}^2. We can then see from the integrals in the Appendix that for interfacial and B20 DMI $N_{sk} = 1$ gives the minimum energy for $\psi = 0(\pi), \pi/2(3\pi/2)$ respectively (depending on DMI sign). For the antiskyrmion, $N_{sk} = -1$ and $\psi = \pi/2(3\pi/2)$.

Alternatively, we can look at the skyrmions from the symmetry analysis of the DMI vectors. For skyrmions stabilized by DMI set by crystal structure (Fig. 2.1), the symmetry breaking energy connecting two spins $\boldsymbol{S}_{i,j}$ takes the form shown in Eq. 2.8. The interfacial DMI vector is set by a symmetry breaking field perpendicular to the interface between a heavy nonmagnetic metal and a magnetic film, the B20 DMI vector is aligned within a non-centrosymmetric magnet between the spin carrying atoms, and the D_{2d} DMI vector set by the elongation of the magnetic unit cell along with the $\hat{y}$-direction. The vector field for the $\boldsymbol{D}$ can then be rewritten in 2-D as:

$$\boldsymbol{D} = \begin{cases} \pm \begin{pmatrix} -y \\ x \end{pmatrix} & \text{Interfacial, Néel skyrmions} \\ \pm \begin{pmatrix} x \\ y \end{pmatrix} & \text{B20, Bloch skyrmions} \\ \pm \begin{pmatrix} x \\ -y \end{pmatrix} & D_{2d}, \text{ antiskyrmion} \end{cases} \tag{2.18}$$

From the E_{DMI} in order to get lowest DMI energy, the vector field of each $\boldsymbol{S}$ must be in a plane perpendicular to $\boldsymbol{D}$ so that $\boldsymbol{S}_i \times \boldsymbol{S}_j$ is parallel/antiparallel to $\boldsymbol{D}_\perp$, the vector perpendicular to the DMI vector $\boldsymbol{D}$:

$$\frac{d}{dt}\begin{pmatrix} x \\ y \end{pmatrix} = \boldsymbol{D}_\perp = \begin{cases} \pm \begin{pmatrix} x \\ y \end{pmatrix} & \text{Néel} \\ \pm \begin{pmatrix} -y \\ x \end{pmatrix} & \text{Bloch} \\ \pm \begin{pmatrix} y \\ x \end{pmatrix} & \text{antiskyrmion} \end{cases} \tag{2.19}$$

This would give A in our linear systems classification as:

$$A = \begin{cases} \pm \begin{pmatrix} 1 & 0 \\ 0 & 1 \end{pmatrix} & \text{Néel} \\ \pm \begin{pmatrix} 0 & -1 \\ 1 & 0 \end{pmatrix} & \text{Bloch} \\ \pm \begin{pmatrix} 0 & 1 \\ 1 & 0 \end{pmatrix} & \text{antiskyrmion} \end{cases} \tag{2.20}$$

whose traces and determinants satisfy the 2-D Poincaré map classification rules above.

2.1.1 Phase-Space for static skyrmions

Several parameters set the skyrmion static and dynamic properties - specifically saturation magnetization M_s, anisotropy field H_k, damping α, external magnetic field H_{ext}, DMI D and exchange stiffness A_{ex}. The phase space can guide us in choosing materials that can host small skyrmions with long enough lifetimes. Additionally, a high Curie temperature, set primarily by exchange, is required to have the required material stability. Figure 2.3 shows the skyrmion phase space sandwiched between the background ferro/ferrimagnetic ground state and the stripe phase.

What determines Skyrmion Size?

A skyrmion has a circular core and a transition region (domain wall) to the background spin texture on the outside. By minimizing energy terms with respect to skyrmion radius and domain wall transition width, we get an equation for skyrmion size. The skyrmion energy barrier then can be calculated from the skyrmion radius and width, as shown in Fig. 2.4. For a constant interfacial DMI, there is an op-

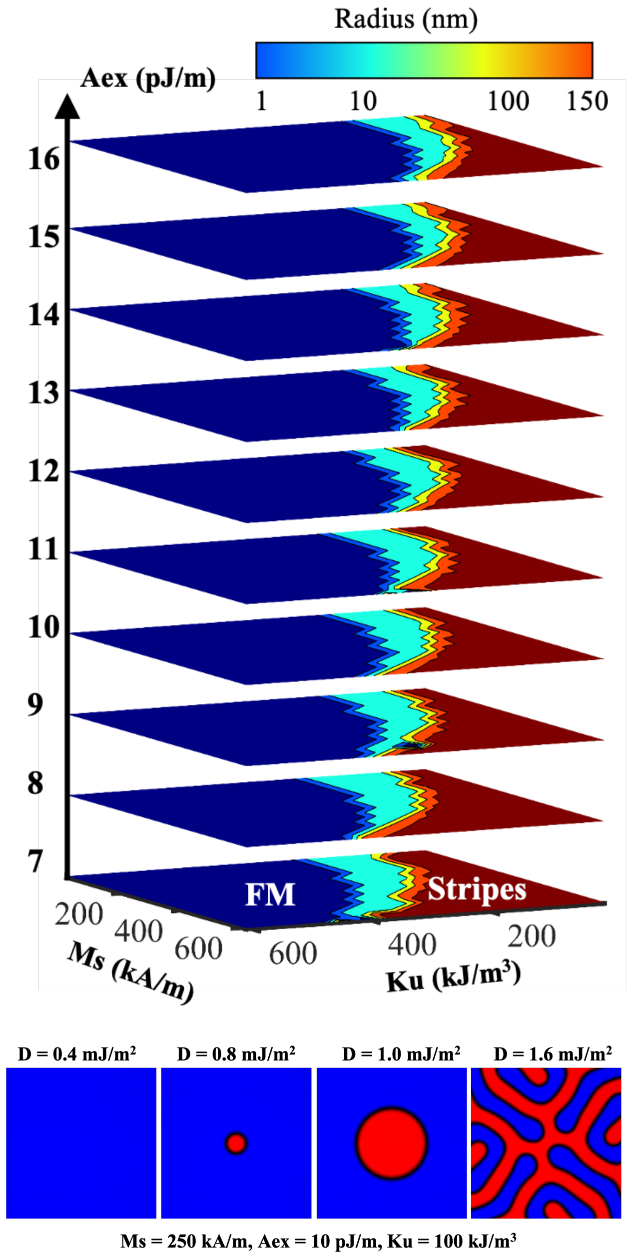

Figure 2.3: A sequence of zero-temperature phase space diagrams for various exchange stiffnesses with interfacial DMI, $D = 1$ mJ/m^2 and thickness $t_{FM} = 3\,nm$. As stiffness increases, the favorable region that can host isolated metastable ~ 10 nm skyrmions shrinks, and the borders separating them from competing phases (ferro/ferrimagnetic background, vs. stripe phase) move towards lower anisotropy. This is expected, as a smaller anisotropy compensates for larger exchange. The pictures below the phase diagram show the evolution of a skyrmion stabilized at zero temperature with parameters listed above, with subsequently increasing the DMI. Going from the ferromagnetic phase (left) to the stripe phase (right).

timized thickness that gives the maximum energy barrier. The points to note are that the energy barrier denoting skyrmion stability/lifetime is maximized for specific skyrmion radius and film thickness and that this barrier maximizing (and local energy minimizing) radius increases with DMI until a destabilization point where there is a phase transition to a skyrmion lattice. Lowering DMI for an isolated skyrmion lowers its size but also reduces thermal stability (Fig. 2.4) by making the metastable wells shallower and allowing the skyrmion to melt into the homogeneous magnetic background.

Minimizing the energy for an isolated skyrmion, we get the skyrmion size. The result for large skyrmions at zero magnetic field is [15, 16, 17, 18]

$$R_{sk} = \Delta\sqrt{\frac{A_{\mathrm{ex}}}{A_{\mathrm{ex}} - \Delta^2 K}} = \frac{\Delta}{\sqrt{1-(D/D_c)^2}}, \qquad \Delta = \frac{\pi D}{4K}, \tag{2.21}$$

where D is the DMI. The critical DMI is $D_c = 4\sqrt{A_{\mathrm{ex}}K}/\pi$. Here the effective anisotropy includes contributions from the demagnetization field $K \approx K_u - \mu_0 M_s^2/2$. Equation 2.21 shows that a perpendicular magnetic anisotropy is required to stabalize skyrmion in zero magnetic field.

Note that these equations change a bit with size. For ultra small skyrmions ($R_{sk} \lessapprox 10$ nm, $\rho = R_{sk}/\Delta \lessapprox 2$), additional form factors $f(\rho)$ (Eq. 2.16) must be taken into consideration, at the cost of more numerical complexity.

It is worth emphasizing that the two terms essential for stabilizing the skyrmion, both involving N_{sk}, are the $\sim -t_F D N_{sk}$ Dzyaloshinskii-Moriya term that gives a negative slope for the energy vs. radius curve, and the $\sim N_{sk}^2 \Delta/R_{sk}$ term in the exchange energy that provides a curvature to its energy curve. Together these two terms allow the creation of a metastable minimum (Fig. 2.4). The last term appears solely due to the circular nature of the skyrmion, i.e., added terms in the cylindrical

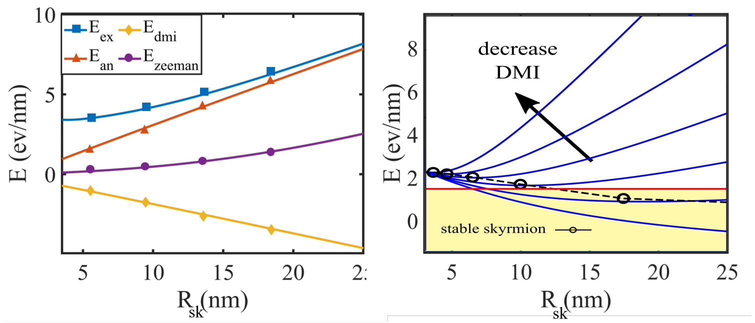

Figure 2.4: (Left) Schematic of energy terms for a skyrmion. The 2-D topological contribution to exchange $\propto N_{sk}^2\Delta/R$ and the negative DMI energy $\propto -N_{sk}\pi D$ together produce a local energy minimum for an isolated metastable skyrmion. (Right) Reducing DMI shifts the minimum to a lower radius, creating smaller isolated skyrmions while at the same reducing the energy well and thus their lifetime to dissolve into the background continuum. Increasing DMI increases skyrmion size, until at $D = D_c$ the skyrmion destabilizes into a stripe phase, indicated in yellow.

gradient arising from variations in cylindrical radial and angular unit vectors from point to point along the azimuthal direction.

2.1.2 Skyrmion Dynamics

To have a low latency skyrmion-based device, fast skyrmions at small energy costs are required. An efficient way to drive a skyrmion or a domain wall is using spin-orbit torque. As the picture shows (Fig. 2.5), a flowing charge current in a heavy metal underlayer creates a vertical separation of spins along the axis perpendicular to the metal-magnet interface. The injected spins create an effective magnetic field causing precession of the skyrmion spins around it, leading to a flow of the skyrmion whirring forward like a buzz saw. For a Néel skyrmion, there will also be a precessional phase lag in the transverse direction, leading to a net Magnus force that drives a Néel skyrmion at an angle with respect to the charge current. The actual expressions can be readily obtained from the Thiele approximation to the spin dynamics [19, 20, 21].

We start with the LLG micromagnetic equation for the normalized magnetic mo-

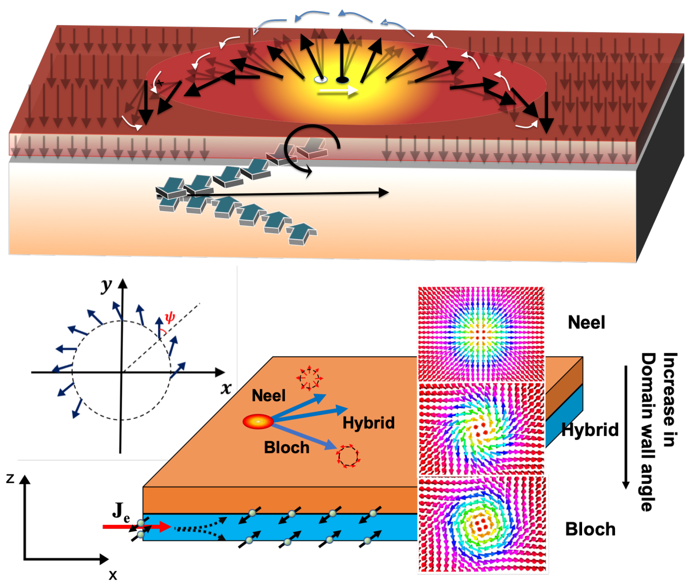

Figure 2.5: Current in a heavy metal underlayer separates spins through spin-orbit torque, and the injected spins lead to precessional torque on individual spins that drives a domain wall or a skyrmion forward. A finite tilt in domain angle ψ causes the topological excitation to see a transverse Magnus force as well depending on whether it is Néel ($\psi = 0, \pi$), Bloch ($\psi = \pm\pi/2$) or hybrid.

ment, in presence of an applied SOT applied to different units i (sublattices or layers) [9]

$$t_{F_i}\frac{M_{s_i}}{\gamma_i}\frac{d\boldsymbol{m}}{dt} = -M_{s_i}\boldsymbol{m}\times\boldsymbol{H}_{\text{eff}} + \alpha t_{F_i}\frac{M_{s_i}}{\gamma_i}\boldsymbol{m}\times\frac{d\boldsymbol{m}}{dt}$$
$$- a_j\,\boldsymbol{m}\times(\boldsymbol{m}\times\boldsymbol{P}) - \eta\, a_j\,(\boldsymbol{m}\times\boldsymbol{P}) \tag{2.22}$$

where $\boldsymbol{P}$ is the polarization of the injected spins from the heavy metal to the magnet, $a_j = (\hbar/2q)\theta_{\text{SH}}j_{\text{HM}}$ is the adiabatic spin-orbit torque coefficient that arises when conduction electrons follow the local texture of the spatially varying magnetization (i.e., the inertial term of a hydrodynamic equation), α is Gilbert damping, η is the non-adiabaticity parameter, and θ_{SH} is the spin Hall angle that relates transverse spin current density to longitudinal charge current density j_{HM}, related through the strength of the spin-orbit coupling in the heavy metal. $\mathbf{H_{eff}} = \frac{-1}{\mu_0}\frac{\delta E}{\delta \mathbf{m}}$ is the effective field.

Using the Thiele approximation, where we assume the magnetic object conserves its rigid shape through out its movement, we get the following equation for i$^{\text{th}}$ layer in a multi sublattice magnet [17]

$$\begin{aligned} &\boldsymbol{F}_{ex_i} + \Sigma_j F_{ij} + 4\pi N_i \; t_{F_i} \; M_{s_i}(\hat{z} \times \boldsymbol{v}_{sk})/\gamma_i \\ &-t_{F_i} \; M_{s_i}\mathcal{D}.(\alpha \boldsymbol{v}_{Sk})/\gamma_i - \frac{4\hbar}{2q} \; I \; \theta_{SH} R(\psi) j_{\text{HM}} = 0 \end{aligned} \tag{2.23}$$

We have taken $\boldsymbol{P} = \boldsymbol{j}_{\text{HM}} \times \hat{z}$ to generalize to any $\boldsymbol{j}_{hm}$ direction.

$\boldsymbol{F}_{ex_i} = -\mu_0 M_{s_i} \int \boldsymbol{H}_{\text{eff}}.\nabla \boldsymbol{m}$ denotes forces from edges, defects, skyrmion-skyrmion repulsion and varying fields (for example anisotropy gradient), and is zero when $\boldsymbol{H}_{\text{eff}}$ is uniform. F_{ij} on the other hand arises from interactions between neighboring layers or sublattices. The third term arises from the inertial term to the right of the LLG equation, with $N_i = \pm 1$ the skyrmion winding number. The fourth term arises from the Gilbert damping term in the LLG equation, and involves $\mathcal{D}$ the dissipation tensor—assumed isotropic with diagonals $\mathcal{D}_{xx}$ set by the dissipation tensor, $\mathcal{D}_{ij} = \int dxdy(\partial_i \boldsymbol{m} \cdot \partial_j \boldsymbol{m})$. For a 2π model this term matches the exchange integral to within a constant (Eq. 2.16), $\mathcal{D}_{xy} = \mathcal{D}_{yx} = 0$, $\mathcal{D}_{xx} \approx R_{sk}/2\Delta \times f_{ex} = \rho f_{ex}(\rho)/2$. γ_i is the gyromagnetic ratio, t_{F_i} is the thickness of sublattice i. f_{ex} is the fitting term coming from the exchange integral. M_{s_i} saturation magnetization of the ith film. The final term arises from the adiabatic spin orbit torque, where $I = \frac{1}{4} I_d(\rho, \Delta)$ is the integral of DMI energy Eq. 5.3, $I_d = \int_0^\infty dr[r\partial_r\theta + N_{sk}\sin\theta\cos\theta] = \pi R_{sk} f_{\text{DMI}}$. This integral is, in effect, a shape factor of the skymion. $R(\psi) = \begin{pmatrix} \cos\psi & \sin\psi \\ -\sin\psi & \cos\psi \end{pmatrix}$ is the rotation matrix acting on the 2-D unit vectors and involves the domain angle ψ

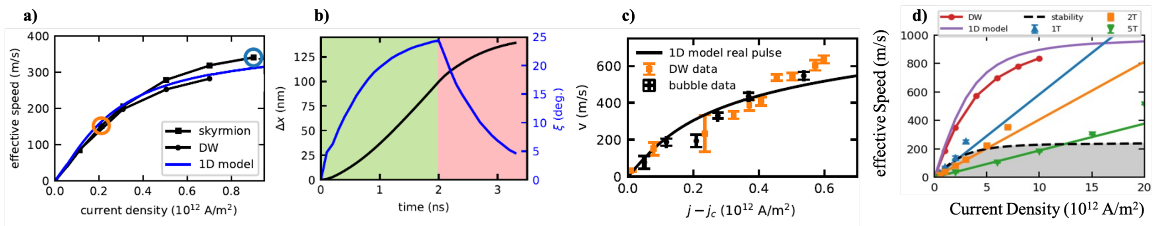

Figure 2.6: Non-linearity of drive and deformation as the origin of skyrmion speed reduction. (a) Simulated skyrmion and DW speeds as a function of applied current density. In contrast to Thiele model descriptions considering skyrmions as rigid particles (which expect skyrmion motion to follow a linear trend), the speeds of DWs and skyrmions are, in fact, practically identical and follow the 1-D DW model. (b) DW and skyrmion displacement (black line) increase even after the current is switched off due to inertial effects caused by the canting of spins in the wall (blue curve). This effect coupled with non-rectangular current pulses can prolong the displacement of skyrmions in an experiment. (c) Experimental observation of skyrmion and DW speeds and 1-D model taking into account the pulse shape. No significant difference is visible [1].

($\psi = 0, \pi$ for Néel skyrmions, $\pm\pi/2$ for Bloch, and in between for hybrid), the current density $\boldsymbol{j}_{\mathrm{HM}}$ in the HM layer assumed to be along the x direction (polarization in $-\hat{y}$ direction). The non-adiabatic SOT term vanishes upon volume integration.

Solving for $\boldsymbol{v}_{sk}$, we get

$$\boldsymbol{v}_{sk} = \frac{4\pi B\theta_{SH} R(\psi - \theta_0)}{\sqrt{\alpha^2 S(T)^2 \mathcal{D}_{xx}^2 + (4\pi S_N(T))^2}} \mathbf{j}_{hm}, \tag{2.24}$$

where $B = \pi\hbar I/2q$, $S(T) = \Sigma_i M_{s_i}(T) t_{F_i}/\gamma_i$ is the spin angular momentum summed over volume, $S_N(T) = \Sigma_i N_{sk_i} M_{s_i}(T) t_{F_i}/\gamma_i$ is the topological spin angular momentum and $\tan\theta_0 = 4\pi\langle N_{sk}\rangle/\alpha\mathcal{D}_{xx}$.

The velocity equation has a simple interpretation—we can write it as

$$q n_e v_{sk} = R(\psi - \theta_0) j_{hm}, \tag{2.25}$$

where the electron density n_e is again set by angular momentum conservation of the form:

$$n_e \frac{\hbar}{2}\theta_{SH} = \frac{M_s}{\gamma} t_F \sqrt{(4\pi N_{sk})^2 + \alpha^2 \mathcal{D}_{xx}^2},$$
$$= \frac{M_s t_F \alpha \mathcal{D}_{xx}}{\gamma} \sec\theta_0. \tag{2.26}$$

The new rotation matrix $R(\psi - \theta_0)$ tells us that there is a deviation Θ_{SkH} from the current path due to the Magnus force or the skyrmion Hall effect:

$$\frac{v_{sk,y}}{v_{sk,x}} \equiv \tan\Theta_{SkH} = \left(\frac{4\pi\langle N_{sk}\rangle \ \cos\psi - \alpha \ \mathcal{D}_{xx} \ \sin\psi}{4\pi\langle N_{sk}\rangle \ \sin\psi + \alpha \ \mathcal{D}_{xx} \ \cos\psi} \right), \tag{2.27}$$

With the average topological index $\langle N_{sk}\rangle = S_N/S$. We see that even in the absence of dissipation, there is a topological damping term proportional to N_{sk} that limits the skyrmion speed compared to a domain wall. which depends on the magnitude of the topological term N_{sk} relative to the effective damping $\alpha\mathcal{D}_{xx}$ (Gilbert damping times shape factor)—one term tries to move the skyrmion perpendicular to the current, while the other tries to bring it back to the current. The rotation matrix depends on the domain wall angle ψ, trying to move along the current for Néel skyrmions ($\psi = 0, \pi$) and perpendicular for Bloch skyrmions ($\psi = \pm\pi/2$).

Let us now compare these skyrmion velocities with the simpler 1-D DW equations within the Thiele approximation:

$$v_{\mathrm{DW}} = \frac{\pi}{2} \frac{D_{int} j_{\mathrm{hm}}}{\sqrt{(S_0(T) j_{hm})^2 + (\alpha S(T) j_0)^2}}. \tag{2.28}$$

With $S_0(T) = |S_1(T) - S_2(T)|$, $S = |S_1(T) + S_2(T)|$ and $j_0 = 2q t_F D_{int}/\hbar\theta_{SH}\Delta_0$. For speeds close to the magnon speeds, relativistic effects have to be taken into account. In Appendix. B, we explain the relativistic dynamics of the skyrmions and DWs and the relativistic corrections to Eqs. 2.24,2.28 in detail.

Note that Eq. 2.28 suggests that ferromagnetic domain wall speeds saturate to a constant $\propto D_{int}/M_{\text{eff}}$ for large current densities j_{hm} that sit in both the numerator and the denominator of the velocity term $\boldsymbol{v}_{\text{DW}}$, leading to an overall damped motion (Fig. 2.6). This may imply that skyrmions could quickly overcome the speeds of a corresponding straight, 1-dimensional domain wall in the same material. However, it is important to realize that skyrmion speeds are furthermore dependent on internal spin dynamics, which start to dominate at high currents and are not captured by the Thiele equations. A simple example of this is the change in size and shape of a skyrmion, which occurs under the influence of a current [22, 23]. Especially at higher current drives, these effects can dominate the skyrmion dynamics, leading to an elongation of the skyrmion and the formation of a domain wall-like section within the otherwise round skyrmion. These, in turn, cause them to be driven by the same dynamics as domain walls. Together with other effects such as added topological damping, it becomes apparent that a skyrmion cannot move faster than a domain wall under identical conditions.

It is also important to point out that by applying a proper 1-D domain wall model that accounts for the drive's pulse shape and inertial effects caused by domain wall spin canting (see Fig. 2.6), skyrmions near the relativistic speed limit (Appendix Subsection D) move with the same speeds as domain walls. This has been observed both in micromagnetic simulations as well as current-driven experiments on ferrimagnetic CoGd (Fig. 2.6). The relativistic speed limit increases strongly for antiferromagnets ($M_{\text{eff}} = 0$) with zero topological damping, while the limitation set by skyrmion distortion will still remain in place and prevent skyrmions from moving faster than domain walls.

Even nanoscale skyrmions like those reported by Romming *et al.* [24], with arguably the highest rigidity of all skyrmions (due to small size) are not impervious to the effect, as Fig. 2.6(d) shows: The mobility of the skyrmions (blue, orange and green data) initially follows the linear mobility curve for undistorted skyrmions that can be derived from the Thiele equation [17]. However, after a critical current density is reached, the skyrmion cannot withstand the enormous torques any longer and collapses long before reaching the 1-D domain wall limit (purple, red) in the material. The gray shaded area gives a phenomenologically determined stability regime for skyrmions, outside of which the skyrmion starts to loose its rigidity. Note that the slope of the Thiele mobility increases with decreasing magnetic field up to about 1 T, where it becomes too low to stabilize skyrmions in the material.

2.2 Summary

In this chapter, we looked at the energy contributions in a magnetic film and how the competition between these energy terms lead to the creation of skyrmions. Understanding the energy terms allowed us to derive analytical equations for skyrmion size. We provided two separate proofs of skyrmion winding number and helicity based on energy and symmetry arguments. By minimizing the energy landscape of a ferromagnet the phase space for small skyrmions was calculated. After the energetics part, we looked at the skyrmion dynamics. To understand the dynamics of skyrmions and the topological hall effect, we first introduced the effective fields which come out of the energy landscape of the magnet. Using the effective fields, we saw how the LLG equation can describe the magnetodynamics. Finally, by assuming that the overall shape of a moving skyrmion is conserved, we introduced the Thiele equation. From the analytical equation for skyrmion velocity under applied spin current, we saw that an antiferromagnet would provide a much faster movement than an equal ferromagnet.

Chapter 3

Self Focusing skyrmions

As we saw in the previous chapter, the skyrmions can be nucleated and driven by spin orbit torque from a current driven in a heavy metal underlayer. Along its gyrotropic path, a Magnus force can cause a skyrmion to be annihilated at the boundaries. By combining interfacial and bulk Dzyaloshinskii-Moriya interactions (DMI), for instance, by using a B20 material on top of a heavy metal (HM) layer with high spin-orbit coupling, it is possible to engineer a hybrid skyrmion that will travel parallel to the racetrack with zero Magnus force. We show that by using a spatially varying interfacial DMI, a hybrid skyrmion will automatically self-focus onto such a track as its domain angle evolves along the path. Furthermore, using a gate driven voltage controlled magnetic anisotropy (VCMA), we can control the trajectory of the hybrid skyrmion and its eventual convergence path and lane selection in a racetrack geometry. This chapter is reproduced from Ref. [25] co-authored with Yunkun Xie and Avik W. Ghosh.

3.1 Skyrmion Chirality

As we saw previously, the DMI energy comes from breaking bulk or interfacial inversion symmetry. The former, bulk DMI (bDMI), exists in chiral magnets such as B20 materials (MnSi, FeGe) and results in Bloch skyrmions with a ninety degree domain angle ψ (Fig. 3.1 inset), while the latter interfacial DMI (iDMI) prefers Néel skyrmions with zero domain angle. These two types of skyrmions are topologically equivalent, but their dynamical behavior are different [26, 27]. In particular, they tend to move orthogonal to each other due to a topologically generated Magnus force under the action of a spin orbit torque (SOT) [28, 29]. Eliminating that Magnus force [30, 31, 32] typically requires ferrimagnets at their angular momentum compensation point, or tracks with raised edges - operating thus at specific temperatures or along pre-set tracks. In a structure with both types of symmetry breaking however, we get hybrid skyrmions with a velocity aligned between Néel and Bloch [33, 34] (Fig. 3.1). For a specific domain angle the net Magnus and driving force from SOT will be in the direction of the applied current and allow the skyrmion to move linearly along the current path - but that requires a precise confluence of parameters setting the ratio of bulk and inversion asymmetry contributions.

A number of methods have been suggested in the skyrmion literature to drive them into rectilinear motion and mitigate skyrmion Hall drift. These include anisotropy engineering with raised edges and/or anisotropy gradients [30] and frustrated ferromagnets with fine tuned anisotropy engineering [35], magnetization compensation using ferrimagnets and synthetic antiferromagnets [32, 31], and iDMI engineering using material stacks with different iDMI signs [36] and hybrid skyrmions with uniform iDMI [34]. Notably all these structures are spatially uniform along the transport direction. They need precise fabrication to achieve compensation within a single racetrack right from the injection point. All except reference [35] allow no selectivity of multiple racetracks and none allow self-selection into a desired track through dynamic compensation. Such a self-selection can be quite critical to the initialization process in a logic operation [37, 38], where pre-existing skyrmions from a common repository

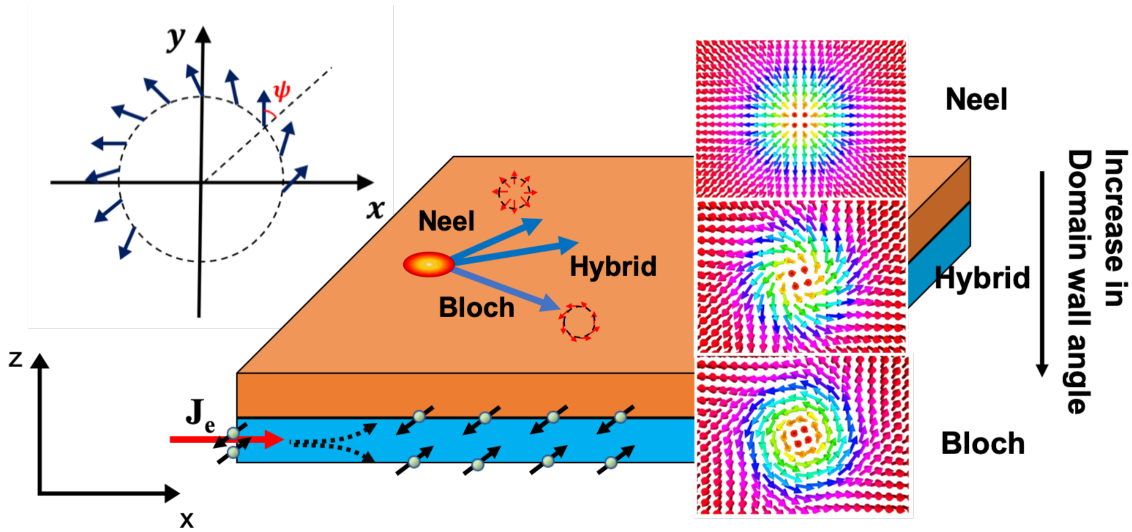

Figure 3.1: Schematic view of a skyrmion in a ferro/ferrimagnetic material (orange). In a FM/HM heterojunction, an applied current in a HM underlayer (black) generates a spin Hall effect that separates opposite spins, resulting in spin injection and torque applied in the FM layer. For a given current, Néel and Bloch skyrmions with orthogonal domain wall angle ψ will move perpendicular to each other, so that a suitably engineered hybrid can move along the current direction.

can be driven into respective racetracks without the high energy cost and reliability issues of on-site on-demand nucleation.

In this chapter, we show that hybrid skyrmions [39] can be made to naturally self-focus along a racetrack with spatially varying DMI (Fig. 3.2), for instance when it sits on a HM with varying thickness or composition (e.g. Pt_xW_{1-x}, Fig. 3.3). Using analytical results and numerical simulations describing skyrmion movement, we show that the domain angle for a traveling skyrmion will keep changing with varying DMI until it reaches the cancellation point for the Magnus force. Furthermore, we can dynamically control the converging lane of the skyrmion (Fig. 3.4) through a voltage controlled magnetic anisotropy (VCMA) at its interface with a top oxide layer. We can thus gate control the skyrmion trajectory to resonate into specific lanes, while allowing it to diffuse along between resonances.

Dynamics of hybrid skyrmions. One way to move a skyrmion is to use a FM/HM structure. A current in the HM layer, say Pt, separates spins through a spin Hall effect, resulting in the injection of a perpendicular spin current into the FM that then diffuses away from the FM/HM interface. The injected spins precess incoherently around the FM magnetization, applying in the process a spin orbit torque that flips the background spins and drives the skyrmions [40]. We start from the equation for velocity $\mathbf{v}$ that we obtained in the previous chapter:

$$\boldsymbol{v} = M^{-1}\Big(\boldsymbol{F} - 4\pi B\theta_{SH}R(\psi)\boldsymbol{j}_{hm}\Big), \quad M = \alpha\mathcal{D} + \mathcal{G} \tag{3.1}$$

where $\mathcal{G} = 4\pi\begin{pmatrix} 0 & N_{sk} \\ -N_{sk} & 0 \end{pmatrix}$ is the gyrotropic tensor. From this equation, we can extract the skyrmion hall angle $\phi_{skm} = \tan^{-1}(v_y/v_x)$, and the critical domain angle ψ_c where the Magnus force vanishes ($\phi_{skm} = 0$). At zero force $F = 0$, we get

$$\phi_{skm} = tan^{-1}\left(\frac{G\ \cos\psi - \alpha\,\mathcal{D}_{xx}\ \sin\psi}{G\ \sin\psi + \alpha\,\mathcal{D}_{xx}\ \cos\psi}\right) \tag{3.2}$$

$$\psi_c = tan^{-1}\Big(G/\alpha\mathcal{D}_{xx}\Big) \quad \text{when } \phi_{\text{skm}} = 0 \tag{3.3}$$

with $G = 4\pi N_{sk}$. The domain angle ψ, set by the ratio of bulk to interfacial DMI, determines if a skyrmion is Néel (Figs. 2, 3) ($\psi = 0, \pi$), Bloch ($\psi = \frac{\pi}{2}, \frac{3\pi}{2}$) or hybrid ($\psi \neq 0, \frac{\pi}{2}, \pi, \frac{3\pi}{2}$). For a given R_{skm} and Δ, the velocities of Bloch and Néel skyrmions are perpendicular to each other ($\boldsymbol{v}_{Bloch}.\boldsymbol{v}_{N\acute{e}el} = 0$), so that a proper hybrid skyrmion at domain angle ψ_c moves along the current direction. However, reaching this domain wall angle requires a precise tuning of parameters.

Spatially varying iDMI for self-focusing skyrmions. Let us now consider a hybrid skyrmion moving in a FM layer with both bulk DMI (e.g. a B20 material like FeGe

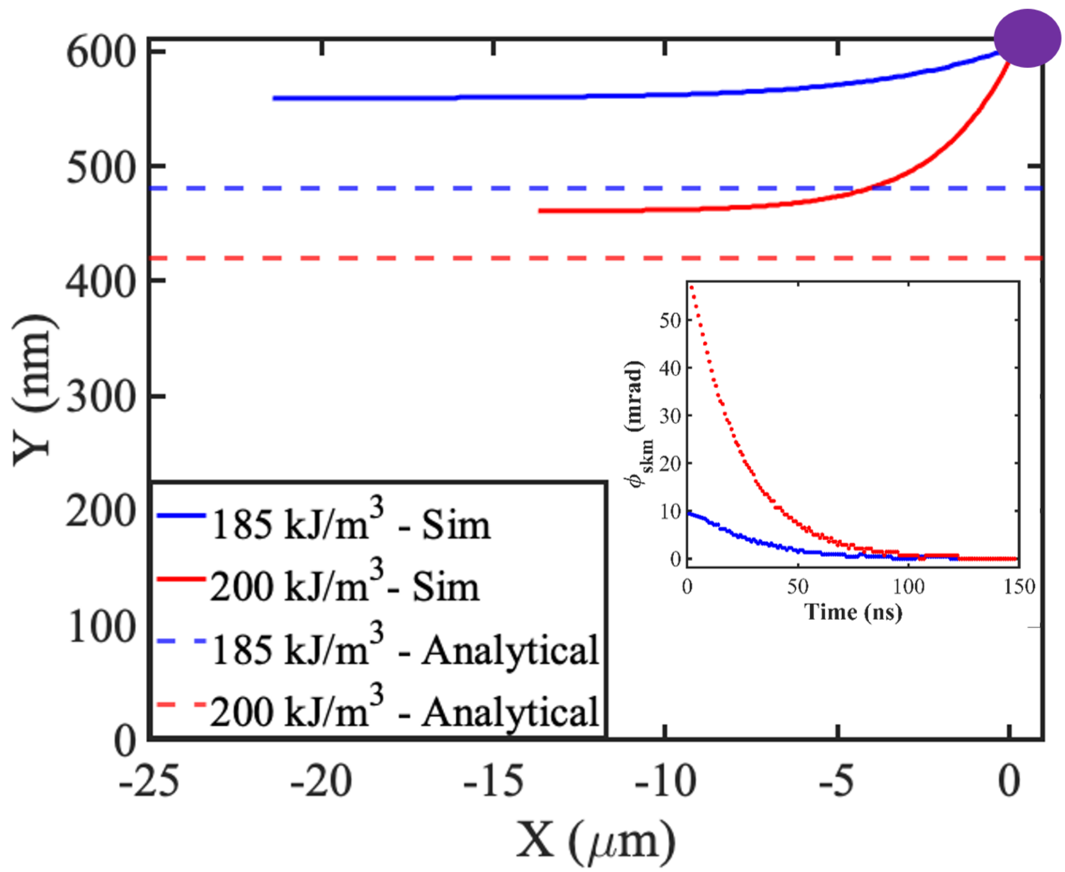

Figure 3.2: Converging lanes for different anisotropy values, simulated (solid) and quasi-analytical (dashed). Increasing anisotropy decreases size ρ, causing the domain angle ψ_c to increase according to Eq. 3.8, due to increasing $bDMI/iDMI$. Here iDMI decreases linearly from top (y = 800 nm, $D_{int} = 0.5mJ/m^2$) to bottom (y = 0 nm, $D_{int} = 0$). Dashed lines are quasi-analytical predictions of self-converging lanes. Inset shows ϕ_{skm} vs time. The purple circle shows the starting point of the skyrmions.

or MnSi) and a linearly varying interfacial DMI from HM spin-orbit coupling [41]

$$D_{int} = D_0 + \lambda y \tag{3.4}$$

The DMI energy density $\epsilon_{DMI} = D_{int} \cos\psi - D_{bulk} \sin\psi$. Solving $\partial\epsilon_{DMI}/\partial\psi = 0$, we can then get the evolution of ψ as a function of y from Eq 3.4

$$\psi(y) = \tan^{-1}\Big(\frac{-D_{bulk}}{D_0 + \lambda y}\Big) \tag{3.5}$$

meaning the skyrmions pick up increasingly more Néel characteristic during transit. The corresponding force from the linearly varying interfacial DMI [36]:

$$\boldsymbol{F}_{DMI} = -\frac{\partial E_{DMI}}{\partial \boldsymbol{r}} = 2\pi\lambda\frac{\gamma}{M_s}\Delta I_d\ \cos\psi\ \hat{y} \tag{3.6}$$

Where $E_{DMI} = \int 2\pi\epsilon_{DMI}(r\partial_r\theta + \cos\theta\sin\theta)\ dxdy$. Using a 2π domain wall model for the azimuthal angle $\theta(r)$, $\theta(r) = 2\tan^{-1}[\sinh\rho/\sinh(r/\Delta)]$, the DMI integral I_d can be approximated as $I_d \approx \pi\rho\Delta$. Putting in $\boldsymbol{F}_{DMI}$ in the Thiele equation, we get a correction to the critical angle: $\tan\psi_c = (1 + C)G/\alpha\mathcal{D}_{xx}$, with $C = 4\lambda e t_{FM}\alpha\mathcal{D}_{xx}/\pi\hbar N_{sk}G\theta_{SH}j_{hm}$. As Fig. 3.2 shows, the convergent lane depends on the anisotropy parameter K_u, which in turn affects the skyrmion size ρ and thereby the dissipation tensor $\mathcal{D}_{xx}$ responsible for the critical domain angle ψ_c. The dissipation integral $\mathcal{D}_{xx}$ is defined as [42]:

$$\begin{aligned}\mathcal{D}_{xx}(\rho) &= \int dxdy\ (\partial_x\boldsymbol{m})^2 \\ &= 2\pi\sinh^2\rho\int_0^\infty\frac{[\cosh 2r + 1]r + [\cosh 2r - 1]/r}{\Big(\sinh^2 r + \sinh^2\rho\Big)^2}dr\end{aligned} \tag{3.7}$$

in a 2π domain wall model. The integral above does not have an analytical solution to our knowledge. However, a simple fit that works quite well for $\rho \sim 0.5 - 4$ is $\mathcal{D}_{xx} \approx 5.96\sqrt{4.285 + \rho^2}$, so that:

$$\psi_c \approx tan^{-1}\Big(\frac{G}{5.96\ \alpha\sqrt{4.285 + \rho^2}}(1 + C)\Big) \tag{3.8}$$

The anisotropy dependence of the skyrmion size ρ can be seen from an evaluation of the energy integrals within a 2π model [43, 44], and can be approximated as (with zero external magnetic field)

$$\rho(y) = \left(\frac{D(y)}{D_c}\right)^2 \frac{C_1}{\sqrt{1 - C_2(D(y)/D_c)^4}} \tag{3.9}$$

where $D_c = 4\sqrt{A_{ex}K_u}/\pi$, $C_1 \approx 12.7$, $C_2 \approx 1.06$ and $D(y) = D_{int}(y)\cos\psi - D_{bulk}\sin\psi$ is the total DMI. Since D_{int} is changing with y (Eq. 3.4), ρ is a function of y for a given anisotropy. Solving $\psi_c = \tan^{-1}\left(\frac{-D_{bulk}}{D_0+\lambda y}\right)$ for y, we get the convergence lane (Fig 3.2).

We perform micromagnetic (MuMax3 [45]) simulations to verify our assumptions and see skyrmion behavior in a linearly varying iDMI with different anisotropies (Fig. 3.2). The parameters used in simulation are taken from [34, 33, 46, 47] for FeGe, $M_s = 300$ kA/m, A_{ex} = 7.5e-12 J/m, $D_{bulk} = 1\ mJ/m^2$, $\alpha = 0.2$, K_u = 185, 200 kJ/m^3 (assuming interfacial effects for ultra thin FeGe), $\theta_{SH} = 0.15$ and $j_{hm} = 10^{12} A/m^2$. The FM layer thickness t_{FM} is taken to be 2 nm. We apply a spin current of polarization $+\hat{y}$ in the $\hat{z}$ direction, arising for instance from SOT in the HM layer from a charge current in the $\hat{x}$ direction. The Magnus force will cause the skyrmion to have a velocity component in the $-\hat{y}$ direction. As the skyrmion comes down the FM, the interfacial DMI decreases, which leads to an increasing domain wall angle

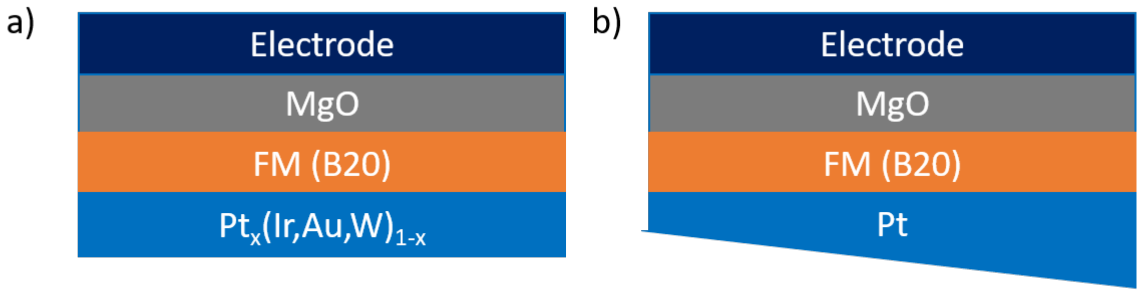

Figure 3.3: Possible stacking options a) Using $Pt_x(Ir, Au, W)_{1-x}$ by varying x value from left to right we can achieve a spatially varying interfacial DMI. b) By changing Pt thickness, or equivalently a varying thickness MgO underlayer between Pt and FM. The DMI from Pt increases for thicknesses of 1-3 nm and saturates thereafter, and can be used to get a spatially varying interfacial DMI. The top MgO-electrode stack sits on a select part of the racetrack for applying a Voltage Controlled Magnetic Anisotropy (VCMA, Fig. 3.4).

ψ (Eq. 3.5), until it reaches the critical angle ψ_c where it no longer has a velocity component along $\hat{y}$ and will have a rectilinear motion, self-focusing into a lane in the process.

Fig. 3.2a shows the tracks for a skyrmion injected at the low iDMI end, as obtained from a numerical simulation of the Landau-Lifschitz-Gilbert equation (which goes beyond the rigid skyrmion Thiele approximation), for various bulk anisotropy values K_u. The horizontal dashed lines show the convergent path coordinates y obtained from analytical approximations [48]. The decrease in skyrmion size ρ along the travel path y means that smaller skyrmions (e.g. with higher anisotropy) travel further down before self-focusing.

To get a linearly varying iDMI we suggest two possible approaches (Fig 3.3) - one is to use a varying thickness of HM layer, or more realistically of an MgO film between the HM layer and FM layer, to tune the iDMI. According to the experiments done in [49, 50], by putting a MgO layer between HM and FM, the iDMI can be increased substantially and this effect increases with thickness of MgO until it saturates for a

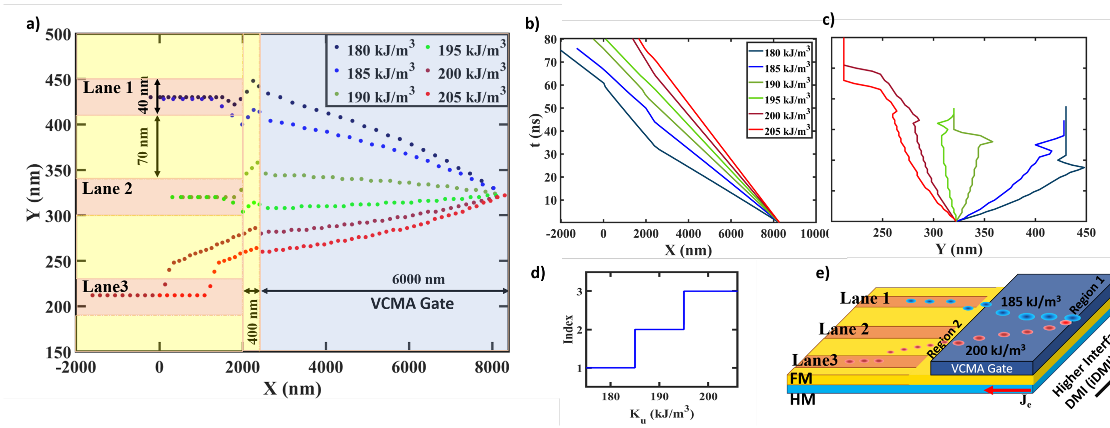

Figure 3.4: a) Skyrmion self-focusing with iDMI gradient of 312.5 J/m^3, varying from 0.45 mJ/m^2 at top, y=800 nm to 0.2 mJ/m^3 at bottom, $y = 0$. The anisotropy values in the legend are for the VCMA gated region (black). This should be achievable using an FM Pt_xW_{1-x} underlayer with x varying linearly from top to bottom. Lanes (Orange rectangles) are 40 nm wide each and 70 nm apart, with anisotropy of 190 kJ/m^3. The yellow part is set to have anisotropy of 220 kJ/m^3 so that it will provide the necessary repulsion for skyrmions to stay in lane. Converging lane for a skyrmion with $K_u = 220$ anisotropy is $y = \ 150nm$ (not shown) b),c) x and y vs time. d) The lane index for the final skyrmion convergence vs anisotropy in the VCMA gated region. e) Schematic view of the simulation geometry, black circles are for skyrmions for $K_u = 185kJ/m^3$ and red circles for $K_u = 200kJ/m^3$. Circle sizes correspond to actual skyrmion size.

thickness of around 2 nm. As the MgO layer has significantly higher resistance than the HM layer, most of current will travel trough the HM layer. However, further investigation is needed to understand how the separation between HM and FM layer due to the MgO layer alters the effective momentum transfer. A second approach is to use a non uniform composition of HM, e.g. $Pt_x(Ir, Au, W)_{1-x}$ [51, 52]. It has been seen by using a composition of $Pt_x(Ir, Au, W)_{1-x}$ that the iDMI increases with increasing x from 0 to 1. The main fabrication challenge is growing high quality B20 thin films on heavy metals and underlying the MgO.

3.2 Role of Anisotropy in Skyrmion Dynamics

From Eq. 3.8, if we increase ρ, ψ_c would decrease. One way to increase ρ is by reducing the anisotropy K_u and thus D_c (Eq. 3.9). We can gate control the skyrmion size through Voltage Controlled Magnetic Anisotropy (VCMA), in effect, voltage gating the Stark shift of the bond between the magnet's d_z^2 orbital and the oxygen p_z orbital of an oxide layer like MgO grown on the side of the sample opposite the HM layer (Fig. 3.3). The equation describing the perpendicular magnetic anisotropy variation with gate voltage in a VCMA set-up is

$$K_u(V) = K_u(0) - \xi V/t_{ox}t_{FM} \tag{3.10}$$

with t_{ox} the oxide thickness and ξ the VCMA coefficient. This means with a gate voltage, we can change the anisotropy and D_c, the size ρ of the skyrmion, the dissipation tensor $\mathcal{D}_{xx}$ and ultimately the critical angle ψ_c - making the skyrmion converge to a different lane. Assuming a thickness of 1 nm for oxide and FM layers, we would need a $\xi = 50\ fJ/Vm$ to get a $10^5\ J/m^3$ change in anisotropy per 1V. ξ of 50-100 fJ/Vm has been achieved for CoFeB of 1 nm thickness [53, 54], whereas by doping FM/oxide interface ξ larger than 100 fJ/Vm has been reported [55, 56], suggesting that our device parameters are quite realizable for lane control. To get a higher separation of lanes, we can choose a smaller λ term in Eq 3.4. This can be done by making the doping x variation slower in Fig. 3.3a, or using Pt with a slower thickness variation, Fig 3.3b.

3.3 Self Focusing

Fig. 3.4 shows how skyrmions can be made to self-focus into a set of prefabricated racetracks using a VCMA gate [57]. Anisotropy in the fabricated lanes is $K_u = 190kJ/m^3$, separated by regions with higher magnetic anisotropy $K_u = 220kJ/m^3$. While the skyrmion domain angle evolves during transport along y, the VCMA gate changes the local anisotropy and alters the bending of the skyrmion track, attempting to set them into alignment with the racetracks. The VCMA gate can change the anisotropy of the magnetic film under it, enough to bend the skyrmion path towards one of the lanes. The competition between attractive force from the lanes vs. Magnus force in region 2 determines which lane a skyrmion will converge to. When the alignment is not perfect (non-resonant skyrmion), the skyrmions instead enter the region between the lanes. The lane locations and relative anisotropies are designed so the skyrmions entering the regions in between the tracks see a Magnus force in the $-\hat{y}$ direction, as well as an attractive force towards the nearest racetrack. The net force will determine which track the non-resonant skyrmions finally converge to. Once they enter a lane, the repulsive force from the interstitials cancels out the Magnus force and the skyrmions stay in lane. Since the interstitials have higher anisotropy, even skyrmions which miss the lanes eventually end up in one of the lanes whereupon their combined anisotropy repulsion and Magnus force vanishes again. As a result, we get a stepfunction-like quantized behaviour (Fig 3.4b) for the final y coordinate of the convergent skyrmion lanes as a function of the VCMA engineered anisotropy, implying a robust well controlled scheme for directing skyrmions into the lanes. We emphasize that this ability to control lanes dynamically is unique to skyrmions with flexible domain angles, and is not achievable with domain walls. To see the thermal effects on skyrmion movements we performed micromagnetic simulations at 300 K temperature. The thermal effect was simulated by using the fluctuating thermal effective field as is implemented in the Mumax3 program[45].

$$\boldsymbol{H}_{thermal} = \boldsymbol{\eta}(step)\sqrt{\frac{2\alpha k_B T}{M_s \gamma \mu_0 \Delta V \Delta t}} \tag{3.11}$$

Where $\boldsymbol{\eta}$ is a random vector from a standard normal distribution whose value is changed after every time step. ΔV and ΔV are cell volume and time steps of the simulation respectively. k_B is the Boltzmann's constant and T the temperature. γ is the gyromagnetic ratio and μ_0 is permeability of vacuum. The material parameters

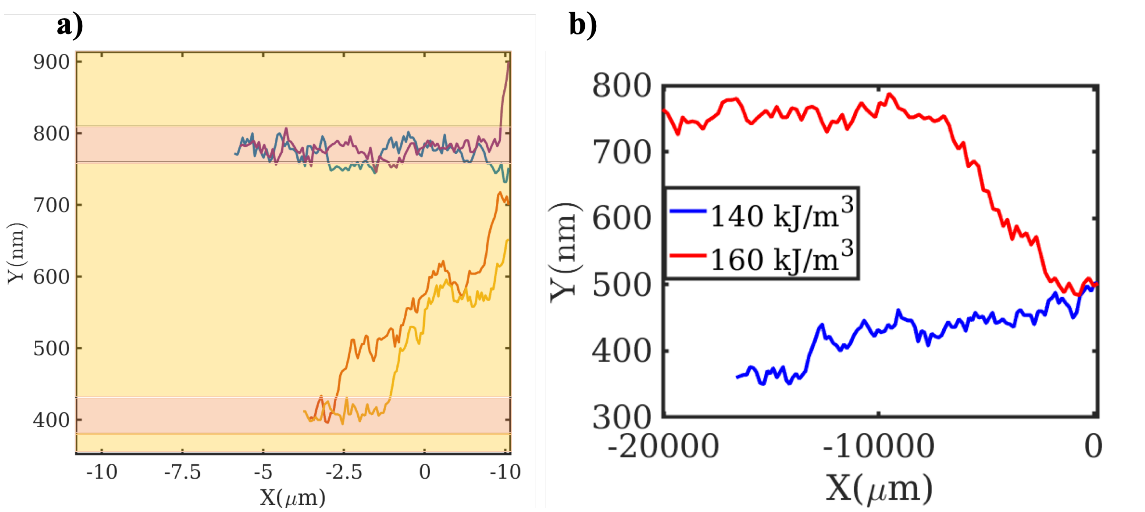

Figure 3.5: Skyrmion path at 300 K temperature simulation.a) Depending on the entry location of skyrmion, they will be going into lane 1 or 2. Yellow region has $K_u = 160kJ/m^3$, orange lanes have $K_u = 150kJ/m^3$ b) Self converging of skyrmions for two different anisotropy. The separation in their path is significantly larger than the fluctuations of skyrmions. This would make the device reliable even at room temperature. The iDMI decreases linearly from top (y = 1000 nm, $D_{int} = 0.37mJ/m^2$) to bottom (y = 0 nm, $D_{int} = 0.25$). The simulations were done at $T = 300\ K$

used for these stochastic simulations are as follow: $M_s = 300\ kA/m$, $A_{ex} =$ 16e-12 J/m, $D_{bulk} = 1.1\ mJ/m^2$, $\alpha = 0.2$, $\Delta V = 1\ nm^3$, $\Delta t = 1\ fs$. Fig. 3.5-b shows that the standard deviation in y-coordinate after self-focusing is around 15 nm when the initial skyrmion K_u is 140 kJ/m^3, and around 10 nm for $K_u = 160$ kJ/m^3, in close agreement with the skyrmion radius (note that these K_u values are from the outside starting point, and distinct from the K_u of the lanes, which are held constant in our simulations). As long as the separation of lanes is much larger than this standard deviation, the proposed device in this chapter should work reliably.

3.4 Summary

In this chapter, we have shown a dynamic method of controlling the skyrmion movement. In the literature, other methods of achieving self convergence have been investigated, but the self convergence is not dynamic or needs extra-fine turnings. The advantage of our method is the ability to achieve multiple converging lanes. In addition, we can dynamically control the position of converging lanes and skyrmion movement. The self convergence would circumvent some of the extra fine-tuning needed compared to other methods. By using a local VCMA gate, we showed an added degree of flexibility that can be achieved, which in turn can be used to dynamically manipulate the logic flow. The existence of multiple convergence lanes makes it possible to do more complicated logic operations compared to the racetracks proposed in the literature. We have also provided a quasi analytical method to predict the convergence lane, which matches reasonably well with the simulations results. Finally, we performed room temperature simulations which showed the robustness of the proposed method with respect to thermal effects.

Chapter 4

Skyrmion Applications

In this chapter, we focus on skyrmion applications. In particular, we look at two main application concepts:

1. Reconfigurable logic based on skyrmion racetrack.
2. Wavefront memory for racelogic operations.

We devote one section to each of the application concepts mentioned above. We design the overhead circuit for each application and calculate the energy consumption of the circuit. Additionally, we study the reliability of the proposed devices. This chapter is partially reproduced from [58] co-authored with Mohammad Nazmus Sakib, Samiran Ganguly, Mircea Stan, Matthew W Daniels, Advait Madhavan, Mark D Stiles and Avik W Ghosh.

4.1 Reconfigurable Logic

Skyrmions, compared to domain walls, benefit from their ability to move in two dimensions. This extra degree of freedom has not been fully utilized in the literature, especially for possible device applications. In this section, we exploit this extra degree of freedom to design a CMOS-skyrmion hybrid circuit for basic and derived logic gates using only one skyrmion. We also propose a novel approach for a reconfigurable logic design using the proposed basic and derived logic gates. We perform micromagnetic and SPICE simulations and show that the proposed approach is highly reliable compared to recently published skyrmionic logic/reconfigurable logic devices. We also show the sources of energy consumption in skyrmionic devices for conservative and non-conservative approaches and show that the proposed approach consumes minimum energy in most cases. Our simulation results show that the racetrack consumes only a fraction of the overall energy, and we also show how the energy-delay product (EDP) of a skyrmionic circuit can be improved with higher-speed skyrmions.

Reconfigurable hardware fabric offers increased performance per Watt than general-purpose processors, and at a lower non-recurring engineering cost than ASICs. Reconfigurability enables workload acceleration while maintaining hardware homogeneity. Modern reconfigurable hardware (FPGAs) make use of SRAM cells to store a configuration. Logic blocks resemble Look-up Tables (LUTs) that use volatile SRAM to store logic function data. While advantageous for re-programmability and manufacturing simplicity, the use of SRAM cells leads to large area overhead and volatility. FPGAs using non-volatile memories (NVMs) are getting a lot of attention as the NVMs can be the embedded memory blocks and play a vital role in programming bits, ensuring zero boot-up delays, energy-efficient, and secure real-time reconfigurability [59]. Thus, there is an ongoing effort in the research community to use different non-volatile memory technologies to design FPGAs [60, 61, 62, 63].

This work presents a reconfigurable logic design using skyrmionic racetracks that have the potential to bring energy efficiency in non-volatile FPGAs, thus eliminating a number of security concerns for programming the FPGA at power on. As skyrmions can move in two dimensions, they have an advantage over magnetic domain wall devices [1]. There are methods in the literature to use multiple or single skyrmion with fine-tuning of parameters to take advantage of the skyrmion 2D movement [64, 65, 66].

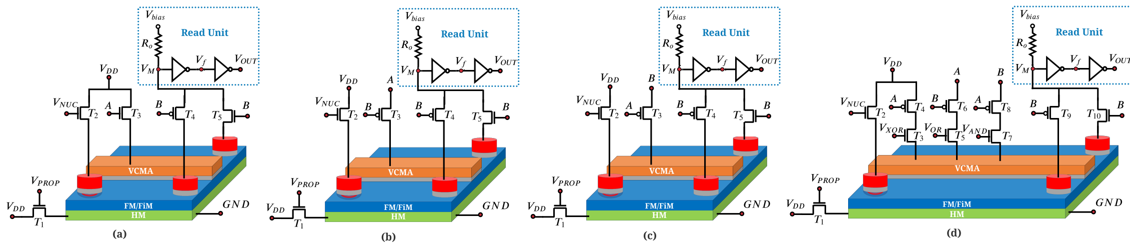

Figure 4.1: (a) XOR logic gate schematic, (b) AND logic gate schematic, (c) OR logic gate schematic and, (d) Reconfigurable logic gate schematic.

Here we are suggesting a reconfigurable logic device based on reshuffling a single stable skyrmion,i.e., a conservative process that bypasses the need for multiple energy hungry nucleation/annihilation processes. The proposed design is also suitable for a non-conservative approach where skyrmions need to be annihilated and re-nucleated before performing a new logic operation.

4.1.1 Proposed Reconfigurable Logic Circuit

First, let us look at the detailed circuit description of the proposed reconfigurable logic device. We exploit the 2D dynamics of skyrmions as well together with the CMOS control circuitry to perform basic and derived logic operations. The VCMA gate placed at the middle of the racetrack divides the racetrack into two lanes. We define these lanes as top and bottom lanes. During a logic operation, the skyrmion either goes to the top or the bottom lane depending on the VCMA gate state, and we call this process the lane selection process. The input conditions control the lane selection process by controlling the ON/OFF condition of the VCMA gate.

The skyrmion logic is set by the competition between the transverse Magnus force that naturally moves a skyrmion from the lower to upper lane in the forward (and reverse in the backward recovery) step, VCMA gate that raises an inter-lane barrier and prevents that cross-over, and thermal fluctuations that randomize the

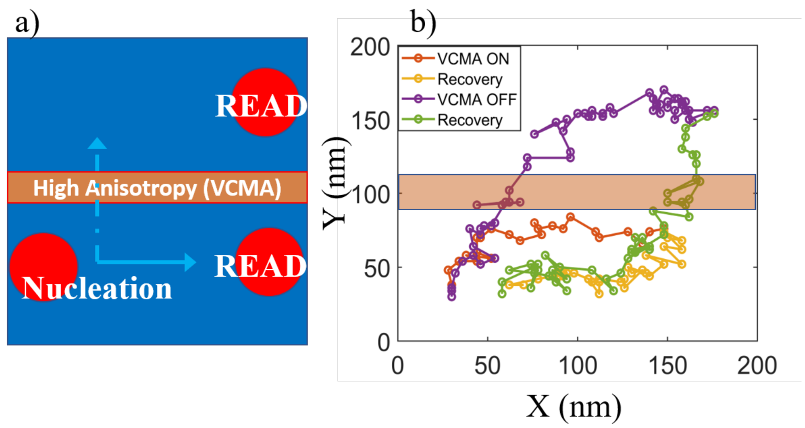

Figure 4.2: (a) The device structure from a top view. Red circles are MTJs responsible for nucleation and read. (b) Micromagnetic simulations for VCMA ON/OFF and their corresponding recovery process at room temperature.

motion under ambient conditions but will need to be circumvented, by making sure the drive current and VCMA strength are significantly larger. A typical simulation trace (Fig. 4.2b) shows this is indeed possible.

For skyrmion detection, we place two detection magnetic tunnel junction (MTJ) stacks at the ends of the top and bottom lanes of the racetrack. Either one of the top and the bottom lane MTJs is connected to the read unit during a logic operation depending on the applied input combinations. We call this process the MTJ selection process. The read unit provides the output depending on the presence/absence of the skyrmion under the selected MTJ. If there is a match between the lane selection process and the MTJ selection process, the output is high, else it is low. We size the read unit access transistors in such a way that we get sufficient voltage swing at the buffer input node M, V_M. The buffer then amplifies node voltage, V_M to either high or low. We show the truth table for all the basic and derived logic gates in Table 4.2.

To increase the reliability at higher currents hence lowering the operating time, the edges can be engineered to have a lower possibility of annihilation by methods

Table 4.1: MATERIAL PARAMETERS FOR SIMULATION for CoFeB/Pt structure [2]

Parameter	Value
Gilbert damping constant (α)	0.2
Saturation magnetization (M_s)	6×10^5 A/m
Magnetic anisotropy (K)	600 kJ/m^3
Dzyaloshinskii-Moriya interaction strength (D)	2.5 mJ/m^2
Exchange stiffness (A_{ex})	15×10^{-12} J/m
Domain wall width ($\Delta = \pi D/4K$)	7.0 nm
MTJ diameter	30 nm
Bare TMR	$\approx$ 400 %
FM width (W), length (L), thickness (t_{FM})	(200 $\times$ 200 $\times$ 1) nm
HM thickness	1 nm
$\rho_{HM}(\Omega.m)$	2.5×10^{-7}
Spin hall angle θ_{sh}	0.15
Spin polarization P	0.8
Skyrmion Radius and wall width	16.5 nm [67, 58]
VCMA Coefficient	100-200 fJ/Vm
Nucleation MTJ resistance	0.5-2 $k\Omega$
Minimum Nucleation current	8×10^{11} A/m^2
Minimum VCMA voltage	0.5 V
Driving current density	8-15$\times 10^{10}$ A/m^2
Minimum Annihilation current density	2$\times 10^{11}$ A/m^2
Speed	80m/s to 150m/s

such as raising the edges or increasing the anisotropy at the edges [30]. However, this would add to fabrication difficulties which would be a trade-off that should be taken into account. We move the skyrmion back to its initial position for the conservative approach before applying different input conditions. It is worth mentioning that the proposed racetrack-CMOS hybrid circuit can perform all the basic and derived logic operations with minimal change in the biasing conditions. Only the biasing conditions change while performing different logic operations. The proposed design is also suitable for both conservative and non-conservative logic with skyrmion. The skyrmion nucleation unit shown in Fig. 4.1 can be disregarded for the conservative approach as we can assume a pre-nucleated skyrmion at the beginning of the racetrack.

Table 4.2: Truth table of the proposed reconfigurable logic.

A	B	$VCMA$			$LaneSelection$			MTJ	V_{OUT}		
		AND	OR	XOR	AND	OR	XOR		AND	OR	XOR
0	0	OFF	OFF	OFF	Top	Top	Top	Bottom	0	0	0
0	1	ON	OFF	OFF	Bottom	Top	Top	Top	0	1	1
1	0	OFF	ON	ON	Top	Bottom	Bottom	Bottom	0	1	1
1	1	OFF	OFF	ON	Top	Top	Bottom	Top	1	1	0

XOR Operation

We first explain the XOR logic operation. In the case of XOR operation, one of the inputs (A) is connected directly to the gate of the transistor T_3 that controls the ON/OFF condition of the VCMA gate. The other input (B) is connected to the gate of the transistors, T_4 and T_5, respectively. The VCMA gate will be in the ON (OFF) state when the input A is 1 (0). On the other hand, the bottom (top) lane MTJ will be connected to the read unit when the input B is 0 (1). When the input A is high, the skyrmion will move along the bottom lane until it reaches under the read MTJ stack. If the input B is low at that time, the bottom lane MTJ will be connected to the read unit, and the output will be high as the skyrmion will be under the bottom lane MTJ stack. On the other hand, if the input B is high, the top lane MTJ will be connected to the read unit, and the resistance of the MTJ will be in the parallel state due to the absence of skyrmion under the MTJ. The voltage at node M, V_M will be low, ensuring 0V at the output node, V_{OUT}.

AND Operation

The lane selection process is different for AND operation, while the MTJ selection process remains unchanged. We use a pMOS transistor instead of an nMOS transistor to control the state of the VCMA gate. We connect the input A and B to the gate and source, respectively, of the pMOS transistor T_3. The VCMA gate will be in the ON state if the transistor, T_3 is ON (B = 0) and the voltage at the source of the transistor is high (A = 1). Thus, the skyrmion will be in the bottom lane only for the input combination when input A is high and input B is low. In all the other three cases, the skyrmion will be in the top lane. However, the top MTJ is connected to the read unit only when the input B is high. Thus, the skyrmion only will be under the selected MTJ only when both the input is high, ensuing successful AND logic computation.

OR Operation

The racetrack and the control circuitry to perform OR operation is similar to the AND operation. The only difference lies in how we control the VCMA gate state. We connect the input A and B to the source and gate of the transistor T_3 which is exactly the opposite input connections while performing the AND logic operation. Thus, the transistor T_3 is only ON when the input B is low. However, the VCMA gate will be in the ON state if the input A is high while the transistor T_3 is ON. Thus, the skyrmion will be in the bottom lane when the input A and B are high and low, respectively. As the MTJ selection process is unchanged, the bottom lane MTJ will be selected for the input condition of 1 and 0 (A, B). Thus, the output will be high due to the matching between the MTJ and lane selection process. Apart from the above-mentioned condition, the skyrmion will be in the top lane due to the OFF state of the VCMA gate. Thus, there will be a mismatch between the lane selection and the MTJ selection process for the input condition of 0 and 0 as the bottom lane MTJ will be selected at that condition returning a 0 at the output node, V_{OUT}. Thus, we can perform the logical OR operation just by changing the input connection of the CMOS-skyrmion hybrid circuit used in the logical AND operation.

XNOR, NAND, and XNOR Operations

We can perform XNOR, NAND and NOR operations by using the XOR, AND and OR circuits in two different methods. One method involves initializing the the MTJ fixed layer state as anti-parallel state while using the same circuit. Thus, if there is a mismatch between the MTJ selection and lane selection process, the output will be high and low otherwise.

The second method involves a slight change in the read unit circuit. If we use one inverter instead of a buffer in the read unit, the same circuit used in XOR, AND and OR operations will perform XNOR, NAND and NOR operations. However, the inverter needs to be sized accordingly to ensure that the node voltage, V_M is amplified correctly.

Programmable Logic Block

We design a programmable logic block by cascading the control circuitry for the VCMA gate state. We use the same racetrack structure, MTJ selection process, and the shared read unit. We add an extra NMOS transistor in series with each of the VCMA gate control units for each logic operation. The transistors, T_3, T_5, and T_7 will be ON while performing the logical XOR, AND, and OR operations (see Fig. 4.1 (d)). For example, in the case of XOR operation, only the transistor, T_3 will be ON and the other two extra transistors, T_5, and T_7 will be OFF. Now, the equivalent circuit of reconfigurable XOR will be similar to the XOR circuit as shown in Fig. 4.4 (a) with an added switch. Reconfigurable OR and AND operations will also follow the same trend. We can also perform programmable XNOR, NAND, and NOR operations with the same circuit by employing any one of the two methods explained section III (D).

4.1.2 Reliability of Skyrmion-based Logic Device: A case Study

In devices that are based on skyrmion-skyrmion repulsions, such as Fig. 4.4, it is necessary for skyrmions to be confined in a relatively small region. Since the thermal effect is non-topological, this will affect skyrmion movement, especially near the edges, as the skyrmion needs to keep its robustness to repel from them. This would make the skyrmion susceptible to annihilation at the edges or not function as intended at room or higher temperatures. As seen from Fig. 5, in a generic skyrmion-skyrmion-based device at room temperature, skyrmions can be annihilated at the edges or notches. This can be alleviated to some degree by engineering the edges to have higher anisotropy or thickness. But as with all the other 'billiard-ball' logic, the arrival times of the balls (in this case, skyrmions) have to be exact to be reliable; otherwise, it will lead to significant error.

The material parameters chosen here are based on experimental results of CoFeB/Pt and MTJ heterostructures[2]. The secondary parameters (nucleation, annihilation time, and current) are all based on room temperature micromagnetic simulations. Note that these are not necessarily the ideal theoretical parameters. To make a one to one comparison, we will show at the end a comparison with existing devices proposed in the literature using the same parameters. In order to use a magnetic racetrack as part of a general digital circuit, it has to be compatible with fabrication processes. The racetrack geometry we are proposing here is very simple to manufacture as it does not need any fine-tuned notch or barrier. The VCMA gating has already been experimentally demonstrated to be possible to fabricate. The geometry for VCMA is also as simple as possible and avoids the need for fine tunings. We ran temperature-dependent simulations for the proposed device in the temperature ranges of 280 to 350 K. As seen from Fig. 4, the proposed device works consistently

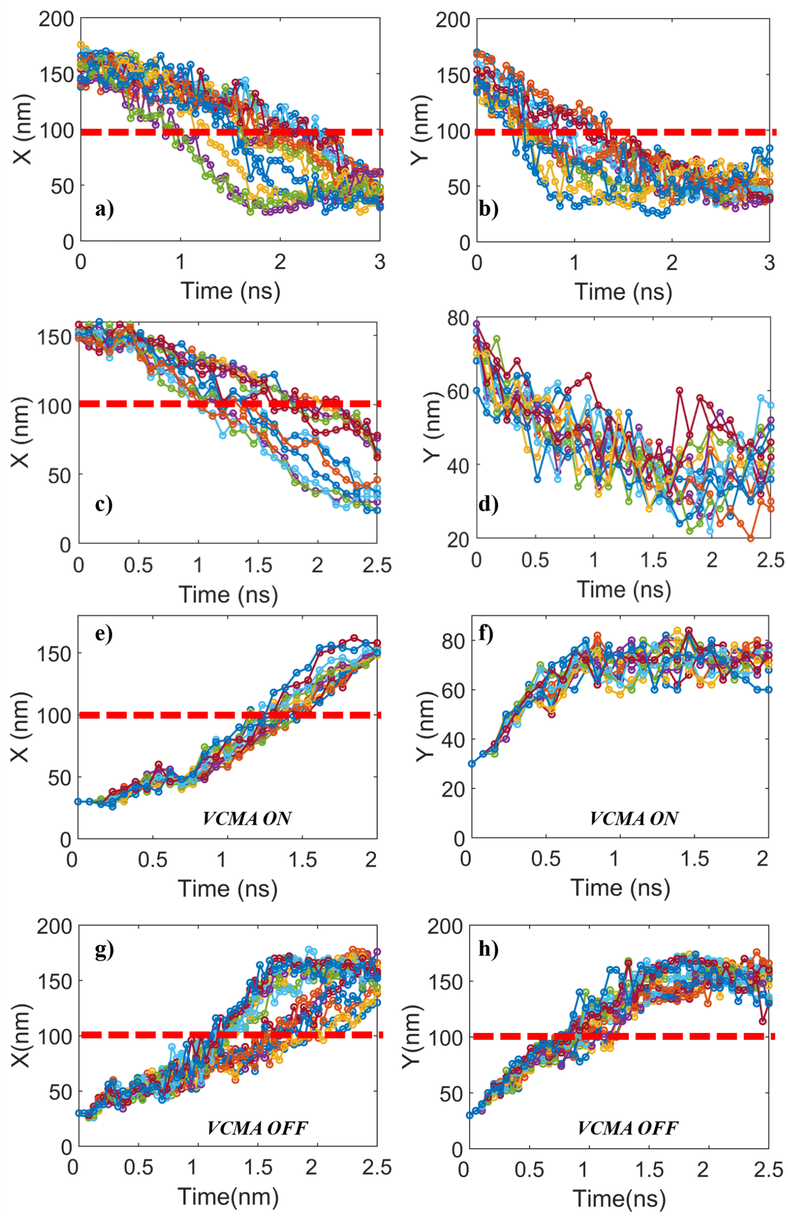

Figure 4.3: X,Y position vs time for temperatures from 280 to 350 K. a,b,c,d are recovery operations for e,f,g,h, respectively. e,f) VCMA is ON, and as we can see, the skyrmion does not pass the VCMA (high anisotropy region). g,h) VCMA off skyrmion to top lane. The dashed red horizontal lines shows the location of VCMA gate which separates the two lanes.

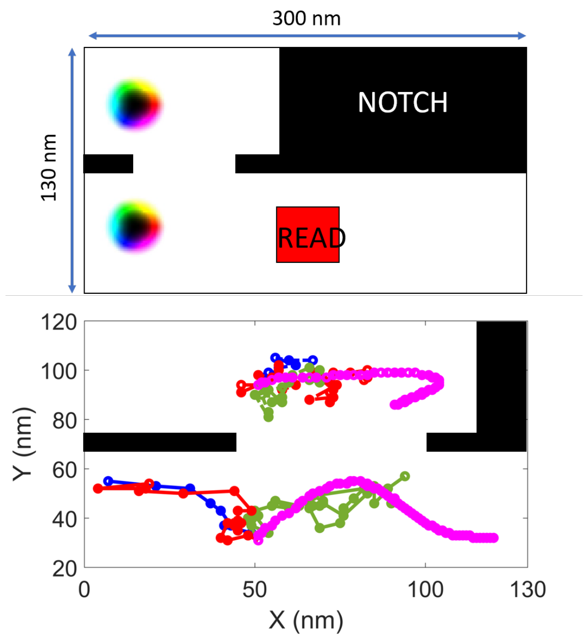

Figure 4.4: Room vs. zero temperature simulations for a two-skyrmion-based logic device. The top figure shows the starting position of skyrmions and the geometry. The simulation is for 1,1 case. The purple lines are for 0 temperature and colored lines for room temperature simulations. The dashed lines are the path of the top skyrmion, and solid lines are the path of the bottom skyrmion. We can see that only at the zero temperature the bottom skyrmion reaches the designated read location; for room temperature simulation, they get annihilated at the notches or the boundaries.

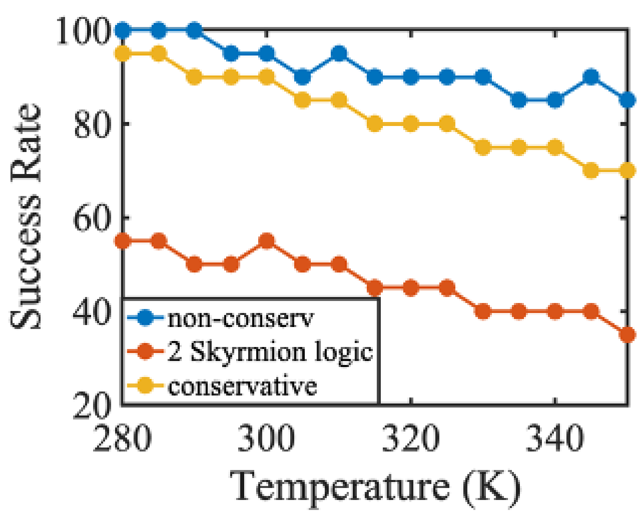

Figure 4.5: The success rate for 3 different skyrmion based logic devices. The skyrmion logic is based on the geometry shown in Fig. 4.4. The success rate is defined as a successful read of skyrmion based on the desired operation.

even above room temperatures. As the skyrmion in our case is not confined to small areas, it has lower chance of getting pinned or annihilated by the edges or boundaries. In the 20 temperature-dependent simulation runs, the skyrmion position at the end of each operation was precisely as intended, indication of a very small error rate. In comparison, as seen in fig 5, a device based on skyrmion-skyrmion repulsion shows a significant error, and for about 50% of the temperature simulations, the device did not work as intended. To quantify the success rate of the devices and make comparison. We define a successful operation as when skyrmion reaches the desired location to have the correct read. As seen in Fig. 4.5, the non conservative approach have the highest reliability closely followed by the conservative approach. The reason for decrease in reliability of the conservative methods is the longer travel time of the skyrmion which increases the possibility of getting annihilated at the edges. For the 2 Skyrmion logic simulations we used the same structure as the Fig. 4.4. Due to the confinement of skyrmions and requirement of fine-tuned skyrmion skyrmion repulsion, the success rate of 2 skyrmion approach is much lower.

4.2 Race Logic Memory

Race logic is a relative timing code that represents information in a wavefront of digital edges on a set of wires in order to accelerate dynamic programming and machine learning algorithms. Skyrmions, bubbles, and domain walls are mobile magnetic configurations (solitons) with applications for Boolean data storage. In this section, we propose to use current-induced displacement of these solitons on magnetic racetracks as a native temporal memory for race logic computing. Locally synchronized racetracks can spatially store relative timings of digital edges and provide non-destructive read-out. The linear kinematics of skyrmion motion, the tunability and low-voltage asynchronous operation of the proposed device, and the elimination of any need for constant skyrmion nucleation and annihilation make these magnetic racetracks a natural memory for low-power, high-throughput race logic applications.

When energy efficiency becomes the predominant metric in computing systems, the choice of information representation becomes increasingly important. A recently proposed temporal coding scheme known as race logic [68, 69, 70] promises orders-of-magnitude energy improvement over classical approaches. In race logic, information is encoded in the relative timing between digital rising edges on different wires, with respect to some temporal reference. This allows each wire to encode multiple bits of information depending on when the rising edge arrives. These rising edges, though encoding multiple bits, incur only a single transition per wire during the course of a computation, keeping activity factors low. This allows conventional Boolean primitives to perform non-traditional operations at a very low energy cost. For example, a single OR gate allows the first arriving edge to pass, effectively performing a two input MIN function,[1] as shown in figure 4.6(a). The rest of the fundamental race logic primitives including MAX, INHIBIT and ADD-BY-CONSTANT gates are shown in figure 4.6. Previous work has mathematically proven the universality of these primitives, constrained by the the physics of causality [71, 72]: any temporally invariant and causal function can be implemented with these primitives.

Such an approach to computation differs from the conventional Boolean approach and results in vastly differing architectures. Computations are generally performed by setting up the problem in a spatially arranged network of operators. Digital temporal wavefronts are presented to the inputs of such an array and the way the wavefront navigates through the network performs the computation. Hence, such an approach maps well to dynamic programming problems, where the spatial data structure of

[1]Note that a multi-bit MIN operation performed with a Boolean magnitude comparator would incur a much higher area and power cost than a single two-input OR gate.

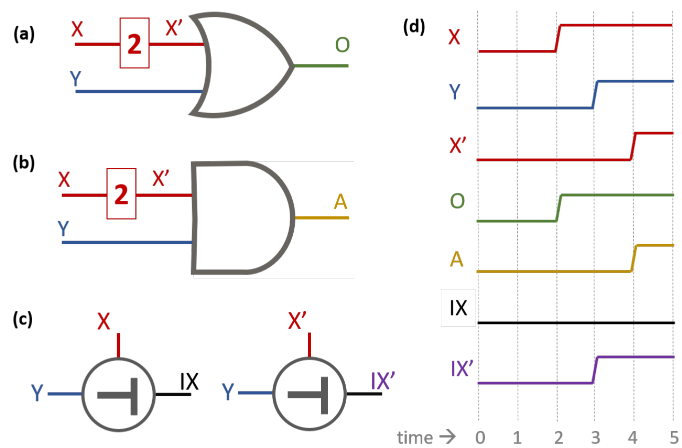

Figure 4.6: Information encoding and primitives of race logic: Panel (a) shows how OR gates and delay elements can be used to perform the temporal MIN and addition by a constant operations. Panel (b) shows the same with an AND gate performing the MAX operation. Panel (c) shows temporal inhibit operation where the inhibiting signals (X and X') inhibit the incoming signal (Y) depending on their relative arrival times. Panel (d) shows the information representation through timing diagrams for the signals used in (a-c).

the problem (like graphs or trees) can be mapped to supporting spatial architectures. Previous work has demonstrated sizeable improvements in performance and energy efficiency for such constrained problems such as decision trees for machine learning (with 4- to 6-bit precision) [69] or directed-acyclic-graph-based genetic sequencing (4-bit precision) [70].

Though a promising approach, one major impediment in implementing race-logic-based temporal computing systems is the need for a memory that can easily store such temporally coded information. Such storage would enable more complicated processing than can be done with simple logic gates. Previously, counter and current starved inverter based circuits have been proposed as tunable delays, but their energy cost, volatility and limited reconfigurability have caused researchers to look at novel approaches to store temporal information. Resistive approaches proposed in [73] suffer from non-linearity between the read and write processes, a problem that is avoided in the magnetic counterparts explored here.

Magnetic devices play key roles in data storage from magnetic tapes to hard disk drives to tunnel junction memories. A racetrack memory [74] is similar to a magnetic disk but without physically moving parts. Translating the magnetic configuration along the track plays the role of moving a magnetic tape. Racetracks with skyrmions [75] can be used to store Boolean information with the presence of a skyrmion at a particular location indicating a one and the absence a zero, for example. This information can be subsequently read by translating the skyrmions past a detector that reads the changing magnetic state through a resistance change. Translation can be achieved by several mechanisms including passing a current through a heavy metal layer as discussed previously [76, 77], that rotates the magnetization. The subsequent local rotations of the magnetization give rise to an effective translation of the magnetization pattern.

We present a design (Fig. 4.7) of a temporal memory cell that linearly converts information from the time domain to a displacement domain. This is done by using current pulses of varying lengths in time to translate skyrmions corresponding distances in space. The linear relationship between pulse length and displacement, thereby encodes the arrival times of the pulses. We present details of this memory, the non-destructive readout, a way to reset memory, and a comparison with conventional Boolean approaches in the next few subsections.

Magnetic memories generally store information in the orientations of the microscopic magnetic domains that reside within the magnetic material. Magnetizations tend to have their energy minimized when the moments point in either direction along a preferred axis. Such a binary configuration naturally lends itself to binary information encoding in which one direction corresponds to 0 and the other to 1. This encoding is used in magnetic tapes, hard disk drives, and magnetic random access memory. In continuous media, the magnetization tends to form domains with the magnetization in two neighboring regions roughly uniform and separated by a narrow region where the magnetization rotates from one domain to the other.

When magnetic materials are fabricated in a 2D geometry, energetic considerations typically prefer that the magnetization lie in the plane. However, it is possible to tune the anisotropies of the material such that the magnetization tends to point parallel to the interface normal, which we label $\hat{z}$. We choose such a material in this work. In the uniform configuration, the magnetization points in the same direction everywhere in a sample, either along $\hat{z}$ or $-\hat{z}$. However, other configurations can exist in a metastable state [78]. One such configuration consists of two stable regions (one along $\hat{z}$ and one along $-\hat{z}$) separated by a localized 180° domain wall. Localized domain walls are generated between oppositely oriented magnetic regions through the balance of exchange and anisotropy forces, the latter of which can arise due to intrinsic magnetocrystalline anisotropy or from magnetostatic interactions [79, 80].

This domain wall divides two regions of uniform magnetization. A skyrmion can be imagined by making the domain wall circular so that it surrounds a region of uniform magnetization (inside the circle) from an region with the opposite magnetization (outside the circle). Both domain walls and skyrmions are topologically protected, meaning that there is a significant barrier to eliminate them, giving them the necessary lifetimes for storage [81]. For skyrmions, the domain wall separating the two regions twists in a particular way, which is described by a topological index known as a winding number. Using ultra-thin ferromagnets (FM) on top of heavy metal (HM) layers breaks inversion symmetry and generates an additional energy term, the Dzyaloshinskii-Moriya interaction (DMI) [82], which stabilizes skyrmions.

Both domain wall and skyrmions have been proposed as fundamental elements of future magnetic memories. For domain walls, ones and zeros are encoded in different magnetization directions; for skyrmions, it is their presence or absence which encodes a bit. In the particular class of memory devices called racetracks [75, 74] that we consider here, the sample geometry is a long thin wire. The information stored in the racetrack can be translated along the wire by passing a current through the wire. Here, this translation is facilitated by the inclusion of a heavy metal layer next to the magnetic layer. An electric current driven through the heavy metal layer injects a spin current, through a spin Hall effect, perpendicular to the FM/HM interface into the magnetic layer, thereby applying a spin-orbit torque to the ferromagnetic layer [83, 84, 85, 25]. This torque can drive skyrmions and domain walls in a variety of ultra-thin magnetic systems at speeds as high as 500 m/s to 1 km/s for relatively low current densities. Possible systems include ferromagnets, antiferromagnets (AFMs), heavy-metal heterostructures, and the two systems of particular interest here: synthetic antiferromagnets [86, 87, 44], and nearly compensated ferrimagnets. For skyrmions to have sufficiently long lifetimes, their energy barriers should be above 30 kT to 40 kT. Such an energy barrier should be achievable by skyrmions of $\approx$ 20 nm diameter. It is also possible to use narrower racetracks, smaller than 100 nm, to have a even more efficient device. The parameters we have used, $\approx$ 50 nm skyrmion diameter and 200 nm racetrack width are to show that the device can be more efficient compared to a CMOS based alternative even without using the state of the art parameters. In our simulations, we consider a racetrack that is either a two-sublattice near-compensated ferrimagnet (FiM) like CoGd or a synthetic antiferromagnet, where the low saturation magnetization gives small-sized high-speed skyrmions that propagate along the track without deflection to the side.

The dynamics of domain walls and skyrmions under the effect of an electronic current is well studied [88, 89], and can be modeled using classical mechanics. In this work we make use of these classical kinemetic behaviors of domain walls and

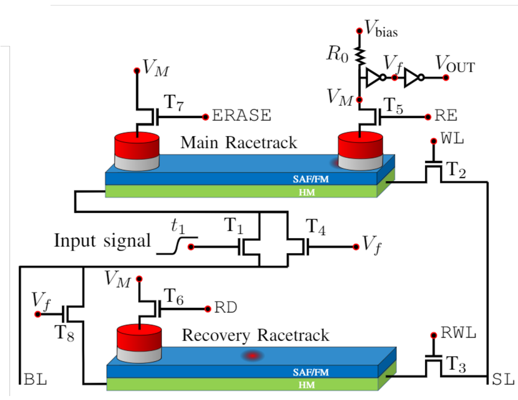

Figure 4.7: Concept and circuit illustration: The general arrangement and detailed description of the circuits of a single column of $N = 1$ cell which can be used to store and play temporal wavefronts. The racetracks consist of a bilayer of synthetic antiferromagnet (SAF) or a ferromagnet (FM) with magnetic tunnel junctions (MTJs) to detect when a skyrmion appears under them. Control lines consist of the bit line (BL), source line (SL), write line (WL), read enable (RE), recovery line (RD), recovery write line (RWL), and erase line (ERASE).

skyrmions by exploiting the simple linear response $x = vt$ between displacement x and time t, mediated by a constant velocity v. To model its motion in synthetic antiferromagnets, we use a collective coordinate description of a rigid skyrmion, that is, we assume the skyrmion texture has only translational degrees of freedom and derive equations for these from the governing LLG equations. We assume that the only driving forces on the skyrmions come from spin orbit torques arising from the spin Hall effect (spin Hall angle Θ_{sh}) in the heavy metal layer.

The resulting Thiele equation gives an instantaneous speed for the skyrmion [90, 88]

$$v = \frac{\pi\gamma\hbar}{2e} \frac{I_d\Delta}{\sqrt{(4\pi)^2\langle N\rangle^2 + \alpha^2\mathcal{D}_{xx}^2}} \frac{\Theta_{\text{sh}}}{\Sigma_i t_i M_{s_i}} j, \tag{4.1}$$

where j is the electrical current density in the heavy metal layer, t is the thickness of that layer, Δ is the characteristic domain wall length, M_s is the saturation magnetization in each layer of the synthetic antiferromagnet, α is the Gilbert damping, and

γ is the gyromagnetic ratio. Two characteristic properties of the skyrmion texture are the (integer) winding number $\langle N \rangle = (4\pi)^{-1} \int \mathbf{m} \cdot (\partial_x \mathbf{m} \times \partial_y \mathbf{m}) \, \mathrm{d}x \, \mathrm{d}y$ and the longitudinal component of the dissipation tensor $\mathcal{D}_{xx} = \int (\partial_x \boldsymbol{m})^2 \, \mathrm{d}x \, \mathrm{d}y$, which provides a kinetic friction force for the moving skyrmion. The direction of the skyrmion motion is determined by the ratio of $4\pi\langle N \rangle$ to $\alpha\mathcal{D}_{xx}$. Because of the off-diagonal response of a skyrmion's velocity, $\alpha\mathcal{D}_{xx}$ ends up being principally responsible for the longitudinal skyrmion motion along the track while the winding number $\langle N \rangle$ gives a transverse Magnus force. Finally, the factor I_d accounts for the spatially varying response of the skyrmion due to its spin texture; this term can be approximated as $I_d \approx e^{-r/\Delta} + \frac{\pi r}{\Delta}$ in rigid skyrmions of radius r, where r is defined by the $m_z = 0$ contour [90]. Note that, contrary to ferromagnetic skyrmions, skyrmions in synthetic antiferromagnets are not expected to experience a Magnus force, due to cancellation between the two oppositely magnetized layers [91]; their net topological charge is $\langle N \rangle = 0$. We develop a circuit module that integrates Eq. (4.1) over time to obtain the instantaneous skyrmion location on the racetracks, which is used to capture the effect of micromagnetic simulations as shown in Fig. 4.8.

The detection scheme is based on the tunneling magnetoresistance (TMR) found in magnetic tunnel junctions. In a magnetic tunnel junction, two magnetic layers are brought close to each other and separated by an insulating layer. The resistance through this material stack depends on the relative orientations of the magnetizations on either side of the insulator. This effect allows the information stored in these magnetic domains to be electrically read out. In this system, the insulating layer is deposited directly on top of the racetrack layer and an additional ferromagnetic layer with a fixed magnetization is deposited on top of that. The resistance measured by this detector changes when there is a skyrmion in the racetrack below the tunnel junction.

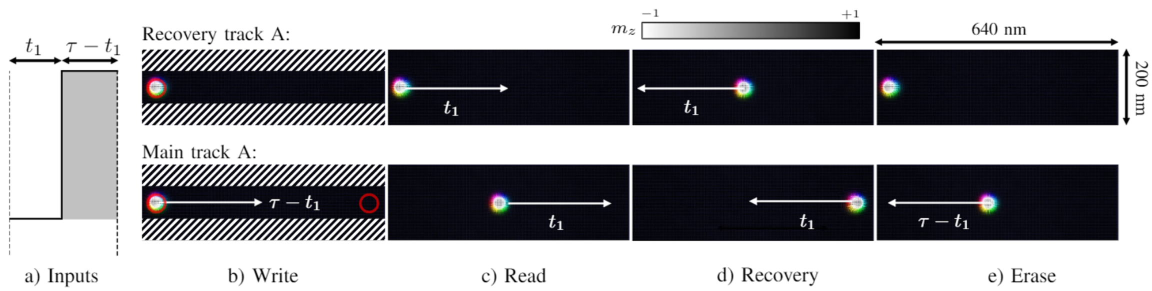

Figure 4.8: (a) An example of a waveform presented as input to be stored by the memory cell. (b-e) Four operational phases of the racetrack temporal memory from a micromagentic simulation. The figures show a background of up-spin magnetic material (black) with a down-spin skyrmion (white); color indicates the in-plane spin orientation. In each phase, the skyrmion location is shown at the beginning of that phase while the arrows point to the location of the skyrmion at the end of the phase. The red circles in the first column indicate the magnetic tunnel junction (MTJ) placement, and the patterned area of the racetracks represents an energy barrier. Amplified repulsion from edges helps keep the skyrmions on their path to the read MTJ locations while preventing them from annihilation or pinning at the edges.

A cell of the proposed magnetic skyrmion based temporal memory, comprising of two parallel racetracks, is shown in Fig. 4.7. The full memory consists of N such cells interfaced with an N channel data bus on which the input wavefronts arrive. The linearity of skyrmion displacement with the drive current pulse length is central to storing temporal data into a linearly mapped spatial skyrmion arrangement on a racetrack. The operating principle of the memory is simple. After a write operation, the temporal location of the incoming edge in the computation window should be mirrored by the spatial location of the skyrmion in the racetrack as shown in Fig. 4.8. Hence when the memory is read, the spatial displacement of the skyrmion leads to a corresponding temporal signal, faithfully reproducing the relative times of the incoming edges. This is done in the following way.

The temporal window of computation is defined as τ, and given a fixed current density of operation, this determines the length of the track $L = \tau v$, where v is the velocity of the skyrmion at the given current density. We assume an erased array to begin with, and a pre-nucleated skyrmion at its origin to avoid skyrmion nucleation costs which are generally understood to be expensive [83], although recent work [92] suggests this may not be prohibitive. During the write process, an incoming rising edge triggers the movement of the skyrmion along the track for a time corresponding to $\tau - t_1$. During the read process, the same current density, hence velocity of the skyrmion, causes a rising edge at the output at time t_1. Though conceptually straightforward, there are some engineering challenges that need to be addressed.

First, readout of such a memory changes the skyrmion position, leading to loss of the state, resulting in a destructive read. We fix this problem by adding a recovery track which saves the skyrmion state. This adds a process known as the recovery operation that restores the previously written value back to the racetrack. The use of a recovery track doubles the complexity of the memory. There are almost certainly other solutions to making a non-destructive memory and some might be less complex but we have not identified one. Second, the supporting circuitry must be developed that allows reliable operation of such a memory, which depends on being able to sense the arrival of a skyrmion with magnetic tunnel junction based readout circuits. These circuits are shown next. Third, such sensing circuits can be designed such that they are shared, hence improving the area and energy efficiency of such a memory. Last, such a memory should be able to work in the presence of non-idealities of the magnetic material. The next section discusses the non-idealities and their effects in detail.

Write Operation

The circuit for the write operation is shown in Fig. 4.7. As described before, we assume pre-nucleated skyrmions in the starting position of the main racetrack and the recovery racetrack as the initial condition for the write operation. Note that the write

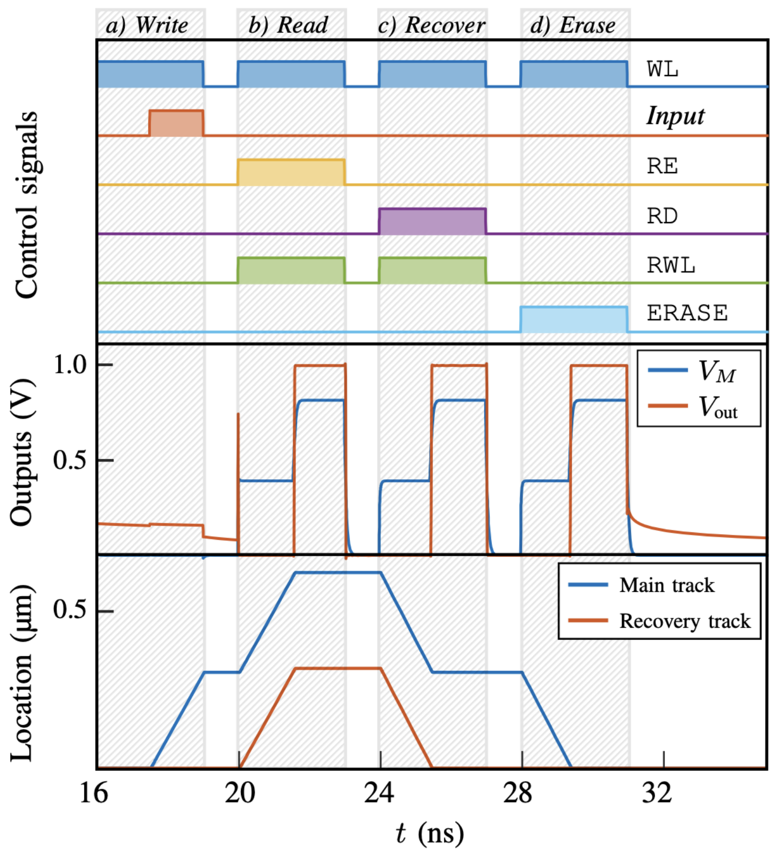

Figure 4.9: Control signals, output signals, and skyrmion positions on the two tracks through four phases memory cell operation. Top: control bits for the write line (`WL`), read enable (`RE`), recovery line (`RD`), recovery write line (`RWL`), erase line (`ERASE`), and the incoming signal. The middle panel shows the synchronizing signal V_{OUT} and the node voltage V_M. The bottom panel shows the instantaneous skyrmion positions on the tracks. The four operational phases are highlighted with gray boxes. a) `WL` drives the skyrmion along the main racetrack, once the input arrives. b) `WL` and `RWL` drive the main and recovery skyrmions, respectively, until the main track skyrmion reaches the MTJ read stack, which is enabled by RE. The resulting resistance change in the MTJ, detected via the feedback voltage V_f (inverse of V_{OUT}), halts the drive currents through the tracks. c) `WL` and `RWL` drive the main and recovery skyrmions as in the read operation, but with the relative polarity of source and bit lines inverted to enable a reverse drive current. Motion stops when the recovery track skyrmion is detected by the `RD`-enabled MTJ stack, restoring the original position of the main track skyrmion before the read operation. d) The `ERASE` signal drives the main skyrmion back to the origin point until it is detected and the drive current is turned off. V_{bias} is held constant at 1.2 V during the read, recovery, erase operations.

operation involves only the primary/main racetrack and not the recovery racetrack, hence only transistors T_1 and T_2 are turned on. The write operation corresponds to shifting the skyrmion in the primary racetrack by the application of the write current (Fig. 4.8b.), resulting in the duty cycle dependence of the final position of the skyrmion. This is done as follows.

A high ($V_{DD} = 1$ V for 45 nm CMOS technology node) voltage is applied to the bit line (BL) and ground to the source line (SL) while the write line (WL) transistor, T_2, is turned on to establish a current path. When the temporally coded incoming rising edge arrives at the gate of the transistor T_1, the write path through the heavy metal layer is turned on and the skyrmion begins its motion along the racetrack. When the incoming signal falls to ground, the transistor T_1 turns off, causing the skyrmion to stop moving and isolating the main racetrack from the BL, successfully storing temporal information spatially. The control signals and corresponding skyrmion motion as a function of time are shown in Fig. 4.9a.

Read Operation

Once the input signal is captured in the racetrack by displacement of the skyrmion to the appropriate position, it can be read. As can be seen in Fig. 4.8c, this read operation changes the skyrmion position and hence is destructive, leading us to employ a corresponding recovery track as shown in Fig. 4.7. During the read operation, the skyrmion in the main racetrack reaches the end of the racetrack, sending off a rising edge, while the recovery track is written with the corresponding t_1 value. This keeps a constant relative displacement between the read and recovery tracks, allowing easy recovery as described in the next subsection.

For the read operation, the circuits are arranged as follows. The BL is biased to high ($V_{DD} = 1$ V for 45 nm CMOS technology node) and SL is biased to ground, similar to the write operation. Transistor T_5 is enabled for readout while the transistor T_1 is turned off. The node voltage V_M is low and V_f is high at the beginning of the read operation due to the low resistance value of the readout MTJ in the absence of skyrmion. This high V_f turns on the identically sized transistors T_4 and T_8 allowing the same current to flow through both the primary and recovery racetrack. As soon as the rising edge that initiates the read operation appears at the inputs to transistors T_2 and T_3, the skyrmion on both racetracks see the same current in the HM layer and exhibit identical dynamics, making them move the same distance along the racetracks as shown in Fig. 4.8c. When the skyrmion along the main racetrack reaches the end of the racetrack, V_M sees an increase in voltage, causing V_f to fall to ground turning off transistors T_4, and T_8 ending the read process. The recovery skyrmion is now frozen at the location corresponding to $t = t_1$ as shown in Fig. 4.8c.

In order to correctly detect the skyrmion, we use MTJ readout circuitry based on the difference in resistance between there being a skyrmion beneath the detector, R_{sk}, or not, R_{P}. This difference can be characterized by an effective TMR, $\beta = (R_{\text{sk}} - R_{\text{P}})/R_{\text{P}}$. A bias voltage V_{bias} with a reference resistor R_0 produces a voltage swing that depends on the effective TMR β at node V_M in the presence or absence of a skyrmion. The voltage at the node V_M is then amplified by an inverter to feed high or low feedback voltage V_f to the gates of the nMOS transistors T_4 and T_8. Note that the readout circuitry is biased in such a pattern that the feedback voltage V_f turns on the transistors T_4 and T_8 during the read, recovery, and erase operations only.

The reference resistance should provide the maximum contrast between the skyrmion and no-skyrmion states under the MTJ. To ensure functionality, R_0 must be between R_{0-} and R_{0+}. In general $R_{0\pm} = \tilde{R} - u\rho \pm \rho\sqrt{1 + u^2 - 2\tilde{R}u/\rho}$, where $\tilde{R} = R_T + (R_s + R_p)/2$, $u = V_{\text{bias}}/V_{\text{min}}$, and $\rho = (R_s - R_p)/2$. V_{min} is the minimum voltage difference between the skyrmion and no-skyrmion states needed at node V_M to ensure switching behavior at V_f, and V_{bias} is the bias voltage. The maximum possible voltage swing is given when $R_0 = \sqrt{R_{\text{sk}} R_{\text{P}}}$. Higher resistances increase efficiency and can be achieved by using a thicker MgO layer in the MTJ. It is essential that the effective TMR be large and the filling of the MTJs by the skyrmions be almost complete because the read-out circuitry begins to function poorly when the effective TMR is below 50 %. Using domain walls instead of skyrmions would give a larger read-out signal at the potential cost of more complicated motion.

Note that though V_M is connected to three different MTJs, only one of them is active in each operating phase. This node and its associated readout circuitry can therefore be shared by these MTJs. This is achieved by controlling inputs to transistors T_5, T_6 and T_7.

Recovery Operation

The recovery operation compensates for the destructive read by restoring the primary and recovery skyrmions to their pre-written values as is shown in Fig. 4.8d. This operation is the opposite of the read operation and is performed almost identically, except with a reversed applied current. Hence, the BL is biased to ground while the SL is biased to high. Using transistor T_6 with the MTJ, the shared readout circuit is triggered when the skyrmion returns to its original location under the MTJ in the recovery track (Fig. 4.9c.) This detects the end of the operation and turns off transistors T_8 and T_4, hence shutting off the current path. After this operation is complete, the skyrmion in the recovery track is restored to its default origin position, while the skyrmion in the primary track is restored to its value before the read. The cell is now ready for another read as described before, or an erase operation.

Erase Operation

The final operation is the erase operation to return the cell to its configuration before any write operations, i.e., the configuration with the skyrmions on both racetracks at the origin. The erase operation is similar to the write operation as only the skyrmion in the main track is moved, but the direction of the drive current and hence skyrmion motion is reversed (Fig. 4.8e.). The ending of this phase is determined by the MTJ at the beginning of the main track. Note that in this phase, the other two MTJs are not required, causing transistors T_5 and T_6 to be disabled, while transistor T_7 can be enabled. As soon as the node voltage V_f of the readout circuitry turns low, the transistor T_4 turns off, signaling the end of the erase operation (Fig. 4.9d.). The cells are now ready to write a new state.

Robustness to parameter variations

The memory is designed in such a way that during the read and recovery operations, only the travel times of the main and recovery track skyrmions matter, not the distances covered by them; and the travel time is controlled by the feedback voltage V_f and as long as the travel time of both the main and recovery track skyrmions is the same, the different velocities in the racetracks will have no impact. For example, if the skyrmion velocities are different in the main and recovery tracks, both the skyrmions will move until the main racetrack skyrmion reaches under the read MTJ stack. Now, during the recovery operation, both the skyrmions will retrace the distances they traveled during the read operation, resulting in the restoration of the skyrmion position (i.e., at the beginning for the recovery track and at the same place where it was positioned after the write operation for the main track).

4.2.1 Performance and Comparison with CMOS

In order to understand and quantify the performance of this wavefront memory cell, we perform detailed circuit simulations using a modular approach. In particular, we construct a complete circuit model using the 45 nm and 16 nm technology node obtained from the Predictive Technology Model [93] for the driving transistors and the dynamics of the skyrmions in the magnetic racetracks. We compare our results to conventional CMOS implementations constrained by the requirements of the application. Race logic has been successfully demonstrated to work well for 4 to 6 bit precision for a variety of applications such as decision trees and DNA sequence alignment[69, 70]. We limit ourselves to a similar precision in order to make a fair comparison.

To describe the magnetic dynamics, our simulations use a Gilbert damping constant $\alpha = 0.1$, saturation magnetization $M_s = 3 \times 10^5$ A/m, magnetic anisotropy $K = 135$ kJ/m^3, Dzyaloshinskii-Moriya interaction strength $D = 1.2$ mJ/m^2, and exchange stiffness $A_{ex} = 7.5 \times 10^{-12}$ J/m. Consequently, the domain wall width is $\Delta = \pi D/4K \approx 7.0$ nm and the skyrmion radius is approximately 24 nm [67]. We use these parameters to model a synthetic antiferromagnet with thickness of $t_{\mathrm{FM}} = 2$ nm for each layer, length of 640 nm, and width of 200 nm. The heavy metal thickness is assumed to be 5 nm. The MTJ diameter is 40 nm with a TMR of ≈ 400 %, based on $R_P = 6.67$ kΩ and $R_{AP} = 33.3$ kΩ. The circuit behaves acceptably provided the bare TMR is greater than 100 %, or an effective TMR of 50 %. With the chosen parameters, the skyrmion size is comparable to that of the MTJ. From the structure of the skyrmion, we compute a 50 % reduction in the TMR to an effective TMR close to 200 %. The reference resistance is taken to be $R_0 = 15$ kΩ, giving a swing voltage of ≈ 425 mV.

The saddle point barrier to skyrmion annihilation is $E_{\mathrm{b}} \approx 23A_{\mathrm{ex}}t_{\mathrm{FM}} - E_{\mathrm{skyr}} \approx 100\ kT$, where k is the Boltzmann constant and T is the temperature. Assuming a mean lifetime to annihilation of [94] $\tau = f_0 e^{E_{\mathrm{b}}/k_B T}$ with $f_0 = 10^{-10}$, the lifetime of these skyrmions is in the range of years at room temperature. While the Magnus force is small in the compensated synthetic antiferromagnet, the wide track requires skyrmion injection right down the middle to hit the MTJ. This constraint can be avoided with narrower racetracks with repulsive edges.

Fig. 4.10 gives the energies consumed for these four operations in each component, for an average case in which the skyrmion is moved to the middle of the racetrack. The bottom panel of Fig. 4.10 shows that the energy consumption is highest in the read and recovery operations, as it involves driving both racetracks, while the write and erase operations, single track operations, consume relatively less energy. For the chosen parameters for the racetrack and the racetrack drive currents ($\approx$ 244 µA), the total energy consumption of the complete cell is $\approx$ 2.8 pJ (45 nm CMOS technology) for the full cycle of the four memory operations, at a 50 % duty cycle—that is, the case where the write process puts the skyrmion midway in the racetrack. This is the average case ($t = \tau/2$) of all possible temporal data recordings in the range $[0, \tau]$. The top panel of Fig. 4.10 shows that the energy consumption in the racetracks themselves (due to Joule heating) is only a minor component of the total energy consumption and is on the order of $\approx$ 45 fJ.

Such a memory cell is only useful if it has advantages over alternatives based solely on CMOS. Here we make a comparison with an equivalent conventional 4 bit CMOS temporal memory by using an up-counter coupled with a latch or an SRAM cell. The up-counter counts ‘clock ticks’ and can thereby digitize a clock delay. An up-counter is built out of multiple positive edge-triggered T-flip flops (TFF) and combinational circuits. Textbook implementations of one such TFF requires

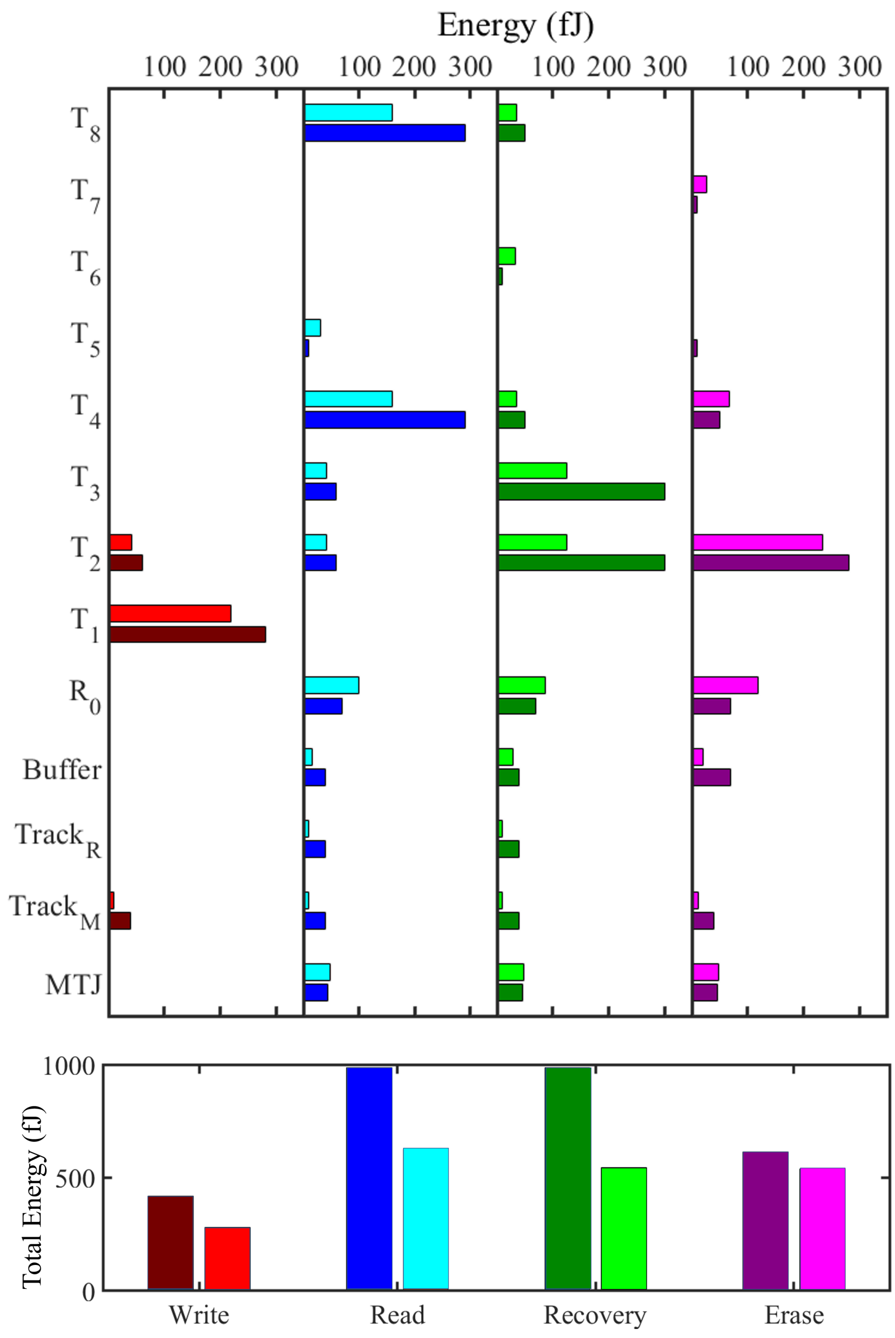

Figure 4.10: Total energy, and energy breakdown per circuit element, for an average case of wavefront capture on a set of 640 nm racetracks. The read and recovery processes consume the most energy because both tracks are active in these operations. In all operations, the largest energy dissipation arises from high overdrive voltage of transistor, with only minimal contributions from Joule heating in the main (Track_M) and recovery (Track_R) racetracks. Darker and brighter color bars show the results done with 45 nm and 16 nm CMOS transistors, respectively.

20 MOSFETs. Our racetracks store 'analog' temporal information, while a counter stores quantized information. For example, a 4 stage counter, which has a $2^4 = 16$ step quantization of temporal data, will require 94 transistors. Coupling them with simple S-R latches to store the memory requires another 32 transistors, yielding a total of 126 transistors. In addition, this scheme stores the data logarithmically and its

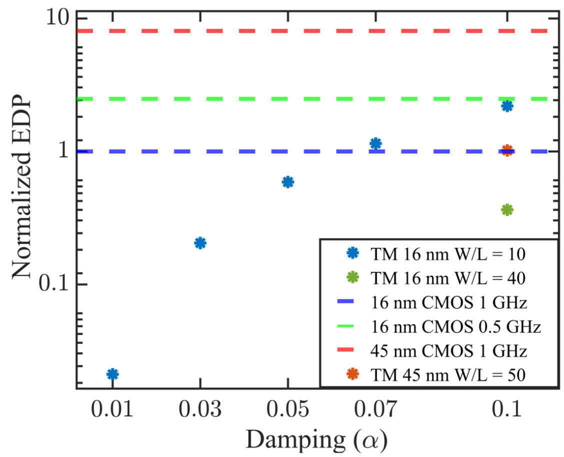

Figure 4.11: Normalized energy delay product (EDP) of 4-bit CMOS counters and four temporal memory cells (TM) with different damping constant with 16 nm and 45 nm transistors (normalized to EDP of 1 GHz 16 nm counter-based CMOS temporal memory).

readout requires either a Boolean decoder circuit increasing the number of transistors (an estimate for a 4×16 decoder requires 172 transistors) or a clock generator driven by latch readout (component count dependent on implementation scheme).

The proposed design can also replay back the temporal data during the recovery operation making the recovery operation another read operation. For low damping ($\alpha = 0.01$), the EDP of the temporal memory is smaller by factors of 32 and 81 compared with the CMOS counterpart working at 1 GHz and 500 MHz clock frequencies, respectively. Moreover, EDP advantage will be even greater for higher numbers of read operations per write operation. The above comparison was made for a full cycle operation where write, read, and erase energies are counted once. When the temporal data is read multiple times per write, everything but the read energy will be amortized. Thus, for 10 and 100 reads, the EDP improves by factors of 74 and 84 respectively. At high damping ($\alpha = 0.1$), the CMOS counterpart has better EDP only when the driving transistor resistance is low for the temporal memory. A higher W/L ratio of the driving transistors decreases the EDP at the cost of increased area; the EDP improves by factors of 3, 11, and 16 when the temporal data is read 1 time, 10 times, and 100 times, respectively, compared to the CMOS counterpart at 1 GHz clock frequency. An additional advantage is the built-in non-volatility of the skyrmion racetrack; the proposed cell can be powered off without losing information for significant lengths of time, compared to the volatile nature of a pure CMOS design. For systems where long term memory is required the proposed memory cell would consume significantly less energy than the counter-based CMOS-only design.

4.2.2 Non-Idealities of Racetracks and Possible Solutions

Our simulations are based on pristine racetracks at zero temperature. In experimental realizations, there will be a number of complications. The most significant constraints on the operation of this memory are non-idealities in the tracks and device variation from track to track. To reliably store and recall temporal signals, skyrmion velocities need to be predictable and narrowly distributed among all tracks. Today, tracks cannot be fabricated with adequate reproducibility to achieve these margins. If applications of skyrmion racetracks become commercially appealing, we expect that such interest would lead to substantial improvement in fabrication quality and make the manufacture of our device realistic. The velocity distribution ultimately limits the precision of the memory and the number of significant bits it can store and recall. We argue below that even four bits of precision could be useful.

Finite temperature and pinning: At finite temperature, skyrmions in close to ideal racetracks undergo rapid diffusion and Brownian motion [95] that would make the racetracks unusable. At the other extreme, both intentional defects such as notches [96] or unintentional ones such as material non-uniformities give rise to pinning centers that can keep skyrmions pinned, preventing thermal diffusion but also preventing the current induced motion necessary for the operation of the racetrack. For the proposed racetrack to be viable, this pinning needs to be strong enough that the skymion remains localized with high probability for a sufficient time. If we require that a skymion remain localized to within 40 nm with probability $1 - 10^{-8}$ for 1 h, the diffusion constant must be less than 10^{-22} m^2/s.

On the other hand, the presence of pinning centers leads to a minimum drive current for predictable motion. Below that drive, the motion is in the creep regime and consists of repeated stochastic thermally assisted depinning and pinning. Reliable racetrack memory requires that the pinning be weak enough to allow low drive current predictable motion but strong enough that Brownian motion is minimized during storage. The study of pinning is still in its infancy with reported diffusion constants ranging from $> 10^{-11}$ m^2/s in optimized material stacks [95] to $< 10^{-20}$ m^2/s [97]. The latter system exhibits predictable current-induced motion [97] for similar current density to what is used in this chapter, suggesting that there is an experimental regime in which the racetrack described here functions as reported. As material fabrication capabilities improve, it may be desirable to control the motion with lithographically designed pinning cites. The memory would then be discrete rather than analog, but such memory is sufficient for a variety of race-logic applications.

These arguments hold for domain walls, but skymions and domain walls are more strongly affected by different types of disorder. Since skyrmions are localized to the center of the racetrack, they are less susceptible to pinning by edge roughness. Domain walls are more extended so they are less susceptible to pinning by the anisotropic grains that can exist in a racetrack [84].

Skyrmion readability: The read-out of skyrmion motion is through the TMR effect of the MTJ as mentioned before. The relative area of the skyrmion under the MTJ is a critical factor for obtaining a sufficiently large resistance swing to control the output swing of signal V_M in Fig. 3. Matching the area can be achieved by using large skyrmions to fill a significant area under the MTJ reader. Using domain walls removes this problem as they can be large enough to provide nearly full MTJ cross-section coverage. Improving the TMR of MTJs would allow smaller skyrmions to be read with sufficient contrast. Another solution is to use additional transistors at the read stage to amplify the smaller voltage contrast provided by a low read TMR, but with a higher area and energy cost.

Parameter Variations: Meaningful comparison of times stored on different write tracks requires a tight distribution of skyrmion velocities on the write tracks. In addition, all of the tracks must be long enough that the fastest skyrmions from the distributions of speeds would not reach the end of a track over the maximum write duration and get annihilated. On the other hand, the requirements for the recovery tracks are less stringent except for constraints on their length. During the read and recovery operations, only the travel times of the main and recovery track skyrmions matter, not the distances they cover. The travel time is controlled by the feedback voltage V_f so that as long as the travel time of both the main and recovery track skyrmions is the same, the different velocities will have no impact. However, to ensure that the recovery skyrmion never gets driven off the end of the track, the recovery tracks need to be long enough that the fastest skyrmion will not reach the end in the time that it takes the slowest skyrmion to travel between the two write track MTJs.

The much faster time scales of CMOS control circuitry compared to that of the current pulses used to move the skyrmion ensures the fidelity of the read process. The considered skyrmion speed is 200 m/s while the transistor switches in picoseconds. The propagation delay of the inverter used in the shared read circuitry is 4 ps (for 45 nm CMOS) during which the skyrmion moves only 0.8 nm. If we incorporate parasitic effects, variations, and the MTJ switching time (time for the V_M to go high), the skyrmion movement will increase. If the isolation time of the racetrack during the read operation becomes 40 ps after incorporating all the delays, the skyrmion will only move 8 nm, smaller than the size of the skyrmion.

Edge annihilation: Skyrmions are susceptible to annihilation by the edges of the racetrack. This can be partially ameliorated by use of wide racetracks, whereby we can avoid the possibility of skyrmion drifting to the edges and getting annihilated due to Magnus effect. This however can worsen the skyrmion readability as this scales up the size of the read MTJs, or makes skyrmions miss the MTJ as discussed above. While the use of synthetic antiferromagnet racetracks with compensation for Magnus force can considerably reduce this issue, use of reflecting edges through anisotropy engineering, such as using ion beam irradiation, or geometry engineering by using thicker edges can also help with this issue [98, 99]. By using reflective edges, the skyrmion will more reliably reach the MTJ position, as the repulsive force from the edges will confine the skyrmion to the middle of racetrack.

All of the issues listed above are common for all magnetic racetracks, an area of active research, and this device will benefit from any future improvements through better fabrication capabilities and novel extrinsic circuit techniques.

Applications of race logic

Race logic performs well against conventional approaches on tasks that involve searching through a large space and that are amenable to a dynamic programming approach. It effectively implements the principle from dynamic programming of optimality, which constrains solutions of sub-computations to be (partial) solutions of the global computation, in turn allowing chaining of temporal computations. Examples of useful computational problems obeying the principle of optimality are shortest paths of graphs and machine classification with decision trees. These applications require decisions to be made at each node in a graph or tree about what computational path needs to be taken next. By mapping the input into temporal edges and by effectively utilizing tunable delay elements, such decisions can be made using simple OR and AND gates on single wires.The precision required of the delay elements by such applications is limited to between 4 to 6 bits. With this limited precision, Ref. [68] shows a 200× energy advantage over conventional limited precision digital approaches. Ref. [70] describes a fabricated chip that performs a similar task at a power level of 70 mW. Ref. [69] performs classification with decision trees at an energy delay product 4 orders of magnitude superior to state of the art.

4.3 Summary

In this work, we utilized a novel technology based on skyrmions and reconfigurable logic architecture in magnetic racetracks to provide energy-efficient memory for temporal computing and Boolean logic operations, respectively. The reconfigurable logic proposal is flexible as we can make use of the same circuit by tuning the control circuitry. We argued that the proposed architecture is more reliable and comparatively easy to fabricate as we are not changing the racetrack structure. The proposed design not only takes advantage of the 2D dynamics of magnetic skyrmion but also takes advantage of the peripheral control circuitry. Apart from the 2D movement of magnetic skyrmion, our approach does not rely on the phenomena such as synchronization of the skyrmion or skyrmion-skyrmion repulsion, which makes the device more reliable.

The proposal for the temporal computing uses the displacement of pre-nucleated skyrmions to store temporal information in magnetic racetracks, avoiding the energy cost required to nucleate them. The readout of this memory is made non-destructive by doubling the number of racetracks to store the information in the second racetrack during the read process. While this increases the energy consumption and area of the memory, we limit the impact by sharing readout and control circuits for the different operations involved in using the memory. The linearity of the stored information with respect to the input limits the circuitry required for translation between the time and displacement domains. By changing the current used to drive the skyrmions, and hence their velocity, these memory cells can be tuned, so their time scale matches the range of input information. Such an efficient memory will greatly expand the problem domain that can be efficiently addressed by timing based computing.

Chapter 5

Positional Stability of Skyrmions

As we saw in previous chapters, the position of skyrmion can directly carry information (temporal memory) or even in traditional racetrack memory, simply the existence of skyrmion would present bit 1 and lack of skyrmion bit 0. It is essential to guarantee the positional stability of skyrmions for reliable information extraction. Using the string method for calculating the minimum energy path (MEP), we compute the energy barriers associated with stabilizing notches along a racetrack. We vary material parameters, specifically, the strength of the chiral Dzyaloshinskii-Moriya interactions (DMI), the notch geometry, and the thickness of the racetrack to get the optimal barrier height. We find that the reduction of skyrmion size as it squeezes past the notch gives rise to the energy barrier. We find a range of energy barriers up to $\sim 45\ k_BT$ for a racetrack of 5 nm thickness that can provide years long positional lifetime of skyrmions for long-term memory applications while requiring a moderate amount of current ($\sim 10^{10}\ A/m^2$) to move the skyrmions. Furthermore, we derive quasi-analytical equations to estimate the energy barrier. We also explore other pinning mechanisms, such as a local variation of material parameters in a region, and find that notched geometry provides the highest energy barrier. This chapter is reproduced from Ref [100] co-authored with Md Golam Morshed, and Avik W Ghosh.

5.1 Brownian Motion

In a skyrmion-based Boolean racetrack memory [101, 21, 58, 102], information is encoded by the presence (bit "1") and absence (bit "0") of skyrmions at a particular position. For an analog domain utilization of a skyrmion racetrack, such as a native temporal memory for race logic [58], the information is encoded directly into the spatial coordinates of the skyrmions that can be translated back into the timing information of wavefront duty cycles carrying out the race logic operations [103]. The positional stability of skyrmions is a critical issue for both of these applications because a randomly displaced skyrmion can alter the bit sequence in Boolean memory applications and change the spatial coordinates hence the encoded analog timings in race logic applications. For reliability, it is essential to guarantee the positional stability of skyrmions for a certain amount of time. For instance, for long-term memory applications, it requires positional stability of years, while for cache memory, hours or even minutes would be sufficient. In an ideal racetrack, skyrmions are susceptible to thermal fluctuations and exhibit Brownian motion leading to diffusive displacement [104, 95]. Moreover, skyrmions show inertia-driven drift shortly after removing a current pulse rather than stopping immediately. One way to control such undesirable motion is by engineering confinement barriers such as defects created by local variations of material parameters and notches etched into the racetrack, which ensures the pinning of skyrmions [83, 105]. Notches can provide a controlled localization of the skyrmion, and using multiple of them in a racetrack allows digitizing the positional information of the skyrmion. It would ensure a deterministic behavior for any skyrmionic device that relies on the position of the skyrmion in the racetrack, ranging from traditional long-term memory applications to temporal computing applications where the temporal data are stored in the spatial coordinates of the skyrmion.

5.2 Imperfect Magnetic Racetrack

The interactions and dynamics of skyrmions with defects and other pinning sites such as notches have been studied over the past few years [105, 106, 107, 108]. References [83, 109] reported skyrmions displacement by the current induced spin-torque with the presence of defects (defects were realized by notches with varying anisotropy). Nucleation of skyrmions in a constricted geometry has been discussed in ref. [110]. Reference [111] used notch to suppress the clogging of skyrmions bit in a racetrack while ref. [112] incorporated notch to do logic operations. Reference [113] discussed the coupling between mobility and breathing mode of skyrmions in a racetrack where periodic notches with varying DMI are placed opposite to each other. Few of the studies have discussed the energy barrier associated with the pinning sites peripherally [104, 114, 115]. Recently, notches have been used to achieve positional stability in skyrmion and domain wall-based artificial synapses [116, 117, 118, 119]. Nonetheless, what is missing is a systematic analysis of a notched racetrack, the mechanics of the energy barrier, and its impact on skyrmion mobility, stability, and unintended nucleation and annihilation which sets its operating limits. The combination of required positional stability and operational current range defines an optimal 'Goldilocks' regime in parameter phase space, which is the focus of this work.

5.2.1 Positional Stability

In this chapter, we systematically analyze the positional skyrmion energy barrier generated by the notches in a magnetic racetrack (Fig. 5.1) using micromagnetic simulations. In particular, we vary the material parameters DMI (varying skyrmion sizes), the geometry of the notches (Fig. 5.2a), and thickness of the racetrack (Fig. 5.2c) to achieve a high tunability of the energy barrier for long-term positional stability of skyrmions. We see that the energy barrier is attributed to the constriction in the skyrmion sizes arising from the notch created in the racetrack. Furthermore, we use a quasi-analytical equation to phenomenologically take into account the effects of the constricted geometry in the energy calculations of a skyrmion (Fig. 5.4b). We see that the quasi-analytical equation can successfully describe the energy barrier calculated from the simulations for various notch sizes and shapes. We also explore other pinning sites such as local variations of material parameters to put the notched geometry into perspective with other types of defects (Fig. 5.5). Moreover, we show the energy barrier dependence on the shape of the notch (Fig. 5.6). Finally, we show that the required unpinning current is small enough for skyrmion-based devices to be integrated with electrical circuits (Fig. 5.7). Our results provide a path forward towards practical, reliable skyrmion-based racetrack memory applications.

5.3 Methods

We perform the simulations using MuMax3 [120], a micromagnetics simulator that solves the Landau-Lifshitz-Gilbert (LLG) equation. The dimensions of the racetrack are length $L = 800\,nm$, width $W = 200\,nm$, and thickness $t_F = 5\,nm$. The simulation mesh is divided into $400 \times 100 \times 5$ grids with a cell size of $2\ nm \times 2\ nm \times 1\ nm$ without considering periodic boundary condition. We note that the choice of cell size is much lower than the exchange length l_{ex} ($\sim 33\ nm$). We use GdCo material parameters such as exchange stiffness $A_{ex} = 7\ pJ/m$, anisotropy $K_u = 50\ kJ/m^3$, saturation magnetization $M_s = 100\ kA/m$ throughout all the calculations unless otherwise specified [121, 122, 1]. We use varying interfacial DMIs to control the size of skyrmions because the DMI can be easily tuned by interface engineering [123, 124]. We calculate the minimum energy path (MEP) using the String method [125]. The basic idea of the string method is to find the MEP by evolving a curve (string) connecting two endpoints along the energy landscape and the reparametrization of the string by interpolation. It is an iterative method that continues until the path converges to the MEP with the desired accuracy. In our simulations, we use 100 iterations to calculate the MEP.

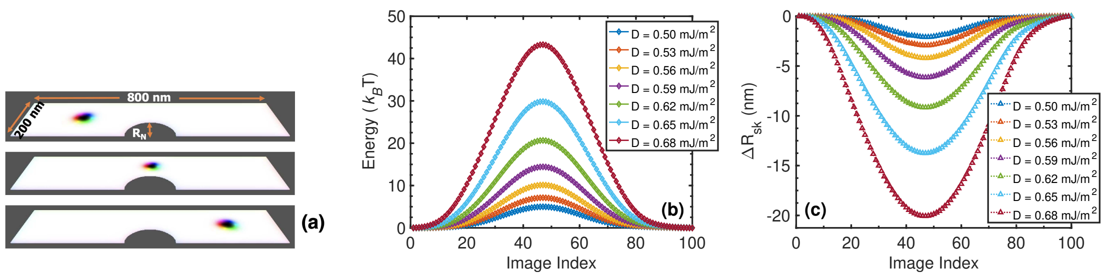

Figure 5.1: (a) Simulated racetrack with notched geometry. Each of the figures represents different snapshots of the skyrmion trajectory along the racetrack, referred to as 'image index'. (b) The energy vs image index for the optimal trajectory of a skyrmion with varying DMIs in a 800 $nm \times 200$ nm racetrack with notch radius, $R_N = 100$ nm. The left valley, peak, and right valley correspond to the image index shown in the top, middle, and bottom panels of Fig. 5.1(a) respectively. (c) Change in skyrmion radius, ΔR_{sk} when the skyrmion passes over the notch. Higher DMIs initiate larger initial skyrmions that undergo bigger shrinkage and larger energy costs when forced through the constriction.

5.4 Results and Discussion

Figure 5.1(a) shows the schematic of a racetrack with notched geometry. We assume semi-circular notches with radius R_N. These are made by removing materials from the racetrack. The snapshots represent different positions of the skyrmion trajectory (referred to as 'image index') along the MEP which maps into the position of the skyrmion along the two sides of the notch. Figure 5.1(b) shows the total energy obtained from the MEP calculations for a racetrack with notch radius 100 nm and

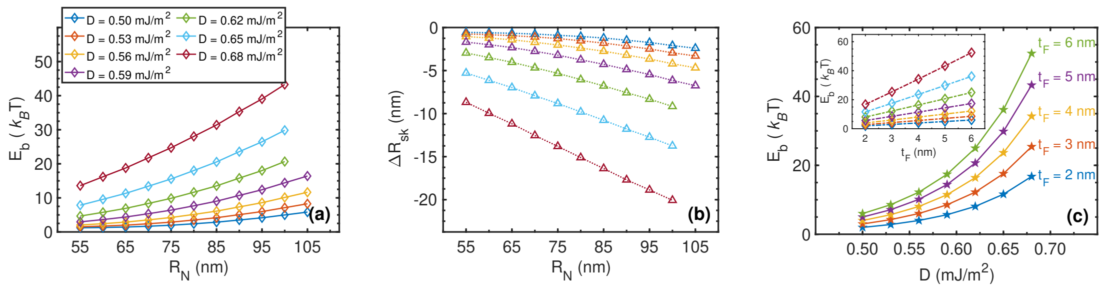

Figure 5.2: Material parameters dependence of the energy barrier, E_b. Effect of notch size (radius R_N) on (a) E_b, and (b) ΔR_{sk}, both for varying DMIs. We see that a larger R_N leads to a larger $|\Delta R_{sk}|$ that corresponds to a higher barrier. (c) Thickness dependence of E_b in a racetrack ($R_N = 100\ nm$). The inset shows that E_b increases linearly as a function of racetrack thickness, t_F for any specific D. The linear variation of E_b vs t_F is consistent with the overall uniform cylindrical shape of the skyrmion at ultrathin limit. The color code to represent DMI variations in (a), (b), and inset of (c) are the same.

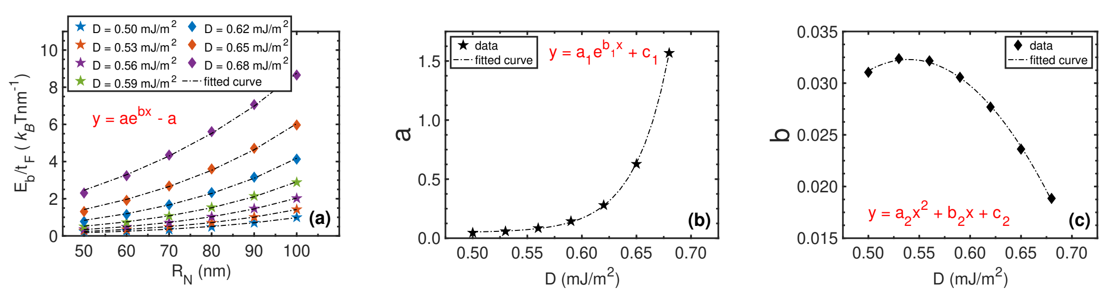

Figure 5.3: (a) Fitting of E_b (normalized by t_F) with respect to R_N. (b), (c) The relation between the fitting constants obtained from (a) and D. The red colored texts in each graph represent the fitting function.

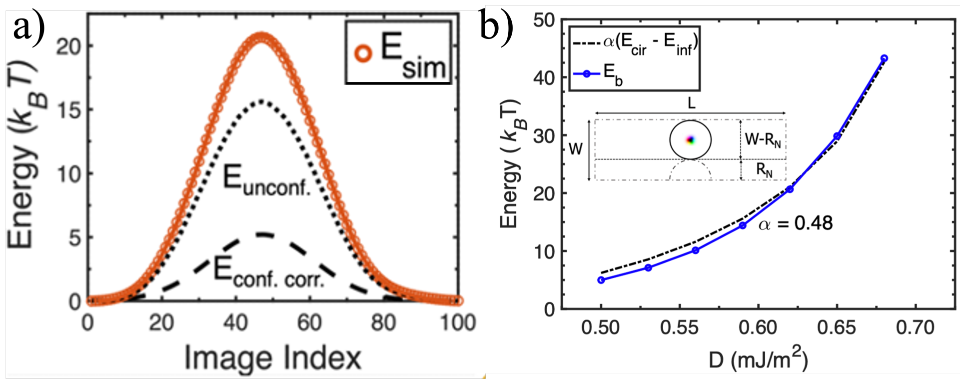

Figure 5.4: (a) Energy landscape of skyrmions in a racetrack ($R_N = 100\ nm$) from the MEP simulations (circles) and unconfined skyrmion energy E_{unconf}. $E_{conf.corr}$ is the energy correction due to the confinement.(b) Explanation of the mismatch between simulated and analytical (calculated using equation 5.3) data in a racetrack ($R_N = 100\ nm$). A skyrmion confined above the pinning site has the energy of a skyrmion confined in a circle of diameter $W - R_N$ above the notch minus that of an unconfined infinite plane skyrmion. Including only one fitting term can describe E_b with good accuracy for varying D values. The black circular region above the notch in the inset schematic represents the simulation geometry for the confined case.

thickness 5 nm (racetrack width is 200 nm). The zero for energy is defined as the energy of the first image index in the simulation which is relaxed to the left side of the notch (shown in Fig. 5.1(a) top). We vary the interfacial DMI, D from 0.50 mJ/m^2 to 0.68 mJ/m^2 and find energy barriers range from $\sim$ 5 to 45 k_BT. For the used exchange and anisotropy, the critical DMI, $D_c = 4\sqrt{A_{ex}K}/\pi = 0.71\ mJ/m^2$, which gives the ratio D/D_c from 0.70 to 0.96 where the effective anisotropy, $K = K_u - \frac{1}{2}\mu_0 M_s^2$ [126, 127]. As the skyrmion move past the notch, due to the confinement from its interactions with the notches and boundary it shrinks in size which results the energy barrier [15, 114].

Figure 5.1(c) shows a series of ΔR_{sk} corresponding to the energy plots shown in Fig. 5.1(b). As the D increases, for a specific exchange and anisotropy, the skyrmion size gets bigger, making it harder to squeeze through and generating a higher energy barrier. The positional lifetime of the skyrmion is described using an Arrhenius form

$\tau = f_0^{-1} e^{E_b/k_B T}$ where f_0 is the attempt frequency and E_b is the height of the energy profile (energy barrier). The f_0 term comes from the entropy effects which is not captured by the energy barrier. Approximately an E_b of 30 k_BT (35 k_BT) will provide positional lifetime in seconds (days) for $f_0 = 10^{10}$ Hz. 45 k_BT energy barrier will give a lifetime in years. Note that estimating the exact attempt frequency is still an open question and the value can be higher due to the entropy effect [128, 129, 130]. However, we use 10^{10} Hz because the most commonly accepted estimate for the attempt frequency is in the range of $10^9 - 10^{10}$ Hz for magnetic materials [131, 132, 133, 134].

We calculate the MEP for various notch sizes and demonstrate the impact on the energy barrier in Fig. 5.2(a) for $R_N = 55 - 105$ nm. We find that for all the DMIs, the energy barrier increases as R_N increases, by reducing the size of the skyrmion, consistent with Fig. 5.2(b). As R_N increases, the skyrmion size shrinks more, $|\Delta R_{sk}|$ gets larger, and the energy barrier increases proportionally. However, if we continue to increase R_N, at some point, the skyrmion starts annihilating as the region over the notch is insufficient to pass through and the skyrmion touches the notch boundary and the edge of the racetrack. For instance, from Fig. 5.2(a), we can see that throughout the range of the DMIs ($D = 0.50 - 0.68$ mJ/m^2), skyrmions pass through without annihilation up to $R_N = 100$ nm. For a larger notch, for example, $R_N = 105$ nm, the skyrmion gets annihilated when D is greater than 0.59 mJ/m^2.

We also vary the thickness t_F of the racetrack for several DMIs, and find an increase in energy barrier height for a thicker racetrack for a specific D. Figure 5.2(c) shows the thickness dependence of the energy barrier in a racetrack with $R_N =$ 100 nm. We get an energy barrier of $\sim$ 45 k_BT for a $\sim$ 45 nm skyrmion ($D =$ 0.68 mJ/m^2) in a moderately thick (5 nm) racetrack, which ensures years long lifetime that makes the device suitable for storage class memory applications. The inset shows the linearity of E_b as a function of t_F, which dictates that we can increase the energy barrier even further by increasing the thickness of the racetrack. Clearly, we can get a large enough energy barrier for smaller skyrmions as well in a thicker racetrack.

To quantify E_b, combining the data we get by varying the D, R_N, and t_F, we come up with a fitted empirical equation, normalized by t_F. Fig. 5.3(a) shows the simulated E_b vs R_N data are perfectly described by the fitted curves of the form $y = a(e^{bx} - 1)$. We find that a is an exponential function of D, while b is a quadratic function of D, as shown in Fig. 5.3(b) and 5.3(c) respectively. The final form of the equation is

$$E_b/t_F = a(e^{bR_N} - 1) \tag{5.1}$$

where a and b are related to D as follows

$$\begin{aligned} a &= a_1 e^{b_1 D} + c_1 \\ b &= a_2 D^2 + b_2 D + c_2 \end{aligned} \tag{5.2}$$

where the prefactor constants are material specific. For GdCo, $[a_1,\ b_1,\ c_1] = [6.874 \times 10^{-10},\ 31.64,\ 0.04783$, and $[a_2,\ b_2,\ c_2] = [-0.6922,\ 0.7471\ , -0.1693]$. The units of E_b, t_F, D, and R_N are in k_BT, nm, mJ/m^2, and nm respectively. It is worth mentioning that the form of the equation (5.1) is physically meaningful as it gives $E_b = 0$ when $R_N = 0$, which is expected. As energy of skyrmion increases linearly with t_F for the limit of uniform cylindrical shape of skyrmion (inset of Fig. 5.2(c)) at the limit of ultrathin films ($\lesssim 10\ nm$), the t_F is simply a scaling factor.

We compare our simulated data with the analytical equation derived for skyrmions [17, 1]. The different energy terms that give total energy equation of the skyrmions on an infinite plane are derived as [1, 17]

$$\begin{aligned} E_{\rm ex} &= (2\pi A_{ex} t_F)\left(\frac{2R_{sk}}{\Delta} + \frac{2\Delta}{R_{sk}} N_{sk}^2\right) f_{\rm ex}(\rho) \\ E_{\rm DMI} &= -\left(2\pi R_{sk} t_F\right) \pi D f_{\rm DMI}(\rho) \\ E_{\rm ani} &= \left(4\pi K_u t_F\right) R_{sk} \Delta f_{\rm ani}(\rho) \end{aligned} \tag{5.3}$$

where $\rho = R_{sk}/\Delta$. R_{sk}, Δ, N_{sk} are skyrmion radius, domain wall width, and skyrmion winding number respectively. The form factors, obtained by fitting numerical simulations is given by Eq. 2.16. Figure 5.4(a) shows that our simulated energy profiles (scattered circles) are perfectly matched with the analytical equation (solid curves) that includes the energetics of skyrmions within 2π model on an infinite plane $E_{unconf.} = E_{ex} + E_{DMI} + E_{ani}$, plus a phenomenological confinement correction $E_{conf.\ corr.}$ (see the dotted and dashed black curves in Fig. 5.4(a) for $E_{unconf.}$ and $E_{conf.\ corr.}$ respectively; adding up these two curves give the E_{tot}). As seen in Fig. 5.4(a), equation (5.3) alone fails to capture the simulated energy profiles because it assumes an unconfined planar geometry, while in our simulations, we use a confined geometry. As the confinement when the skyrmion is above the notch is somewhere in between an unconfined skyrmion and a completely confined skyrmion in a circular shape boundary, we expect the barrier to also be somewhere in between the two limits. To verify, we calculate the static energy of skyrmions both for a circle (E_{cir}) above the notch region with diameter $W - R_N$ (see the inset of Fig. 5.4(b)), and for an unconfined infinite plane (E_{inf}). In Fig. 5.4(b), we show the energy difference between E_{cir} and E_{inf} for a racetrack with $R_N = 100\ nm$. We find that our simulated E_b matches with $\alpha(E_{cir} - E_{inf})$ for the entire range of D, where α is a prefactor dependent on the racetrack geometry. We compare $\alpha(E_{cir} - E_{inf})$ and E_b for other notch radii and find overall agreement while α varies as a function of notch radius.

We explore alternate pinning mechanisms to compare the energy barrier among them. One common approach to introduce pinning sites is a local variation of the material parameters in a specific region in the racetrack [105, 83, 135, 136, 137]. In practical systems, the variation of material parameters can be achieved by naturally occurring and intentional defects, grain boundaries, composition and thickness gradient in the thin films, voltage gating, modulating the heavy metal layer, etc. We create the pinning sites by locally varying K_u, A_{ex}, D, and M_s. We vary one parameter at a time while the other parameters remain constant throughout the racetrack. Figure 5.5(a) shows the energy barrier for different pinning sites, including the fully notched geometry for a 5 nm thick racetrack having a semi-circular pining site of 100 nm radius. It appears that a racetrack with a fully notched geometry produces the highest energy barrier compared to the rest, which attributes to the largest change in skyrmion radius while passing over the notch as shown in Fig. 5.5(b). Additionally, notches are easier to create experimentally than controlling local variations of material parameters.

We also calculate E_b for another promising material Mn_4N for skyrmion-based spintronics applications [138, 139, 140]. In a 5 nm thick Mn_4N racetrack ($R_N = 75\ nm$), we find an E_b of $\sim 45\ k_BT$ for a $\sim 40\ nm$ skyrmion, while for GdCo with identical R_N, t_F, and R_{sk}, the E_b is $\sim 22\ k_BT$. The used parameters for Mn_4N are $A_{ex} = 15\ pJ/m$, $K_u = 110\ kJ/m^3$, $M_s = 105\ kA/m$ [138]. Our finding suggests that Mn_4N offers a higher E_b than GdCo, which is mainly because of the higher exchange stiffness of Mn_4N. Needless to say that the E_b can be further increased by tuning the R_N and t_F of the racetrack.

We have focused on semi-circular notches so far, however, the shape of the notch is important for the dynamics of the skyrmions, including their nucleation and annihilation [110, 109, 112, 111]. As a case study, we show the energy barrier associated

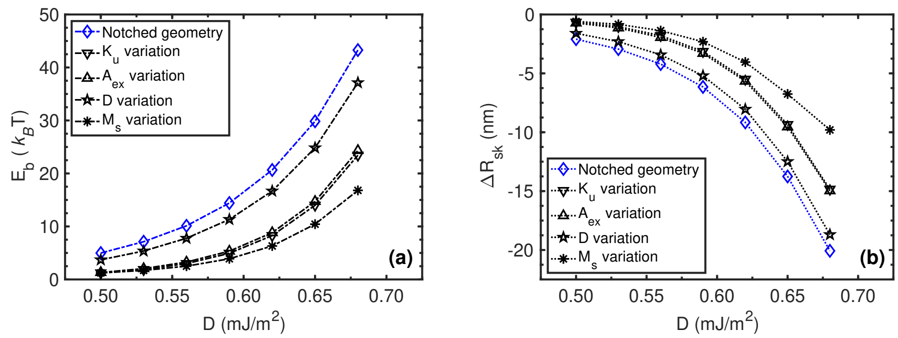

Figure 5.5: (a) Energy barrier for different pinning sites in a 5 nm thick racetrack. For all the cases, the pinning site is a semi-circular region of 100 nm radius. K_u and A_{ex} of the pinning site are 2 times higher, and D and M_s are 10 times lower than the rest of the track region. We choose the ratio that gives the highest E_b. (b) Change in skyrmion radius corresponding to the E_b in (a), shows a proportional relation between E_b and $|\Delta R_{sk}|$.

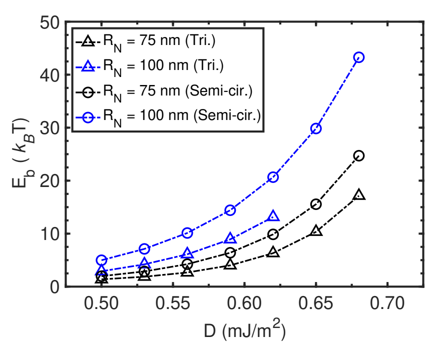

Figure 5.6: Energy barrier of a triangular notch with 75 nm (black) and 100 nm (blue) depth in comparison with semi-circular notch.

with a triangular notch with 75 nm and 100 nm depth in comparison with the semi-circular notch of the same radii in Fig. 5.6 for a 5 nm thick racetrack. We see that for the same skyrmion size, a triangular notch produces a lower E_b than the semi-circular one. Moreover, annihilation occurs for smaller skyrmion size in the case of a triangular notch. For instance, for 100 nm notch depth, skyrmion gets annihilated when D is greater than 0.62 mJ/m^2 as shown in Fig. 5.6. These findings show that a semi-circular notch is more favorable to achieving a high energy barrier. Nonetheless, one important thing to note is that the trend of the energy barrier is qualitatively similar irrespective of the notch shape. Therefore, our derived quasi-analytical equations hold for other notch shapes as well with different prefactor constants. Similarly, our explanation of simulated E_b in terms of $\alpha(E_{cir} - E_{inf})$ also works for triangular shaped notch for a different fitting parameter α. For a 5 nm thick racetrack with 75 nm notch, $\alpha = 0.37$ for semi-circular shape while for triangular shape $\alpha = 0.25$. This shows that by using the quasi analytical form $\alpha(E_{cir} - E_{inf})$ we can predict the energy barrier needing only one fitting term α.

While a barrier is needed to hold the skyrmion in place, it is equally important to ensure that the critical current to unpin the skyrmions is not too large, as that would cause unacceptable energy dissipation when integrated with the peripheral circuitry, not to mention random skyrmion annihilation, and the occasional unintended nucleation [141]. The energy barrier can be tuned by varying various knobs such as materials parameters and notch geometries. However, we need to optimize it to get a high enough hold time for the skyrmions yet require a moderate unpinning current.

Figure 5.7 shows the unpinning current of racetracks with 95 nm and 100 nm notch radii, and 5 nm thickness. The current density distribution for the racetrack with the notch is calculated using COMSOL Multiphysics® [142]. We employ spin

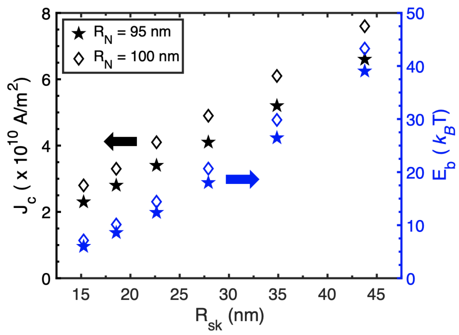

Figure 5.7: The critical current J_c (black) to unpin the skyrmion and the corresponding E_b (blue) for a 5 nm thick racetrack as a function of R_{sk}. We see a low unpinning current with a fairly large energy barrier. The arrows point each colored data to the corresponding y-axis.

orbit torque (SOT) with a spin Hall ratio $\theta_{SH} = 0.15$ while estimating the unpinning current. We use current pulses ranging from 8 ns to 25 ns to unpin the skyrmions. We find that bigger skyrmions need a shorter pulse and the critical current increases as E_b increases. The energy barrier increases faster with radius than the critical current, which would help us to get a large enough barrier and a small enough unpinning current. We find moderate critical currents for large energy barriers. For instance, a ~ 45 nm skyrmion can be unpinned with currents of 6.6×10^{10} A/m^2 and 7.6×10^{10} A/m^2 while the corresponding energy barriers are ~ 40 k_BT and ~ 45 k_BT respectively, which are orders of magnitude smaller than the critical current required to unpin domain walls [143, 139]. Moreover, the obtained critical currents are significantly lower than the nucleation current ($> 10^{12}$ A/m^2) of the skyrmions in a constricted geometry [110, 141], which prevents any unintended nucleation of skyrmions during the unpinning process.

5.5 Summary

In this chapter, we demonstrated that skyrmion positional stability is achievable by creating notches along a racetrack. We presented quantitative analyses, backed by analytical equations for various material parameters, notch geometries, and racetrack thicknesses. An optimal combination of skyrmion size, notch radius, and thickness of the racetrack provides a large enough energy barrier ($\sim 45\ k_BT$) to achieve a positional lifetime of years for long-term memory applications. We showed that the quasi-analytical description can describe the simulation results with only one fitting term. We found a moderately low minimum critical current to unpin the skyrmion ($\sim 10^{10}\ A/m^2$), which is an essential aspect of low-power operations.

Chapter 6

Tuning of Three dimensional Topological Insulators

As we saw in previous chapters, the generation of spin currents is crucial for any spintronics applications. Methods of generating spin current can be categorized into two approaches:

1. Passing an electrical current through a ferromagnet, where the ferromagnet would then polarize the electrons. One of the main drawbacks of this method is its low efficiency due to the high resistance of the ferromagnet and relatively low polarization efficiency.

2. Using a nonmagnetic material that can convert the electric current to a spin current. These types of materials are known as spin-momentum locked materials. Two major groups of spin momentum locked materials are heavy metals which we focused on in the previous chapters, and three dimensional topological insulators (3DTI). In this chapter, we focus on 3DTIs and ways of tuning their spin current. Both heavy metals and 3DTIs rely on spin orbit coupling to generate spin current. The dominant mechanism for the generation of spin current in heavy metals is the spin

Hall effect which happens in the bulk of the heavy metal from 3DTIs are nonmagnetic, which are insulators in the bulk and metallic at their surface. The surface state of the 3DTI is the interface between the bulk insulator of the 3DTI and a trivial insulator such as a vacuum. Similar to the heavy metals, a 3DTI also has a strong SOC. The SOC has to be strong enough to cause band inversion. This chpater is reproduced from Ref [144] co-authored with Yunkun Xie, Samiran Ganguly, Avik W Ghosh and Ref [145] co-authored with Samiran Ganguly, George J de Coster, Mahesh R Neupane, and Avik W Ghosh.

6.1 Reciprocal Ferromagnet and 3D Topological Insulator Interaction

The surface state of a 3D topological insulator (3DTI) is a spin-momentum locked conductive state, whose large spin hall angle can be used for the energy-efficient spin orbit torque based switching of an overlying ferromagnet (FM). Conversely, the gated switching of the magnetization of a separate FM in or out of the TI surface plane, can turn on and off the TI surface current. The gate tunability of the TI Dirac cone gap helps reduce its sub-threshold swing. By exploiting this reciprocal behaviour, we can use two FM/3DTI heterostructures to design a 1-Transistor 1-magnetic tunnel junction random access memory unit (1T1MTJ RAM) for an ultra low power Processing-in-Memory (PiM) architecture. We combine the Fokker-Planck equation with the Non-equilibrium Green Function (NEGF) based flow of conduction electrons and Landau-Lifshitz-Gilbert (LLG) based dynamics of magnetization. Our combined approach allows us to connect device performance metrics with underlying material parameters, which can guide proposed experimental and fabrication efforts.

In-memory computing or Processing-in-Memory (PiM) [146, 147] is an important emerging architectural design that reduces data movement between the memory and the processor. PiM operates by performing simple intermediate steps along a long chain of compute processes within the memory array itself, as far as possible. The memory layout in a typical PiM architecture is in the form of a grid. Each row and column of the grid is driven by selectors, which enable the cells for a read or write operation. A sense amplifier reads an entire row of the memory cell by comparing its state against a known reference voltage, current, or charge [148]. While such a local computing paradigm leads to a significantly reduced footprint, this however, needs to be traded off against material integration complexity as well as overall switching costs.

Recent experiments on spin-orbit torque (SOT) based switching [149, 150, 151, 152] in FM/3DTI heterostructures have shown TIs to be a promising alternative to heavy metal (HM) underlayers, because of their higher spin Hall angle. Conversely, the ability of a FM to turn current ON or OFF in a TI by breaking inversion symmetry through its orientation [153, 154] offers an option for a gate tunable selector, along with the intrinsic energy efficiency of a gate-tunable bandgap [155]. This brings up intriguing possibilities of using the reciprocal interactions between a FM and a TI to realize unique, energy-efficient device configurations.

Here we present a potentially energy efficient efficient 1-Transistor 1-magnetic tunnel junction random access memory unit (1T1MTJ-RAM), that can function as the building block of a PiM design (Fig. 6.1). In the device we are discussing here, there are two FM/3DTI heterostructures, one functioning as a transistor switch/row-column selector, and the other as a nonvolatile memory unit. The switching in the second, MTJ memory unit (FM2) is based on conventional spin orbit torque (SOT) [149, 151, 150], with the required spin current at the FM2-3DTI interface provided by the spin momentum locking at the 3DTI surface. The FM that acts as the transistor

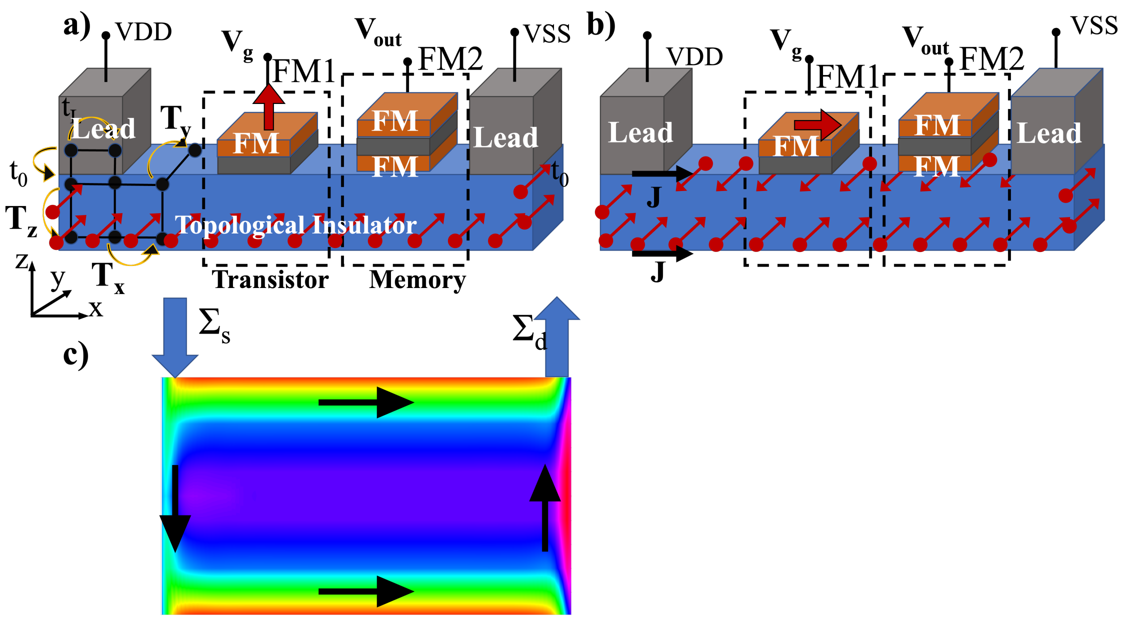

Figure 6.1: a) Schematic 1T1MTJ cell using FM/3DTI heterostructure in the off state, where a ferromagnet FM1 oriented perpendicular to the TI plane opens a gap in its top surface states. The source and drain are placed on top of the channel region in contact with the top layer. b) In the ON state of the device, the current flow at the top surface is restored upon rotating the magnetization FM1 into the TI plane, whereupon the TI top surface bandstructure is no longer gapped. c) Simulated current flows on both top and bottom layers, connected by current flowing along the ungapped side walls. The first ferromagnet (FM1) is the selector unit while the second (FM2) is the memory unit.

unit (FM1) is the trickier component, as it needs to be electrically switched from out of plane to in plane and back. There are a number of mechanisms to achieve this transistor like behaviour. One way is to use a gated piezoelectric clamped above a magnetostrictive material sitting on the TI [156, 157, 158, 159, 160, 161]. Another mechanism is interface induced anisotropy of a FM/3DTI and an applied electric field to control the polarization of the FM1 [162, 163]. The latter approach benefits from intrinsic properties of the FM/3DTI heterostructure and the effect of Voltage Controlled Magnetic Anisotropy (VCMA) [164].

One of the known challenges for the FM1-3DTI is an expected low On/Off ratio compared to competing technologies such as CMOS. We show that as a selector for low power PiM, the On/Off ratio does not need to be very high. In fact, our proposed device is naturally suited for compact PiM designs, since it directly incorporates a selection transistor in the first FM1-3DTI combination. Using an enhanced sense-amplifier for each column with programmable sensing thresholds, it is possible to implement basic Boolean operations (AND, OR, XOR, Majority, and their complements). We describe a possible scheme of building such a PiM towards the end of this section.

Computational approach. We set up a tight binding Hamiltonian that describes the 3DTI, the Zeeman energy term H_Z originating from the FM/3DTI exchange and the on-site energy term H_V from the applied gate voltage at FM1, with parameters fitted to *ab-initio* calculations. In the 3D atomistic grid $\{i, j, k\}$, this looks like [165, 166, 167, 168]

$$\begin{aligned}
H &= H_{3DTI} + H_Z + H_V \qquad (6.1)\\
H_{3DTI} &= \sum_{ijk} c^\dagger_{i,j,k}\varepsilon_{3DTI}c_{i,j,k} + \Big(c^\dagger_{i,j,k}T_x c_{i+1,j,k} + \\
&\quad c^\dagger_{i,j,k}T_y c_{i,j+1,k} + c^\dagger_{i,j,k}T_z c_{i,j,k+1} + h.c.\Big)\\
H_Z &= \sum_{ijk} c^\dagger_{i,j,k}M_0\mathbf{S}.\sigma c_{i,j,k}\\
H_V &= \sum_{ijk} c^\dagger_{i,j,k}V_g(x_i, z_k)c_{i,j,k}
\end{aligned}$$

where the onsite energies $\varepsilon_{3DTI} = (C_0 + 2C_1 + 4C_2)I_{4\times4} + (M + 2M_1 + 4M_2)I_{2\times2} \otimes \tau_z$, while the various hopping terms $T_{x,y} = -M_2 I_{2\times2} \otimes \tau_z - C_2 I_{4\times4} + (iA_0/2)\sigma_{x,y} \otimes \tau_x$, $T_z = -M_1 I_{2\times2} \otimes \tau_z + C_1 I_{4\times4} + (iB_0/2)\sigma_z \otimes \tau_x$. For Bi_2Se_3, the parameters used are $M = -0.28$ eV, $A_0 = 0.8$ eV, $B_0 = 0.32$ eV, $C_1 = 0.024$ eV, $C_2 = 1.77$ eV, $M_1 = 0.216$ eV, $M_2 = 2.6$ eV, $C_0 = -0.0083$ eV. τ and σ are the Pauli matrices in orbital and spin subspaces respectively while I is the identity matrix. One layer each of the source and drain is included in the Hamiltonian. The fixed FM in the MTJ is not included in the simulation. V_g is the applied gate voltage to the 3DTI varying with thickness.

The employment of a 3D model allows us to separate the bulk and interfacial components of the charge and current distribution. The placements of magnets and the source and drain contacts are shown in Fig. 6.1. The current source, drain, the FM1 and FM2 are all connected to the top surface.

We employ the Non-Equilibrium Green's Function (NEGF) formalism to analyse the transport signatures and the overall performance of the device. The retarded Green's function G^r and correlation (i.e., non-equilibrium) Green's function G^n of the electron can be written as [169, 170]

$$\begin{aligned}
G^r(E, \mathbf{k}_\perp) &= [EI - H(\mathbf{k}_\perp) - \Sigma_S(E, \mathbf{k}_\perp) - \Sigma_D(E, \mathbf{k}_\perp)]^{-1} \\
G^n(E, \mathbf{k}_\perp) &= G^r \left(f_S \Gamma_S + f_D \Gamma_D\right) G^{r\dagger} \\
\Gamma_{S,D} &= i\left(\Sigma_{S,D} - \Sigma^\dagger_{S,D}\right)
\end{aligned} \tag{6.2}$$

with $f_{S,D}$ the bias separated Fermi-Dirac distribution functions on the source/drain sides. We assumed an infinite cross-section that allowed us to Fourier transform the transverse y-z hopping terms into $\vec{k}_\perp$. The self-energies $\Sigma_{S,D}$ describe the projection of the contact states onto the channel, and are calculated recursively at each energy and transverse momentum value. $\Gamma_{S,D}$ are the corresponding energy broadening matrices denoting escape rates into the contacts. The charge and spin currents from site i to

j are then calculated as

$$\mathbf{J}_s^{i\to j} = \frac{q}{ih}\sum_{\mathbf{k}_\perp,E} \mathrm{Tr}\left[\boldsymbol{\sigma}\left(H_{ij}G^n_{ji} - G^n_{ji}H_{ij}\right)\right] \tag{6.3a}$$

$$J_q^{i\to j} = \frac{q}{ih}\sum_{\mathbf{k}_\perp,E} \mathrm{Tr}\left[\left(H_{ij}G^n_{ji} - G^n_{ji}H_{ij}\right)\right] \tag{6.3b}$$

The SOT torque is given by $\tau_{SOT} = \mathbf{m}\times(\mathbf{J_p}\times\mathbf{m}) - \alpha\,\mathbf{m}\times\mathbf{J_p}$, where α is the Gilbert damping and $\mathbf{m}$ is the magnetization vector of the ferromagnet. The polarization current $\mathbf{J_p}$ comes from the NEGF calculated spin current $\mathbf{J_s}$ in the TI, as well as phenomenological scattering terms in the magnet. We can keep track of the separate in and out of plane vector components of the polarization current as a complex vector, $\mathbf{J_p} = \mathbf{J}_{in} + i\mathbf{J}_{out}$, where [171, 172, 173]:

$$\mathbf{J}_p = \frac{p\mathbf{J_s}L^2}{t_{FM}}\left(\frac{1}{\lambda_\phi^2} - \frac{i}{\lambda_j^2}\right)\frac{\sinh t_{FM}/L}{\cosh t_{FM}/L} \tag{6.4a}$$

$$\tau_{SOT} = \mathbf{m}\times(\mathbf{J_p}\times\mathbf{m}) - \alpha\,\mathbf{m}\times\mathbf{J_p} \tag{6.4b}$$

where the net scattering length $L = (1/\lambda_{sr}^2 + 1/\lambda_\phi^2 - i/\lambda_j^2)^{-1/2}$. $\lambda_{sr}, \lambda_\phi, \lambda_j$ are spin relaxation, precessional and decoherence length of the ferromagnet of thickness t. J_s is the spin current density at the interface of FM2 and TI calculated from Eq. 6.3b, and p is the efficiency of spin current transfer from TI to FM2 (taken to be 0.5 here), which depends on the interfacial exchange. Note that due to the spin current precessing in the ferromagnet, an out of plane component arises in the torque, denoted by the imaginary part of τ_{SOT}.

The dynamics of the two magnets are simulated using the Landau-Lifshitz-Gilbert (LLG) equation[174]. By changing the anisotropy we can switch FM1 from out of plane to in plane (using VCMA or strain), which changes the Zeeman Hamiltonian H_Z. The corresponding NEGF calculated torque τ_{SOT} with phenomenological corrections (Eqs. 6.3b,6.4b) is then fed into the LLG equation self-consistently. Assuming the electron transit speed is orders of magnitude faster than the magnet's characteristic FMR frequency, we can stick to steady state NEGF, and adjust the torque quasi-statically as the magnetization $\mathbf{m}$ evolves. The quasi-static approximation reduces computational complexity significantly without compromising on accuracy. The bandstructure of the 3DTI at the location of the FM1 is modified due to the interfacial effects and the applied voltage, which shift its location with respect to the Fermi energy (Fig. 6.2). The shift of bandstructure is not uniform throughout the thickness; we shift the bottom surface 0.5 times the top surface under the applied gate voltage V_g, and assume the magnet covers the full TI width laterally.

To solve the LLG equation we have taken a macro spin model with effective anisotropy field $\mathbf{H}_K = (2\Delta k_B T/M_s V)(\mathbf{u_0}.\mathbf{m})\mathbf{u_0}$, where Δ is the ferromagnet's thermal stability, related to anisotropy K as $\Delta = KV/k_B T$. $\mathbf{u}_0$ is the effective field, pointing along $\hat{z}$ and $\hat{y}$ directions for FM1 and FM2 respectively at the start of the simulation. For room temperature simulations we have added a stochastic effective field described as $\mathbf{H}_{Th} = (\eta/\mu_0)\sqrt{2\alpha k_B T/M_s \gamma V \Delta t}$ [175], where η is a random vector following a normal distribution with zero average. μ_0 is vacuum permeability, α is damping, k_B is Boltzmann constant, T is temperature, M_s is saturation magnetization, γ is the electron gyromagnetic ratio. V and Δt are volume of FM2 and simulation time step. Finally, the solved LLG equation can be written as: $(1+\alpha^2)\partial_t \mathbf{m} = \gamma\left(\mathbf{m}\times\mathbf{H} + \alpha\mathbf{m}\times(\mathbf{m}\times\mathbf{H}) + \tau_{SOT}\right)$, with $\mathbf{H} = \mathbf{H}_K + \mathbf{H}_{Th} + \mathbf{H}_D$ where $\mathbf{H}_D$ is the demagnetization field.

The voltage control of the FM1 anisotropy can come from a VCMA effect across an oxide-FM stack, with coefficient ξ and oxide thickness t_{ox}. Here $\Delta K_u = \xi V/t_{ox} t_{FM}$ due to the electric field from the vertical voltage difference across the stack and the interfacially induced anisotropy. Alternatively, if we use strain as a switching mechanism for FM1, the applied effective field can be added to $\mathbf{H}$ as $\zeta(\mathbf{u}.\mathbf{m})\mathbf{u}$[161] where ζ is the strain coefficient that needs to cancel out the effective anisotropy field $\mathbf{H_K}$. u is the strain direction which needs to be along z (perpendicular to the TI) in this case. A third mechanism for controlling the anisotropy is by varying the free energy[162] through an applied gate voltage. This method works by making the perpendicular FM1 with gapped 3DTI the favorable state compared to in-plane FM1 and gapless 3DTI. For the VCMA mechanism, assuming a thickness of 1 nm for the capped oxide and FM1 layers, a $\Delta K_u/V = 100KJ/m^3$ for CoFeB of 1 nm thickness has been reported [53, 54], whereas by doping FM/oxide interface larger $\Delta K_u/V$ has been achieved as well[55, 56]. For the straining mechanism, $\Delta K_u/V$ of 200-300 KJ/m^3 have been reported [161]. For both the VCMA and strain mechanism, the free energy change from the applied gate V_g can potentially lower the voltage requirements. The required voltage to change the anisotropy of a reliable FM1 with $\Delta = 40$ of size $40 \times 40 \times 1$ nm^3 would be 0.3-1 V. Although this would be relatively large compared to the applied bias because there would be negligible current flowing in the FM1 heterostructure, the energy consumption would still be small (in the range of 100 aJ [161]).

Results: In Fig. 6.2 we look at the bandstructure of the 3DTI channel under four circumstances. Fig 6.2a and b show the bandstructure of the channel at the location of the FM1, for the On (magnet in plane of TI) and Off (magnet out of plane) states respectively, while Fig. 6.2c shows the pristine (magnet-free) TI states for comparison. For the On state, we see a small modification of band-structure in (a). Specifically, the Dirac point is shifted away from the Γ point. For the Off state (b) however, the degeneracy is lifted and a corresponding energy gap is created for the states arising from the top surface (solid lines), while at the same time keeping the bottom surface states (dashed lines) intact. We also present the side surface states (Fig.2. d) and as

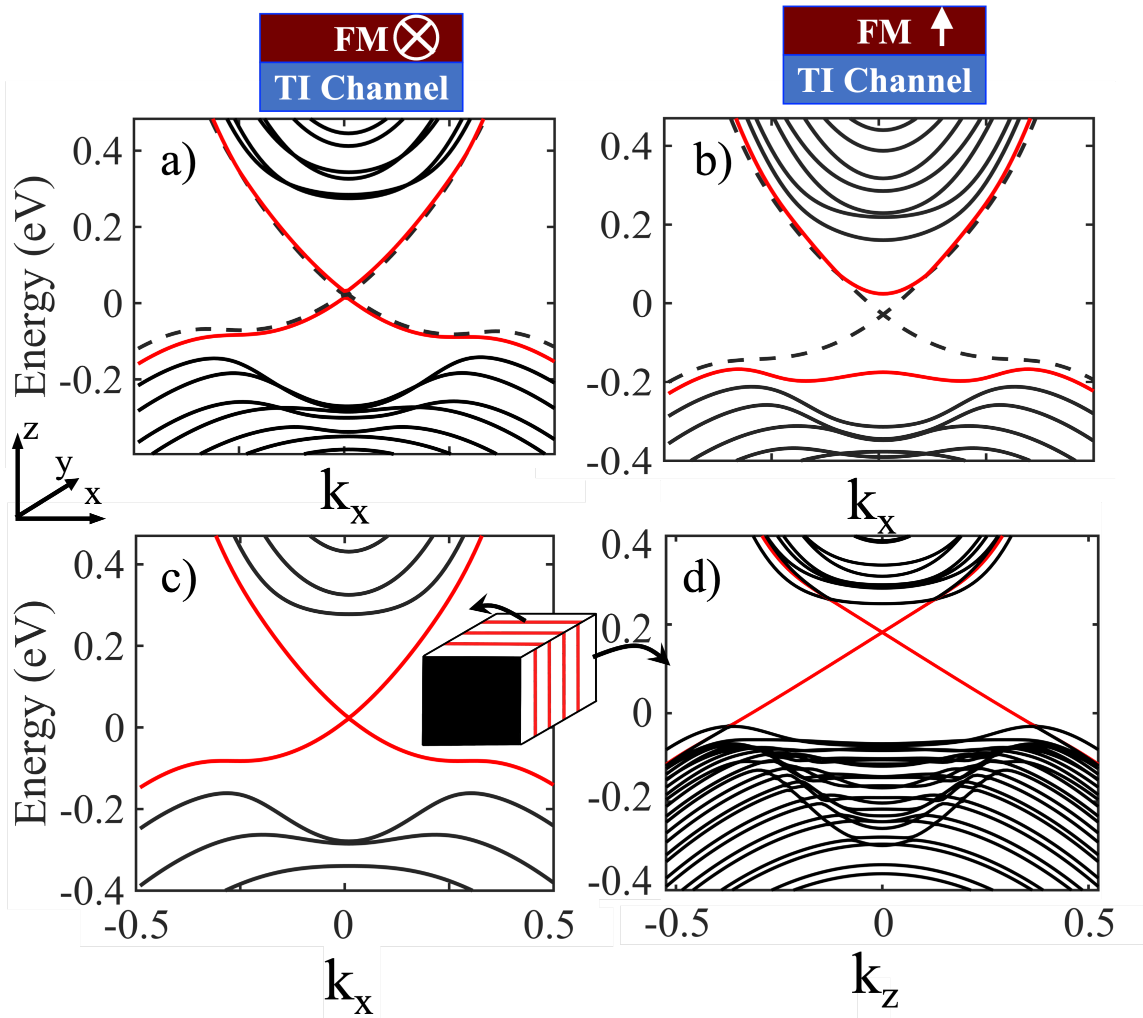

Figure 6.2: The band structure of the device channel at various points. Red lines in (a-c) emphasize the top surface states and in d, the side surfaces. Dashed lines show the bottom surface states a) FM/3DTI bandstructure with in plane magnet (in y direction) b) Magnet in z direction with on site voltage energy at the top at -0.1 and bottom at -0.05 V. c) Bandstructure of the pristine (magnet free) 3DTI channel discretized in the z direction (top to bottom) d) Bandstructure of the 3DTI channel discretized in the transport direction (side to side).

expected (Fig. 6.1.b) the sides of the 3DTI stay gapless for both On and Off states, as the FM only affects part of the top surface. This would mean that for an electrical transistor based on FM/3DTI [162], the current along the 3DTI sides would play a crucial role. However in the device geometry we propose here, we avoid the problem of dealing with the side current as only the top surface states can apply any appreciable spin orbit torque to FM2.

For a competitive transistor-memory device based on the FM/3DTI stack, we outline requirements. The first is the On/Off ratio β. For deterministic switching of an in-plane ferromagnet with a given thermal barrier Δ, the critical spin current is estimated as $I_s = (4q\alpha k_B T\Delta/\hbar)(1 + H_D^*/2H_K)$ [176]. We also need to make sure that when FM1 is out-of-plane in the Off state, the surface leakage current would be small enough to not accidentally switch FM2. The probability of switching P can be approximated from a Fokker-Planck analysis with a perpendicular magnet [177, 178]

$$\begin{aligned} P &\approx 1 - \Delta_T \frac{\iota}{\iota + 1} e^{-2\iota\tau}, \\ \tau &\equiv \frac{\alpha\gamma\mu_0 H_K}{1 + \alpha^2} t \end{aligned} \tag{6.5}$$

When the TI is not gapped (FM1 in plane, $P \approx 1$), the write error is $WER \approx 1 - P$, while when the TI is locally gapped (FM1 out of plane, $P \approx 0$), the error is $WER \approx P$. For simplicity we take the WER in both cases to be equal to each other. In the case of thermally assisted switching (Off) we would need to either solve the Fokker Planck equation or use the empirical equation $P = \exp\left(-tf_0 \exp\left(-\Delta(-\iota)^c\right)\right)$. where t is the switching time, and $\iota = I/I_s - 1$ is the fractional current overdrive. c is an empirical constant between 1 and 2, where 1 is for in-plane and 2 is for out-of-plane FM2, and in between for imperfect materials.

The ability to open a gap is determined by the Zeeman term $H_z = M_0\mathbf{S}.\sigma$ which

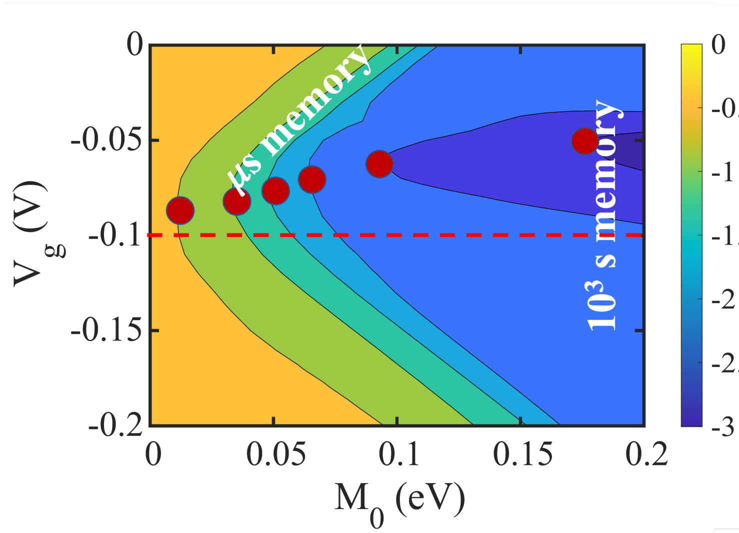

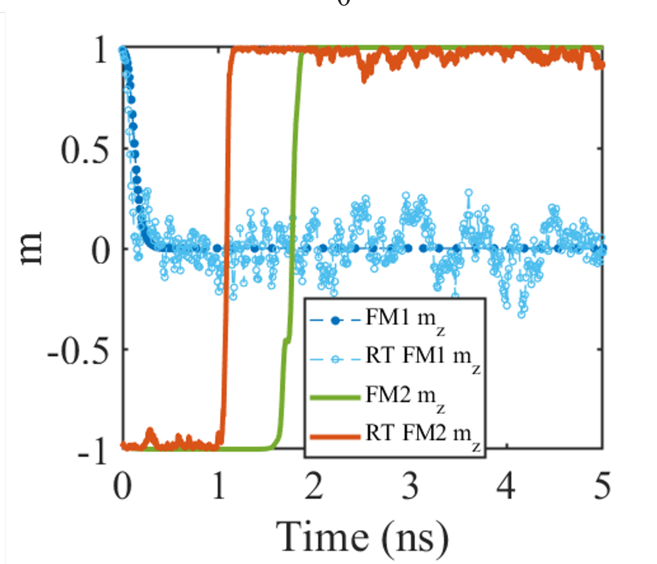

Figure 6.3: The colorplot shows the logarithm of the On/Off ratio β of non-equilibrium spin current J_s at the FM2/3DTI interface with respect to the Zeeman energy coefficient M_0 and applied gate bias V_g. The contours show different memory regimes in which the device can operate, ranging from cache memory (operating in μs up to longer term memory, like a computer RAM 10^3 s). The dashed red line is the V_g equal to the applied bias $VDD = -0.1V$. As explained in the text, the red circles show the minimum required M_0 for each contour. Bottom figure shows the 0 K and 300 K simulation of the FM2 magnetization dynamics. Applied voltage bias and V_g are 100 mV. The Zeeman exchange energy for FM2 is taken to be 10 meV. $\lambda_{sr}, \lambda_{\phi}, \lambda_j$ are taken to be 1, 10, 1 nm respectively. Source, drain, FM1 and FM2 lengths are 20 nm each. 3DTI thickness is 5 nm (6 layers) and magnet thickness t is 2 nm. The total length of the channel is 140 nm. Gilbert damping α is 0.1.

breaks the time reversal symmetry. This term needs to be large enough to have a small error rate for accidental switching. Equation 6.6 allows the material parameters to be directly connected to the device performance metrics. For long term storage, we assume $\Delta = 40$, write error rate $WER = 10^{-7}, c = 1.2$ [179, 180] and attempt frequency $f_0 = 1\ GHz$ [181]. For the Off state, depending on the required memory application (e.g. cache memory or long term memory) t would be different, ranging from $\sim \mu s$ to years. We can see from Fig. 3.a that depending on the values of V_g and M_0, the device can be used in different regimes. When the FM1 is in plane, the required I/I_s is 1.7. When FM1 is out plane, the flowing current needs to be small enough to not accidentally switch FM2. For short term memory, this requires I/I_s to be < 0.2. This means that a modest On/Off ratio of 10 would make the device work. For longer memory applications (hours to days), a larger On/Off ratio (Fig. 6.3a), $\log_{10} \beta > 3$ is needed.

From Figs. 6.2c and d we can see there is a band offset between the side and top surface TI bandstructures. This would mean that the conductivity of side and top surfaces differ at any given energy. To achieve minimum required magnetic exchange M_0, the applied gate voltage should be approximately same as the applied voltage bias (-0.1 V). This matches the observation from Fig. 6.3a, where the minimum M_0 required for short term ($\sim \mu$s) memory happens when the V_g is near the VSS (red dashed line). This implies that without a magnetization, when the chemical potential is tuned to the top or side Dirac point to reduce its conductivity, the other surface will retain a large density of states (DOS), providing a shunting conduction channel. For long term (10^3 s) memory, a higher On/Off ratio is needed which requires a bigger bandgap, hence a larger M_0 value. Due to the sizable gap opening for long term memory, the critical V_g for the minimum required M_0 deviates from the midpoint.

Note that the required On/Off ratio would be larger if we used a simplified 2D

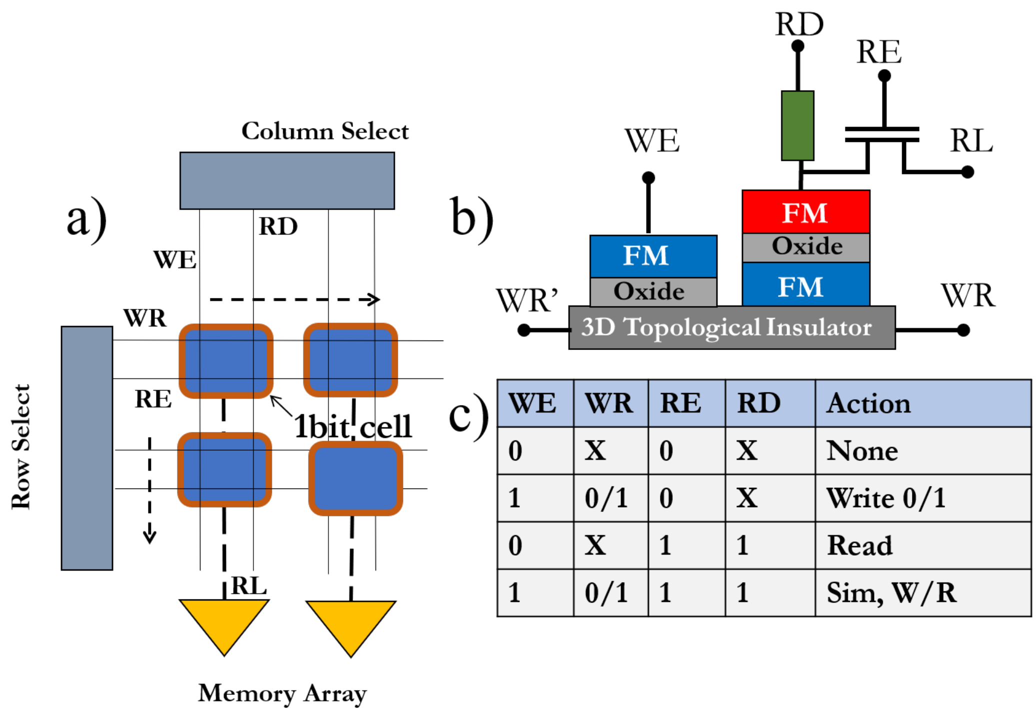

WE	WR	RE	RD	Action
0	X	0	X	None
1	0/1	0	X	Write 0/1
0	X	1	1	Read
1	0/1	1	1	Sim, W/R

Figure 6.4: a. Memory array for the presented cell b. The cell and its position in the array indicated. c. The truth table for the array operations.

Hamiltonian that only considers the surface states. This is because in a realistic TI structure, a significant amount of the current shunts into the bulk of the TI stack [175], which our 3D geometry naturally takes into account (current shunting seen in Fig. 6.1c - we simulate a depth of 6 layers here). To have a faster working memory, using a perpendicular ferromagnet as FM2 is preferred, as the switching mechanism would be determined by a field like torque which is faster than an anti-damping torque. However, for a perpendicular ferromagnet an assisting external field is required. This assisting field can originate from the stray field of a capping magnetic layer or the exchange bias of a coupled antiferromagnet-ferromagnet stack [182, 183, 184].

Proposal for a Processor-in-Memory (PiM) design. In Fig. 6.4a. we show a possible approach for performing in-memory compute functions using an array built out of the presented memory cell. The relation between the voltage lines in Fig. 6.4

and 6.1 are as follows: WR : VDD, WR' : VSS, WE : Vg, RL : V_{out}. The cell (Fig. 6.4b) contains a selection transistor, which acts as a write enable, i.e. WE signal. The current flowing in the TI acts as the write signal, with the two ends being designated as WR and WR'. Since a spintronic memory cell requires bipolar currents for programming, we can either use a bipolar current generating selector to drive the WR signal with WR' grounded, or else reverse the polarities of WR, WR' pairs between 0/1 and 1/0 respectively.

The read is performed through a voltage divider arrangement at the reader MTJ, which changes the output voltage at the read line (RL) that is shared over the cells in the array column-wise. This reader is charged through the RD line, and we include one transistor in the cell for a read enable functionality (RE) that also provides the load resistance which attaches a meaningful current quantity to the read line per cell depending on the voltage at the divider; critical for the read and PiM functionalities as we describe next. We choose to arrange the read to be done row-wise, whereas the write is done column-wise. This is by no means a necessary condition for designing this architecture, but simply one of the choices we make that allows us the option of simultaneous read and write options, if it is ever necessary. The read process is performed by sensing the current in the read line and compared with a reference current in the sense amplifier (SA), which then reports the value stored at a specific cell addressed via RD and RE signals. The truth table of these operations is shown in Fig. 6.4c.

The processing-in-memory functions are also arranged within the SA over each column. We can build in reference currents that enable Boolean operations over the whole array by enabling multiple rows at the same time. Consider a two-bit AND operation over any two rows. In this case, the two specific rows are enabled using RE and all the RD over the rows are enabled as well. Each of the SA reference currents for the AND operation is set to $1.8I_R$ where I_R is the read current of a cell when it is storing '1'. In this case both of the cells being read simultaneously by a single SA will have to be '1' to trigger the SA to report '1', in all other combinations it will report '0'. Similarly for the OR case, the reference current can be set as $0.8I_R$ to trigger '1' from SA for even one of the cells being '1'. An XOR gate can be implemented by a two threshold SA where the thresholds are $0.8I_R$ and $1.8I_R$ and it is configured to report '1' when reading values in between these two references. The complement functions are easily implemented by using an additional inverter. All these functionalities are built within a single SA and as per the requirements of the computation the SA can be configured to perform a given operation.

6.2 Gating Topological Insulators

The spin-momentum locking feature of topological surface state (TSS) imposes spin conservation rules across a PN junction, suggesting a charge-to-spin conversion ratio (scaled dimensionally like the Spin Hall Angle except between longitudinal current densities) can exceed unity and be as high as 20 [185]. This number is much higher than the Spin Hall Angle measured in heavy metals such as Pt (0.07)[186], β-Ta $(0.12 - 0.15)$[187], and in Pt-doped Au (0.12)[188]. However, besides an idealized assumption about the presence of a large non-leaky bandgap (perhaps more suitable to TIs like SmB_6 than Bi_2Se_3), it is also worth emphasizing that the spin 'amplification' effect was studied on a homogeneous TIPNJ, where the source/drain contacts are assumed to be extensions of the TI surface as well. While it is easy to over-generalize the high charge-to-spin conversion efficiency to the TI-ferromagnet interface, it is not a straightforward equivalence to the homogeneous TI surface and deserves proper analysis. A PN junction provides a gate tunable filter on the spins. For sufficient current densities it can flip a low barrier in-plane magnet unidirectionally. The latter can be flipped back with an oppositely directed current in a symmetric set-up. The low barrier magnet is useful for three-terminal stochastic computing [189, 190], where the PN junction provides a gate tunability of the average magnetization that follows a neuron-like nonlinear activation function. The model we used for simulating

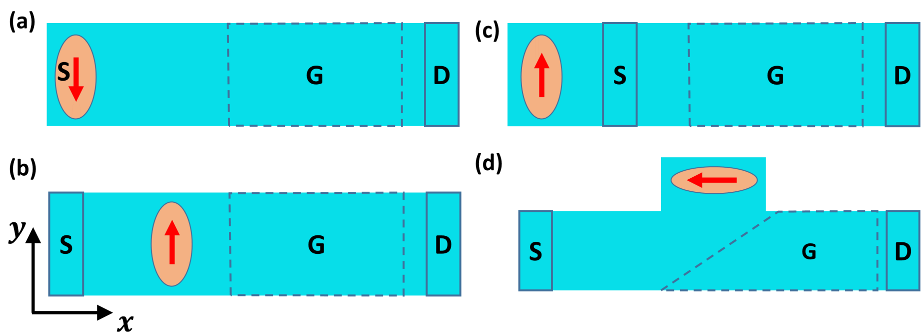

Figure 6.5: Top view of different configurations of nanomagnet on a TIPNJ. (a) Nanomagnet as the source contact. (b) Floating nanomagnet located between source and drain contacts. (c) Floating nanomagnet outside the source-drain path. (d) A variation of the out-of-location floating nanomagnet. The gate (PN junction interface) is at 45° degree from the source-drain direction. The angled PN junction can reflect electrons from the source to the nanomagnet.

the charge/spin transport in the combined system of a TIPNJ and a nanomagnet: $H_{\mathrm{TSS}} = v_F \hat{\mathbf{z}} \cdot (\boldsymbol{\sigma} \times \mathbf{p})$. To discretize this Hamiltonian, a Wilson mass term needs to be added to avoid the fermion doubling problem [191]:

$$\begin{aligned} H_{\mathrm{TSS}} &= v_F \hat{\mathbf{z}} \cdot (\boldsymbol{\sigma} \times \mathbf{p}) + \gamma \hbar v_F \sigma_z (k_x^2 + k_y^2) \\ &= \sum_i c_i^\dagger \varepsilon_{\mathrm{TI}} c_i + \sum_i \left(c_{i,i}^\dagger t_x c_{i,i+1} + \mathrm{H.C.} \right) \\ &\qquad + \sum_j \left(c_{j,j}^\dagger t_y c_{j,j+1} + \mathrm{H.C.} \right) \end{aligned} \tag{6.6}$$

where $\varepsilon_{\mathrm{TI}} = -4\hbar v_F \alpha \sigma^z / a$, $t_x = \hbar v_F [i\sigma^y/2 + \alpha\sigma^z]/a$, $t_y = \hbar v_F[-i\sigma^x/2 + \alpha\sigma^z]/a$. $a = 5$ is the grid spacing, $v_F = 0.5 \times 10^6\,\mathrm{m/s}$, and $\alpha = \gamma/a$ is a fitting parameter set to $\alpha = 1$ to generate a bandstructure that reproduces the ideal linear bands within a energy window of 0.5 eV [185]. $\hat{\mathbf{z}}$ is the normal vector to the surface and v_F is the speed of electrons near the Dirac point. A generic ferromagnetic (FM) nanomagnet is modeled by a tight-binding Hamiltonian in a cubic lattice with a single orbital per site:

$$\begin{aligned} H_{\mathrm{FM}} = \sum_{i,\sigma,\sigma'} c_{i\sigma}^{\dagger} \left(\varepsilon_{\mathrm{FM}} \delta_{\sigma\sigma'} - \frac{\boldsymbol{\Delta}}{2} \cdot \boldsymbol{\sigma} \right) c_{i\sigma'} \\ - t \sum_{i,i',\sigma} \left(c_{i\sigma}^{\dagger} c_{i'\sigma} + \mathrm{H.C.} \right) \end{aligned} \tag{6.7}$$

where $\varepsilon_{\mathrm{FM}}$ is the onsite energy. $\boldsymbol{\Delta} = \Delta \mathbf{m}$ is the exchange energy split along the direction of the magnetization $\mathbf{m}$. i' goes through all neighbors of site i. $t = \hbar^2/2m^* a^2$ is the electron hopping energy with effective electron mass m^*. The hopping term between the FM and TI surface is tuned to $t_{\mathrm{FM-TI}} = 2.3t$ to minimize the contact resistance. The FM parameters $m^* = 0.5m_e$, $\varepsilon_{\mathrm{FM}} = 1.3\,\mathrm{eV}, \Delta = 0.8\,\mathrm{eV}$ result in a spin polarization $\eta = (D_\uparrow - D_\downarrow)/(D_\uparrow + D_\downarrow) \approx 0.57$ around the Fermi energy with density of states $D_\uparrow = 1.34 \times 10^{46}\,\mathrm{J^{-1}m^{-3}}, D_\downarrow = 0.357 \times 10^{46}\,\mathrm{J^{-1}m^{-3}}$ for the spin up $(-y)$/down $(+y)$ channels. These numbers are a bit lower than the nanomagnet modeled in [192], mostly due to the reduced size of our simulated magnet. The TI surface is assumed to be doped N-type with a single gate controlling the drain side. The periodic boundary condition is adopted in the y direction and characterized by the transverse quasi-momentum $\mathbf{k}_\perp$. The bias induced carrier density $n = n_{\mathrm{neq}} - n_{\mathrm{eq}}$ where $n_{\mathrm{neq}}, n_{\mathrm{eq}}$ are obtained from:

$$\begin{aligned} n_{\mathrm{eq}} &= -\frac{1}{\pi} \mathbf{Tr} \left(\sum_{\mathbf{k}_\perp} \int dE \,\mathbf{Im}(G^r(E, k_\perp)) \right) f_0(E) \\ n_{\mathrm{neq}} &= \frac{1}{2\pi i} \mathbf{Tr} \left(\sum_{\mathbf{k}_\perp} \int dE G^n(E, k_\perp) \right) \end{aligned} \tag{6.8}$$

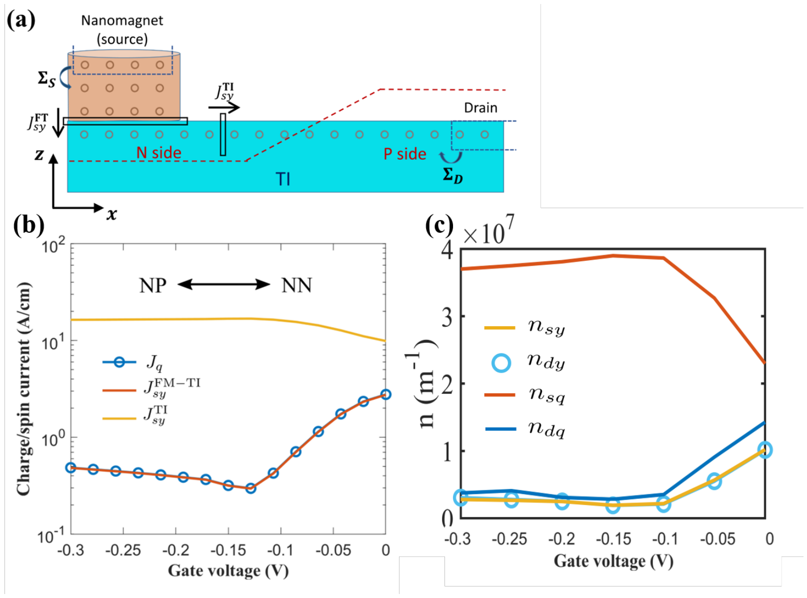

Figure 6.6: I-V characteristic of TIPNJ with a ferromagnetic source contact. (a) TIPNJ setup with a nanomagnet as the source. The magnetization of the FM contact is oriented to the $-y$ direction. The gate contact is present but not visualized in the schematic. (b) Charge and spin current densities calculated at different locations. J_q is the charge current density (conserved throughout the system). J_{sy}^{TI} is the spin current (polarized along $-y$ direction) calculated on the TI surface on the source side (N side). $J_{sy}^{\mathrm{FM-TI}}$ is the spin current density at the FM-TI interface. The source-drain bias V_{sd} is fixed at 0.1 V and the magnetization of the nanomagnet is aligned in the $-y$ direction. (c) Spin density shows almost no change with gate voltage and is the same in the source and drain side of TI. This indicates that the spin current amplification in the source region of TI can not be used for magnet switching.

where f_0 is the equilibrium Fermi-Dirac distribution. Our previous work[185] showed that the TIPNJ acts like a spin collimator that increases the non-equilibrium spin current while reducing the charge current at the same time. The corresponding spin-to-charge ratio (the longitudinal equivalent of the Spin Hall Angle θ_{SH}) at the source contact can go up to as high as 20 [185]. While it is easy to assume that this conversion would dramatically improve the switching efficiency if we replace the 'TI source contact' with a ferromagnetic contact, we show here that the impressive gain is limited to the TI surface (we refer to this as the 'intrinsic' gain). To see the difference between the intrinsic and the external gain, we calculated the spin current at two locations along the transport direction: one between the FM contact and the TI surface, the other one on the N-type TI surface, as indicated in Fig. 6.6(a). Fig. 6.6(b) compares the charge current with the spin currents at the above-mentioned locations as a function of the gate voltage. As the gate voltage sweeps from $-0.3\,\mathrm{V}$ to $0\,\mathrm{V}$, the TI surface transitions from a PN junction to a homogeneous N-type surface. The behavior of the charge current (independent of where it is being calculated) and TI surface spin current J_{sy}^{TI}, with a maximum ratio of $J_{sy}^{\mathrm{TI}}/J_q > 20$ resembles the results from [185], where the PN junction effectively suppresses the charge current while amplifying the nonequilibrium spin current. However, the spin current across the nanomagnetic contact $J_{sy}^{\mathrm{FM-TI}}$ does not follow the in-plane surface spin current but instead follows the charge current. While the ratio $J_{sy}^{\mathrm{FM-TI}}/J_q$ is very close to 100%, $J_{sy}^{\mathrm{FM-TI}}$ never exceeds the charge current regardless of which regime the TI surface is in. Looking at the bias-induced charge and spin carrier density, we can see the picture more clearly (Fig. 6.6.c). The spin density shows no change on the source and drain sides of TI. However, the charge densities show significant variations in the source and drain regions (opposite of currents' behavior). This further solidifies the above explanation, as the charge densities from the incoming and reflected currents add up in the source region but are subtracted for spin density. To better understand this discrepancy, we look at the individual Fermi levels f_μ in each spin channel (where spin-up corresponds to $-y$ while spin-down corresponds to $+y$) on the TI surface (Fig. 6.7). The Fermi levels are calculated by simulating a magnetic probe at each lattice point which draws net zero currents from the channel with negligible deformation of the channel Hamiltonian. The calculated quantity is $f_\mu = \frac{Tr(\Gamma_{\mathrm{FM}} G^n)}{Tr(\Gamma_{\mathrm{FM}} A)}$ [191] where $\Gamma_{\mathrm{FM}}(\pm y) = \gamma_m(I \pm \sigma_y)$ is the coupling between FM probe and the TI surface with $\gamma_m \ll \hbar v_f/a$ being the coupling strength. Due to the spin-momentum locking of

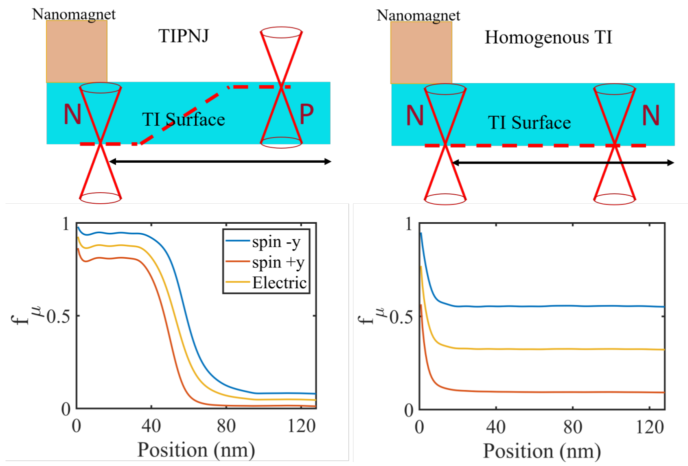

Figure 6.7: Fermi levels f_μ for different spin channels on the TI surface in different regimes (TIPNJ versus homogeneous TI surface). $\mu_s(\mu_d)$ is the Fermi level of the source (drain) contact. As can be seen from the comparison, PN junction raises the Fermi level of all spin channels on the source side due to the reflection of the junction potential barrier. The biggest potential drop happens near the junction interface. In the case of homogeneous TI, the Fermi level remains uniform throughout the TI surface from the source to the drain.

the TI surface states, electrons in the spin-up channel can only move in the $+x$ direction while electrons in the spin-down channel move in the opposite direction, roughly along two one-way streets (for 3D TSS, the angular transition is continuous)[193]. This behavior results in the 'intrinsic' spin amplification observed on the TI surface: non-equilibrium electrons moving in opposite directions due to electron reflection at the PN junction reduce the net charge current while increasing the net nonequilibrium spin current. However, when the nanomagnet contact exchanges electrons with the TI surface, the electrons flow bidirectionally regardless of their spin orientations. Ultimately, the rate of influx and outflow of spins from the nanomagnet is controlled by the difference in the electrochemical potentials between the magnet and the TI surface. Being the source contact, the magnet has the highest electrochemical potential in both spin channels. Therefore one expects a net outflow of electrons from the magnet to the TI surface in both spin channels. The net spin current is just the difference between the charge currents in different spin channels, which is always lower than the sum of them. The extrinsic spin amplification in this configuration, with the magnet doubling as the current source, cannot exceed unity.

The limit on external charge-to-spin gain is imposed by having the nanomaget as the source contact. A more common setup is to have a floating nanomagnet on top of a TI (see fig. 6.5(b)). There are several research papers that discuss this configuration (without a PN junction) in detail, such as the proximity effect induced by the magnetic field from the magnet [194], and the shunting of the charge current from the TI surface to a conductive magnetic layer [192]. With this configuration, the electrochemical potential of the nanomagnet is free to adjust in order to draw a net zero charge current.

The charge-to-spin conversion rate depends on the splitting of the electrochemical potentials of the opposite spin channels. With TIPNJ, Fig. 6.7 shows that the splitting narrows compared to the homogeneous TI surface, which means the PN junction effectively turns off the spin torque from the TI surface.

Because of the current shunting to the bulk of the 3DTI, the surface spin current calculated from TSS Hamiltonian Eq. 6.6 is overestimated. To study the surface-bulk current distribution, the 3DTI Hamiltonian as described in Eq. 6.2 is employed. With equation 6.3b, the current density for each layer is calculated and separated into bulk and surface currents. To get a simple resistance model, we use two parallel resistances for bulk R_b and surface R_s. Based on the current distributions, the ratio of resistances is calculated. Here we define the surface current as the current in the top (bottom) layers: starting from the top (bottom) surface layer to the layer where the current density is peaked as shown in Fig. 6.8.c. TSS has a practical limitation on how much current increases with applied bias. For electrons with higher energies that are only accessible with a higher bias, the conductive state will no longer be

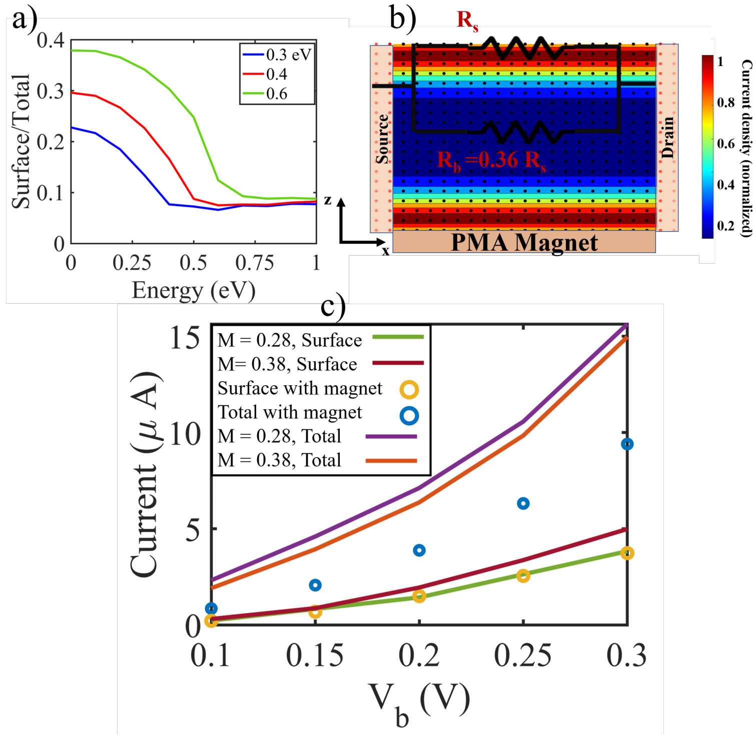

Figure 6.8: a) The ratio of TSS-to-Bulk current contributions as a function of the bulk band gap for various carrier energies. We simulate different bulk bandgaps by varying M 0.28, 0.38 and 0.55 eV . For electron energies inside the bulk bandgap, the TSS dominate. We see that for energies above the band gap the TSS is weakly localized. b) Current distribution and a corresponding simple resistance model for Bi_3Se_2 (with a bulk gap of 0.3 eV) at 0.2 V applied bias. The magnetic layer with perpendicular anisotropy (PMA) inserted between the bottom TI surface and the substrate (not shown) shows a possible way to lower the shunting effect. c) The surface current is defined as the current in the top layers; from the top layer to the layer with peaked current density. d) Two ways to improve the surface-to-bulk current ratio: with a larger bulk band gap, the surface current increases while the total current decreases. Alternatively, by inserting a magnetic layer with perpendicular anisotropy at the bottom surface, the total current is reduced while the current at the opposite surface is almost unaffected, translating to a higher contribution for the top surface. V_s and V_d are $\pm V_b/2$

.

strongly localized at the surface and will shunt into the bulk (Fig. 6.8(a)). Such a shunting [195] implies that a significant portion of the current will be diverted away from the surface, reducing the carrier exchange between the FM and TI and degrading the switching efficiency. Increasing the bias above the bulk bandgap will therefore have diminishing returns. For example, for Bi_2Se_3 the localized current at the surface (about 2nm thick, Fig. 6.8.b) carries only 30% of the total current. One way to alleviate this is by finding a 3DTI material with a larger bulk bandgap, as can be seen in Fig 6.8(a,b). Alternatively, inserting or doping the TI surface in contact with the substrate (Fig. 6.8b,d) the 3DTI grown on with a PMA magnet can also increase θ_{SH}. This is due to the fact that out-of-plane Zeeman energy [196, 197, 198, 199] opens up a gap. Since this effect is localized only at one surface, the opposite surface is nearly unaffected. However, the total current is now smaller as the total resistance of the channel is increased.

6.3 Summary

In this chapter, we proposed an in-memory processing device based on the reciprocal interactions in FM-3DTI heterostructures. The main advantage is the compactness of the in-built selector-memory unit. Using DFT-calibrated 3D tight binding, NEGF-LLG and Fokker-Planck, we connected the material parameters to switching delay and WER. We showed that a modest ON-OFF suffices for selector action in cache memory, even in the presence of current shunting through the sides and bulk. Furthermore, we studied the TIPNJ with realistic three dimensional geometry and clarified the discrepancy that can come out from calculating spin current in such a device. We also looked at the spin current shunting into the bulk of 3DTI and saw that it could make up a major part of the total current.

Chapter 7

Conclusion and Future Work

The focus of this dissertation was to look at two main challenges in the field of spintronics. The first challenge is the size and speed limit of an FM based device. We tried to address that question by making use of skyrmions. The topological stability of skyrmions makes them a promising candidate to push the limits of spintronics devices based on skyrmions. We looked at skyrmions from a fundamental level up to the device level applications. We started with the energetics of static skyrmions and their phase diagram. Then we looked at the dynamics of hybrid skyrmions and their self focusing behavior. Finally, we proposed a few applications for skyrmions and addressed one of their main challenges: their positional stability. To study the positional stability of skyrmions, we developed a sting method to find MEP between two sides of a notch. The main conclusions from this part of the dissertation are the reliability of skyrmions in nucleation, annihilation, moving, and reading are crucial for the realization of competitive skyrmionic based devices. This would require material level studies to discover materials with more favorable properties. In addition, a further device level analysis can help with finding more reliable ways of using skyrmions. We saw that an isolated skyrmion movement is more reliable when compared to multi skyrmion movements. A Fokker-Planck study of the behavior of single and multiple skyrmions in the presence of forces from edges and defects would help study skyrmions' reliability. Finally, to have a complete understanding of the skyrmion positional lifetime, the entropic contributions to the skyrmion positional lifetime needs to be accurately calculated by using methods such as transition state theory with atomistic models.

For the second main challenge of the field spintronics, efficiently and reliably generating spin currents, we turned to TIs. The spin surface current generated by the 3DTI shows promising capabilities to generate spin current efficiently. We saw that the interaction between FM and TI provides a way to tune the surface state of TI. We proposed a RAM, based on two FM/3DTI heterostructures used together. However, we saw that the exchange coupling between an FM and topological insulator needs to be large enough for a device based on FM/3DTI heterostructure to work reliably. Moreover, the voltage control of FM to tune the surface state of TI needs to be within the practical limit of an electric circuit. Ab-initio studies of interfacial properties of FM/3DTI for various combinations of 3DTI and FM materials can give an answer to these questions. Finally, developing a spin circuit model for a device based on FM/3DTI heterostructure would speed up the numerical simulations by orders of magnitude and provide an accurate calculation of the energy consumption of the device by including the overhead energy consumption.

List of Publications

1. H. Vakili, Y. Xie, and A. W. Ghosh, “Self-focusing hybrid skyrmions in spatially varying canted ferromagnetic systems,” Phys. Rev. B, vol. 102, p. 174420, Nov 2020.

2. Y. Xie, J. Ma, H. Vakili, Y. Tan and A. W. Ghosh "Computational Search for Ultrasmall and Fast Skyrmions in the Inverse Heusler Family", IEEE Transactions on Magnetics, 1500108

3. H. Vakili, M. N. Sakib, S. Ganguly, M. Stan, M. W. Daniels, A. Madhavan, M. D. Stiles, and A. W. Ghosh, “Temporal Memory With Magnetic Racetracks,” IEEE J. Explor. Solid-State Comput. Devices Circuits, vol. 6, pp. 107–115, Sep 2020.

4. H. Vakili, J.-W. Xu, W. Zhou, M. N. Sakib, M. G. Morshed, T. Hartnett, Y. Quessab, K. Litzius, C. T. Ma, S. Ganguly, M. R. Stan, P. V. Balachan- dran, G. S. D. Beach, S. J. Poon, A. D. Kent, and A. W. Ghosh, “Skyrmionics Computing and memory technologies based on topological excitations in magnets,” J. Appl. Phys., vol. 130, p. 070908, Aug 2021.

5. M. G. Morshed, H. Vakili (co-first author), and A. W. Ghosh, “Positional stability of skyrmions in a racetrack memory with notched geometry,” arXiv:2110.13445 [cond-mat], Dec. 2021. arXiv: 2110.13445. Submitted to PR Applied

6. H. Vakili, Y. Xie, S. Ganguly, and A. W. Ghosh, “Anatomy of nanomagnetic switching at a 3D Topological Insulator PN junction,” arXiv:2110.02641 [cond- mat], Nov. 2021. arXiv: 2110.02641. Submitted to PR Applied

7. H. Vakili, S. Ganguly, G. J. de Coster, M. R. Neupane, and A. W. Ghosh, "Low power In Memory Computation with Reciprocal Ferromagnet/Topological Insulator Heterostructures," arXiv:2203.14389 [cond-mat], Mar. 2022. arXiv: 2203.14389. Submitted to APL

References

[1] H. Vakili, J.-W. Xu, W. Zhou, M. N. Sakib, M. G. Morshed, T. Hartnett, Y. Quessab, K. Litzius, C. T. Ma, S. Ganguly, M. R. Stan, P. V. Balachandran, G. S. D. Beach, S. J. Poon, A. D. Kent, and A. W. Ghosh, "Skyrmionics—computing and memory technologies based on topological excitations in magnets," *Journal of Applied Physics*, vol. 130, no. 7, p. 070908, 2021.

[2] M. Xu, M. Li, P. Khanal, A. Habiboglu, B. Insana, Y. Xiong, T. Peterson, J. C. Myers, D. Ortega, H. Qu, C. L. Chien, W. Zhang, J.-P. Wang, and W. G. Wang, "Voltage-controlled antiferromagnetism in magnetic tunnel junctions," *Phys. Rev. Lett.*, vol. 124, p. 187701, May 2020.

[3] A. D. Kent and D. C. Worledge, "A new spin on magnetic memories," *Nature Nanotechnology*, vol. 10, pp. 187–191, Mar. 2015.

[4] L. Thomas, G. Jan, S. Le, S. Serrano-Guisan, Y.-J. Lee, H. Liu, J. Zhu, J. Iwata-Harms, R.-Y. Tong, S. Patel, V. Sundar, D. Shen, Y. Yang, R. He, J. Haq, Z. Teng, V. Lam, P. Liu, Y.-J. Wang, T. Zhong, and P.-K. Wang, "Stt-mram for embedded memory applications from envm to last level cache," *2017 IEEE SOI-3D-Subthreshold Microelectronics Technology Unified Conference (S3S)*, pp. 1–4, 2017.

[5] J. M. Slaughter, K. Nagel, R. Whig, S. Deshpande, S. Aggarwal, M. DeHerrera, J. Janesky, M. Lin, H. Chia, M. Hossain, S. Ikegawa, F. Mancoff, G. Shimon, J. Sun, M. Tran, T. Andre, S. Alam, F. Poh, J. Lee, Y. Chow, Y. Jiang, H. Liu, C. Wang, S. Noh, T. Tahmasebi, S. Ye, and D. Shum, "Spin-torque MRAM product status and technology for 40nm, 28nm and 22nm nodes," *2017 IEEE International Magnetics Conference (INTERMAG)*, pp. 1–1, April 2017.

[6] M. N. Baibich, J. M. Broto, A. Fert, F. N. Van Dau, F. Petroff, P. Etienne, G. Creuzet, A. Friederich, and J. Chazelas, "Giant magnetoresistance of (001)fe/(001)cr magnetic superlattices," *Phys. Rev. Lett.*, vol. 61, pp. 2472–2475, Nov 1988.

[7] G. Binasch, P. Grünberg, F. Saurenbach, and W. Zinn, "Enhanced magnetoresistance in layered magnetic structures with antiferromagnetic interlayer exchange," *Phys. Rev. B*, vol. 39, pp. 4828–4830, Mar 1989.

[8] J. C. Slonczewski, "Conductance and exchange coupling of two ferromagnets separated by a tunneling barrier," *Phys. Rev. B*, vol. 39, pp. 6995–7002, Apr 1989.

[9] J. Slonczewski, "Current-driven excitation of magnetic multilayers," *Journal of Magnetism and Magnetic Materials*, vol. 159, no. 1, pp. L1–L7, 1996.

[10] L. Berger, "Emission of spin waves by a magnetic multilayer traversed by a current," *Phys. Rev. B*, vol. 54, pp. 9353–9358, Oct 1996.

[11] S. I. Kiselev, J. C. Sankey, I. N. Krivorotov, N. C. Emley, R. J. Schoelkopf, R. A. Buhrman, and D. C. Ralph, "Microwave oscillations of a nanomagnet driven by a spin-polarized current," *Nature*, vol. 425, no. 6956, pp. 380–383, 2003.

[12] T. Gilbert, "A phenomenological theory of damping in ferromagnetic materials," *IEEE Transactions on Magnetics*, vol. 40, no. 6, pp. 3443–3449, 2004.

[13] J. P. Kim, T. Kim, W. Hao, H. M. Rao, K. Lee, X. Zhu, X. Li, W. Hsu, S. H. Kang, N. Matt, and N. Yu, "A 45nm 1Mb embedded STT-MRAM with design techniques to minimize read-disturbance," *2011 Symposium on VLSI Circuits - Digest of Technical Papers*, pp. 296–297, 2011.

[14] Q. Shao, P. Li, L. Liu, H. Yang, S. Fukami, A. Razavi, H. Wu, K. L. Wang, F. Freimuth, Y. Mokrousov, M. D. Stiles, S. Emori, A. Hoffmann, J. Åkerman, K. Roy, J.-P. Wang, S.-H. Yang, K. Garello, and W. Zhang, "Roadmap of spin-orbit torques," *arXiv*, apr 2021.

[15] S. Rohart and A. Thiaville, “Skyrmion confinement in ultrathin film nanostructures in the presence of dzyaloshinskii-moriya interaction,” *Phys. Rev. B*, vol. 88, p. 184422, Nov 2013.

[16] A. N. Bogdanov and U. K. Rößler, “Chiral symmetry breaking in magnetic thin films and multilayers,” *Phys. Rev. Lett.*, vol. 87, p. 037203, Jun 2001.

[17] F. Büttner, I. Lemesh, and G. S. D. Beach, “Theory of isolated magnetic skyrmions: From fundamentals to room temperature applications,” *Scientific Reports*, vol. 8, no. 1, p. 4464, 2018.

[18] X. S. Wang, H. Y. Yuan, and X. R. Wang, “A theory on skyrmion size,” *Communications Physics*, vol. 1, no. 1, p. 31.

[19] A. A. Thiele, “Steady-state motion of magnetic domains,” *Phys. Rev. Lett.*, vol. 30, pp. 230–233, Feb 1973.

[20] A. Hrabec, J. Sampaio, M. Belmeguenai, I. Gross, R. Weil, S. M. Chérif, A. Stashkevich, V. Jacques, A. Thiaville, and S. Rohart, “Current-induced skyrmion generation and dynamics in symmetric bilayers,” *Nature Communications*, vol. 8, no. 1, p. 15765, 2017.

[21] R. Tomasello, E. Martinez, R. Zivieri, L. Torres, M. Carpentieri, and G. Finocchio, “A strategy for the design of skyrmion racetrack memories,” *Scientific Reports*, vol. 4, p. 6784, 2014.

[22] K. Litzius, I. Lemesh, B. Krüger, P. Bassirian, L. Caretta, K. Richter, F. Büttner, K. Sato, O. A. Tretiakov, J. Förster, R. M. Reeve, M. Weigand, I. Bykova, H. Stoll, G. Schütz, G. S. D. Beach, and M. Kläui, “Skyrmion hall effect revealed by direct time-resolved x-ray microscopy,” *Nature Physics*, vol. 13, no. 2, pp. 170–175, 2017.

[23] K. Litzius, J. Leliaert, P. Bassirian, D. Rodrigues, S. Kromin, I. Lemesh, J. Zazvorka, K.-j. Lee, J. Mulkers, N. Kerber, D. Heinze, N. Keil, R. M. Reeve, M. Weigand, B. Van Waeyenberge, G. Schütz, K. Everschor-Sitte, G. S. D. Beach, and M. Kläui, “The role of temperature and drive current in skyrmion dynamics,” *Nature Electronics*, vol. 3, pp. 30–36, jan 2020.

[24] N. Romming, C. Hanneken, M. Menzel, J. E. Bickel, B. Wolter, K. von Bergmann, A. Kubetzka, and R. Wiesendanger, "Writing and deleting single magnetic skyrmions," *Science*, vol. 341, no. 6146, pp. 636–639, 2013.

[25] H. Vakili, Y. Xie, and A. W. Ghosh, "Self focusing hybrid skyrmions in spatially varying canted ferromagnetic systems," *arXiv:2001.00729*.

[26] S. Woo, K. Litzius, B. Krüger, M.-Y. Im, L. Caretta, K. Richter, M. Mann, A. Krone, R. M. Reeve, M. Weigand, P. Agrawal, I. Lemesh, M.-A. Mawass, P. Fischer, M. Kläui, and G. S. D. Beach, "Observation of room-temperature magnetic skyrmions and their current-driven dynamics in ultrathin metallic ferromagnets," *Nature Materials*, vol. 15, no. 5, pp. 501–506, 2016.

[27] S. Seki, X. Yu, S. Ishiwata, and Y. Tokura, "Observation of skyrmions in a multiferroic material," *Science*, vol. 336, no. 6078, pp. 198–201, 2012.

[28] N. Nagaosa and Y. Tokura, "Topological properties and dynamics of magnetic skyrmions," *Nature Nanotechnology*, vol. 8, no. 12, pp. 899–911, 2013.

[29] R. Tomasello, S. Komineas, G. Siracusano, M. Carpentieri, and G. Finocchio, "Chiral skyrmions in an anisotropy gradient," *Phys. Rev. B*, vol. 98, p. 024421, Jul 2018.

[30] H. Fook, C. A. C. Ian, W. Gan, I. Purnama, and W. Lew, "Mitigation of magnus force in current-induced skyrmion dynamics," pp. 1–1, May 2015.

[31] X. Zhang, Y. Zhou, and M. Ezawa, "Magnetic bilayer-skyrmions without skyrmion Hall effect," *Nature Communications*, vol. 7, p. 10293, Apr. 2016.

[32] S. K. Kim, K.-J. Lee, and Y. Tserkovnyak, "Self-focusing skyrmion racetracks in ferrimagnets," *Physical Review B*, vol. 95, p. 140404, Apr. 2017.

[33] K.-W. Kim, K.-W. Moon, N. Kerber, J. Nothhelfer, and K. Everschor-Sitte, "Asymmetric skyrmion Hall effect in systems with a hybrid Dzyaloshinskii-Moriya interaction," *Physical Review B*, vol. 97, p. 224427, June 2018.

[34] H. Z. Wu, B. F. Miao, L. Sun, D. Wu, and H. F. Ding, "Hybrid magnetic skyrmion," *Physical Review B*, vol. 95, p. 174416, May 2017.

[35] A. O. Leonov and M. Mostovoy, “Edge states and skyrmion dynamics in nanostripes of frustrated magnets,” *Nature Communications*, vol. 8, no. 1, p. 14394, 2017.

[36] S. A. Díaz and R. E. Troncoso, “Controlling skyrmion helicity via engineered Dzyaloshinskii–Moriya interactions,” *Journal of Physics: Condensed Matter*, vol. 28, p. 426005, Oct. 2016.

[37] H. Zhang, D. Zhu, W. Kang, Y. Zhang, and W. Zhao, “Stochastic computing implemented by skyrmionic logic devices,” *Phys. Rev. Applied*, vol. 13, p. 054049, May 2020.

[38] M. N. Sakib, H. Vakili, S. Ganguly, S. Mosanu, A. W. Ghosh, and M. Stan, “Magnetic skyrmion-based programmable hardware,” in *Spintronics XIII* (H.-J. M. Drouhin, J.-E. Wegrowe, and M. Razeghi, eds.), vol. 11470, pp. 129 – 140, International Society for Optics and Photonics, SPIE, 2020.

[39] J. Rowland, S. Banerjee, and M. Randeria, “Skyrmions in chiral magnets with Rashba and Dresselhaus spin-orbit coupling,” *Physical Review B*, vol. 93, p. 020404, Jan. 2016.

[40] R. Tomasello, E. Martinez, R. Zivieri, L. Torres, M. Carpentieri, and G. Finocchio, “A strategy for the design of skyrmion racetrack memories,” *Scientific Reports*, vol. 4, p. 6784, May 2015.

[41] L. Liu, O. J. Lee, T. J. Gudmundsen, D. C. Ralph, and R. A. Buhrman, “Current-Induced Switching of Perpendicularly Magnetized Magnetic Layers Using Spin Torque from the Spin Hall Effect,” *Physical Review Letters*, vol. 109, p. 096602, Aug. 2012.

[42] F. Büttner, I. Lemesh, and G. S. D. Beach, “Theory of isolated magnetic skyrmions: From fundamentals to room temperature applications,” *Scientific Reports*, vol. 8, p. 4464, Dec. 2018.

[43] S. Rohart and A. Thiaville, “Skyrmion confinement in ultrathin film nanostructures in the presence of Dzyaloshinskii-Moriya interaction,” *Physical Review B*, vol. 88, p. 184422, Nov. 2013.

[44] Y. Xie, J. Ma, H. Vakilitaleghani, Y. Tan, and A. W. Ghosh, "Computational search for ultrasmall and fast skyrmions in the inverse heusler family," *IEEE Transactions on Magnetics*, vol. 56, no. 7, pp. 1–8, 2020.

[45] A. Vansteenkiste, J. Leliaert, M. Dvornik, M. Helsen, F. Garcia-Sanchez, and B. Van Waeyenberge, "The design and verification of MuMax3," *AIP Advances*, vol. 4, p. 107133, Oct. 2014.

[46] E. Turgut, H. Paik, K. Nguyen, D. A. Muller, D. G. Schlom, and G. D. Fuchs, "Engineering Dzyaloshinskii-Moriya interaction in B20 thin-film chiral magnets," *Physical Review Materials*, vol. 2, p. 074404, July 2018.

[47] C. Dhital, L. DeBeer-Schmitt, Q. Zhang, W. Xie, D. P. Young, and J. F. DiTusa, "Exploring the origins of the Dzyaloshinskii-Moriya interaction in MnSi," *Physical Review B*, vol. 96, p. 214425, Dec. 2017.

[48] *We are treating skyrmion as a point particle with zero dimensions. Since DMI is linearly varying this assumption will result in a small disagreement with LLG simulations.*

[49] S. Tacchi, R. Troncoso, M. Ahlberg, G. Gubbiotti, M. Madami, J. Åkerman, and P. Landeros, "Interfacial Dzyaloshinskii-Moriya Interaction in Pt / CoFeB Films: Effect of the Heavy-Metal Thickness," *Physical Review Letters*, vol. 118, p. 147201, Apr. 2017.

[50] A. Cao, X. Zhang, B. Koopmans, S. Peng, Y. Zhang, Z. Wang, S. Yan, H. Yang, and W. Zhao, "Tuning the Dzyaloshinskii–Moriya interaction in Pt/Co/MgO heterostructures through the MgO thickness," *Nanoscale*, vol. 10, no. 25, pp. 12062–12067, 2018.

[51] L. Zhu, K. Sobotkiewich, X. Ma, X. Li, D. C. Ralph, and R. A. Buhrman, "Strong Damping-Like Spin-Orbit Torque and Tunable Dzyaloshinskii–Moriya Interaction Generated by Low-Resistivity Pd $_{1-x}$ Pt $_x$ Alloys," *Advanced Functional Materials*, vol. 29, p. 1805822, Apr. 2019.

[52] D. Lau and V. Sokalski, "The interfacial Dzyaloshinskii-Moriya interaction and spin-orbit torque driven domain wall motion in Co/Ni multi-layers with a Pt $_x$ (Ir,Au) $_{1-x}$ seedlayer," *AIP Advances*, vol. 9, p. 035208, Mar. 2019.

[53] S. Kanai, M. Yamanouchi, S. Ikeda, Y. Nakatani, F. Matsukura, and H. Ohno, "Electric field-induced magnetization reversal in a perpendicular-anisotropy cofeb-mgo magnetic tunnel junction," *Applied Physics Letters*, p. 122403, 2012.

[54] F. Xue, N. Sato, C. Bi, J. Hu, J. He, and S. X. Wang, "Large voltage control of magnetic anisotropy in CoFeB/MgO/OX structures at room temperature," *APL Materials*, vol. 7, p. 101112, Oct. 2019.

[55] B. Rana and Y. Otani, "Towards magnonic devices based on voltage-controlled magnetic anisotropy," *Communications Physics*, vol. 2, p. 90, Dec. 2019.

[56] T. Nozaki, T. Yamamoto, S. Miwa, M. Tsujikawa, M. Shirai, S. Yuasa, and Y. Suzuki, "Recent Progress in the Voltage-Controlled Magnetic Anisotropy Effect and the Challenges Faced in Developing Voltage-Torque MRAM," *Micromachines*, vol. 10, p. 327, May 2019.

[57] B. Zhang, L. Wu, J. Zheng, P. Yang, X. Yu, J. Ding, S. M. Heald, R. A. Rosenberg, T. V. Venkatesan, J. Chen, C.-J. Sun, Y. Zhu, and G. M. Chow, "Control of magnetic anisotropy by orbital hybridization with charge transfer in (La0.67sr0.33mno3)n/(SrTiO3)n superlattice," *NPG Asia Materials*, vol. 10, pp. 931–942, Sept. 2018.

[58] H. Vakili, M. N. Sakib, S. Ganguly, M. Stan, M. W. Daniels, A. Madhavan, M. D. Stiles, and A. W. Ghosh, "Temporal memory with magnetic racetracks," *IEEE Journal on Exploratory Solid-State Computational Devices and Circuits*, vol. 6, no. 2, pp. 107–115, 2020.

[59] Y. Chen, J. Zhao, and Y. Xie, "3d-nonfar: Three-dimensional non-volatile fpga architecture using phase change memory," in *Proceedings of the 16th ACM/IEEE international symposium on Low power electronics and design*, pp. 55–60, 2010.

[60] S. Paul, S. Mukhopadhyay, and S. Bhunia, "Hybrid cmos-sttram non-volatile fpga: Design challenges and optimization approaches," in *2008 IEEE/ACM International Conference on Computer-Aided Design*, pp. 589–592, IEEE, 2008.

[61] K. Liu, M. Zhao, L. Ju, Z. Jia, J. Hu, and C. J. Xue, “Applying multiple level cell to non-volatile fpgas,” *ACM Transactions on Embedded Computing Systems (TECS)*, vol. 19, no. 4, pp. 1–22, 2020.

[62] L. Bagheriye, S. Toofan, R. Saeidi, B. Zeinali, and F. Moradi, “A reduced store/restore energy mram-based sram cell for a non-volatile dynamically reconfigurable fpga,” *IEEE transactions on circuits and systems II: Express briefs*, vol. 65, no. 11, pp. 1708–1712, 2017.

[63] S. M. Williams and M. Lin, “Architecture and circuit design of an all-spintronic fpga,” in *Proceedings of the 2018 ACM/SIGDA International Symposium on Field-Programmable Gate Arrays*, pp. 41–50, 2018.

[64] S. Luo, M. Song, X. Li, Y. Zhang, J. Hong, X. Yang, X. Zou, N. Xu, and L. You, “Reconfigurable skyrmion logic gates,” *Nano Letters*, vol. 18, no. 2, pp. 1180–1184, 2018.

[65] M. N. Sakib, H. Vakili, S. Ganguly, S. Mosanu, A. W. Ghosh, and M. Stan, “Magnetic skyrmions-based programmable hardware,” *Proc. SPIE 11470, Spintronics XIII, 114703D.*

[66] M. Chauwin, X. Hu, F. Garcia-Sanchez, N. Betrabet, A. Paler, C. Moutafis, and J. S. Friedman, “Skyrmion logic system for large-scale reversible computation,” *Physical Review Applied*, vol. 12, no. 6, p. 064053, 2019.

[67] X. S. Wang, H. Y. Yuan, and X. R. Wang, “A theory on skyrmion size,” *Communications Physics*, vol. 1, p. 31, July 2018.

[68] A. Madhavan, T. Sherwood, and D. Strukov, “Race Logic: A hardware acceleration for dynamic programming algorithms,” *2014 ACM/IEEE 41st International Symposium on Computer Architecture (ISCA)*, pp. 517–528, June 2014. ISSN: 1063-6897.

[69] G. Tzimpragos, A. Madhavan, D. Vasudevan, D. Strukov, and T. Sherwood, “Boosted race trees for low energy classification,” *Proceedings of the Twenty-Forth International Conference on Architectural Support for Programming Languages and Operating Systems*, April 2019.

[70] A. Madhavan, T. Sherwood, and D.Strukov, "A 4-mm 2 180-nm-cmos 15-giga-cell-updates-per-second dna sequence alignment engine based on asynchronous race conditions," *2017 IEEE Custom Integrated Circuits Conference (CICC)*, pp. 1–4, 2017.

[71] J. Smith, "Space-time algebra: A model for neocortical computation," in *2018 ACM/IEEE 45th Annual International Symposium on Computer Architecture (ISCA)*, pp. 289–300, IEEE, 2018.

[72] A. Madhavan, G. Tzimpragos, M. Stiles, and T. Sherwood, "A truth-matrix view into unary computing,"

[73] A. Madhavan and M.D.Stiles, "Storing and retrieving wavefronts with resistivetemporal memory," *2020 IEEE International Symposium on Circuits and Systems (ISCAS)*, pp. 1–4, 2020.

[74] S. S. P. Parkin, M. Hayashi, and L. Thomas, "Magnetic Domain-Wall Racetrack Memory," *Science*, vol. 320, pp. 190–194, Apr. 2008.

[75] R. Tomasello, E. Martinez, R. Zivieri, L. Torres, M. Carpentieri, and G. Finocchio, "A strategy for the design of skyrmion racetrack memories," *Sci Rep*, vol. 4, p. 6784, May 2015.

[76] C. Hanneken, F. Otte, A. Kubetzka, B. Dupé, N. Romming, K. von Bergmann, R. Wiesendanger, and S. Heinze, "Electrical detection of magnetic skyrmions by tunnelling non-collinear magnetoresistance," *Nature Nanotechnology*, vol. 10, pp. 1039–1042, Dec. 2015.

[77] K. Y. Camsari, R. Faria, B. M. Sutton, and S. Datta, "Stochastic p -Bits for Invertible Logic," *Phys. Rev. X*, vol. 7, p. 031014, July 2017.

[78] A. Belavin and A. Polyakov, "Metastable states of two-dimensional isotropic ferromagnets," *JETP lett*, vol. 22, no. 10, pp. 245–248, 1975.

[79] A. Thiaville, J. M. García, and J. Miltat, "Domain wall dynamics in nanowires," *Journal of Magnetism and Magnetic Materials*, vol. 242-245, pp. 1061–1063, Apr. 2002.

[80] G. S. D. Beach, C. Nistor, C. Knutson, M. Tsoi, and J. L. Erskine, "Dynamics of field-driven domain-wall propagation in ferromagnetic nanowires," *Nature Mater*, vol. 4, pp. 741–744, Oct. 2005.

[81] A. N. Bogdanov and U. K. Rößler, "Chiral Symmetry Breaking in Magnetic Thin Films and Multilayers," *Phys. Rev. Lett.*, vol. 87, p. 037203, June 2001.

[82] I. Dzyaloshinsky, "A thermodynamic theory of "weak" ferromagnetism of antiferromagnetics," *Journal of Physics and Chemistry of Solids*, vol. 4, Jan. 241–255.

[83] J. Sampaio, V. Cros, S. Rohart, A. Thiaville, and A. Fert, "Nucleation, stability and current-induced motion of isolated magnetic skyrmions in nanostructures," *Nature nanotechnology*, vol. 8, no. 11, p. 839, 2013.

[84] R. Tomasello, V. Puliafito, E. Martinez, A. Manchon, M. Ricci, M. Carpentieri, and G. Finocchio, "Performance of synthetic antiferromagnetic racetrack memory: domain wall versus skyrmion," *J. Phys. D: Appl. Phys.*, vol. 50, p. 325302, Aug. 2017.

[85] X. Zhang, Y. Zhou, and M. Ezawa, "Magnetic bilayer-skyrmions without skyrmion Hall effect," *Nat Commun*, vol. 7, p. 10293, Apr. 2016.

[86] W. Legrand, D. Maccariello, F. Ajejas, S. Collin, A. Vecchiola, K. Bouzehouane, N. Reyren, V. Cros, and A. Fert, "Room-temperature stabilization of antiferromagnetic skyrmions in synthetic antiferromagnets," *Nat. Mater.*, Sept. 2019.

[87] T. Dohi, S. DuttaGupta, S. Fukami, and H. Ohno, "Formation and current-induced motion of synthetic antiferromagnetic skyrmion bubbles," *Nat Commun*, vol. 10, p. 5153, Dec. 2019.

[88] A. A. Thiele, "Steady-State Motion of Magnetic Domains," *Phys. Rev. Lett.*, vol. 30, pp. 230–233, Feb. 1973.

[89] E. G. Tveten, A. Qaiumzadeh, O. A. Tretiakov, and A. Brataas, "Staggered dynamics in antiferromagnets by collective coordinates," *Phys. Rev. Lett.*, vol. 110, p. 127208, Mar 2013.

[90] F. Büttner, I. Lemesh, and G. S. D. Beach, "Theory of isolated magnetic skyrmions: From fundamentals to room temperature applications," *Sci Rep*, vol. 8, p. 4464, Dec. 2018.

[91] J. Barker and O. A. Tretiakov, "Static and dynamical properties of antiferromagnetic skyrmions in the presence of applied current and temperature," *Phys. Rev. Lett.*, vol. 116, p. 147203, Apr 2016.

[92] M. G. Mankalale, Z. Zhao, J. Wang, and S. S. Sapatnekar, "Skylogic—a proposal for a skyrmion-based logic device," *IEEE Transactions on Electron Devices*, vol. 66, no. 4, pp. 1990–1996, 2019.

[93] "Predictive technology model (ptm), http://ptm.asu.edu,"

[94] P. F. Bessarab, G. P. Müller, I. S. Lobanov, F. N. Rybakov, N. S. Kiselev, H. Jónsson, V. M. Uzdin, S. Blügel, L. Bergqvist, and A. Delin, "Lifetime of racetrack skyrmions," *Scientific Reports*, vol. 8, no. 1, p. 3433, 2018.

[95] J. Miltat, S. Rohart, and A. Thiaville, "Brownian motion of magnetic domain walls and skyrmions, and their diffusion constants," *Phys. Rev. B*, vol. 97, p. 214426, Jun 2018.

[96] D. Suess, C. Vogler, F. Bruckner, P. Heistracher, F. Slanovc, and C. Abert, "Spin torque efficiency and analytic error rate estimates of skyrmion racetrack memory," *Scientific Reports*, vol. 9, no. 1, p. 4827, 2019.

[97] G. Beach. private communication.

[98] H. T. Fook, W. L. Gan, I. Purnama, and W. S. Lew, "Mitigation of magnus force in current-induced skyrmion dynamics," vol. 51, no. 11, pp. 1–4.

[99] K. Fallon, S. Hughes, K. Zeissler, W. Legrand, F. Ajejas, D. Maccariello, S. McFadzean, W. Smith, D. McGrouther, S. Collin, N. Reyren, V. Cros, C. H. Marrows, and S. McVitie, "Controlled individual skyrmion nucleation at artificial defects formed by ion irradiation," p. 1907450.

[100] M. G. Morshed, H. Vakili, and A. W. Ghosh, "Positional stability of skyrmions in a racetrack memory with notched geometry," *arXiv:2110.13445 [cond-mat]*, Dec. 2021. arXiv: 2110.13445.

[101] A. Fert, V. Cros, and J. Sampaio, "Skyrmions on the track - Nature Nanotechnology," *Nat. Nanotechnol.*, vol. 8, pp. 152–156, Mar 2013.

[102] B. Göbel and I. Mertig, "Skyrmion ratchet propagation: utilizing the skyrmion Hall effect in AC racetrack storage devices," *Sci. Rep.*, vol. 11, pp. 1–11, Feb 2021.

[103] A. Madhavan, T. Sherwood, and D. Strukov, "Race logic: a hardware acceleration for dynamic programming algorithms," in *ACM SIGARCH Computer Architecture News*, vol. 42, pp. 517–528, New York, NY, USA: Association for Computing Machinery, Jun 2014.

[104] D. Cortés-Ortuño, W. Wang, M. Beg, R. A. Pepper, M.-A. Bisotti, R. Carey, M. Vousden, T. Kluyver, O. Hovorka, and H. Fangohr, "Thermal stability and topological protection of skyrmions in nanotracks," *Scientific Reports*, vol. 7, p. 4060, Jun 2017.

[105] Y.-H. Liu and Y.-Q. Li, "A mechanism to pin skyrmions in chiral magnets," *J. Phys.: Condens. Matter*, vol. 25, p. 076005, Jan 2013.

[106] J. Müller and A. Rosch, "Capturing of a magnetic skyrmion with a hole," *Phys. Rev. B*, vol. 91, p. 054410, Feb 2015.

[107] H. C. Choi, S.-Z. Lin, and J.-X. Zhu, "Density functional theory study of skyrmion pinning by atomic defects in MnSi," *Phys. Rev. B*, vol. 93, p. 115112, Mar 2016.

[108] C. Reichhardt, C. J. O. Reichhardt, and M. V. Milosevic, "Statics and Dynamics of Skyrmions Interacting with Pinning: A Review," *arXiv*, Feb 2021.

[109] C. Jin, C. Song, J. Wang, and Q. Liu, "Dynamics of antiferromagnetic skyrmion driven by the spin hall effect," vol. 109, no. 18, p. 182404.

[110] J. Iwasaki, M. Mochizuki, and N. Nagaosa, "Current-induced skyrmion dynamics in constricted geometries - Nature Nanotechnology," *Nat. Nanotechnol.*, vol. 8, pp. 742–747, Oct 2013.

[111] X. Zhang, G. P. Zhao, H. Fangohr, J. P. Liu, W. X. Xia, J. Xia, and F. J. Morvan, "Skyrmion-skyrmion and skyrmion-edge repulsions in skyrmion-based racetrack memory," *Sci. Rep.*, vol. 5, pp. 1–6, Jan 2015.

[112] H. Xia, C. Jin, C. Song, J. Wang, J. Wang, and Q. Liu, "Control and manipulation of antiferromagnetic skyrmions in racetrack," *J. Phys. D: Appl. Phys.*, vol. 50, p. 505005, Nov 2017.

[113] J. Leliaert, P. Gypens, M. V. Milošević, B. Van Waeyenberge, and J. Mulkers, "Coupling of the skyrmion velocity to its breathing mode in periodically notched nanotracks," *J. Phys. D: Appl. Phys.*, vol. 52, p. 024003, Nov 2018.

[114] V. M. Uzdin, M. N. Potkina, I. S. Lobanov, P. F. Bessarab, and H. Jónsson, "The effect of confinement and defects on the thermal stability of skyrmions," *Physica B*, vol. 549, pp. 6–9, Nov 2018.

[115] D. Suess, C. Vogler, F. Bruckner, P. Heistracher, F. Slanovc, and C. Abert, "Spin torque efficiency and analytic error rate estimates of skyrmion racetrack memory," *Scientific Reports*, vol. 9, no. 1, p. 4827, 2019.

[116] Y. Huang, W. Kang, X. Zhang, Y. Zhou, and W. Zhao, "Magnetic skyrmion-based synaptic devices," *Nanotechnology*, vol. 28, p. 08LT02, jan 2017.

[117] T. Bhattacharya, S. Li, Y. Huang, W. Kang, W. Zhao, and M. Suri, "Low-Power (1T1N) Skyrmionic Synapses for Spiking Neuromorphic Systems," *IEEE Access*, vol. 7, pp. 5034–5044, Jan 2019.

[118] R. Chen, C. Li, Y. Li, J. J. Miles, G. Indiveri, S. Furber, V. F. Pavlidis, and C. Moutafis, "Nanoscale Room-Temperature Multilayer Skyrmionic Synapse for Deep Spiking Neural Networks," *Phys. Rev. Appl.*, vol. 14, p. 014096, Jul 2020.

[119] S. Liu, T. P. Xiao, C. Cui, J. A. C. Incorvia, C. H. Bennett, and M. J. Marinella, "A domain wall-magnetic tunnel junction artificial synapse with notched geometry for accurate and efficient training of deep neural networks," *Appl. Phys. Lett.*, vol. 118, p. 202405, May 2021.

[120] A. Vansteenkiste, J. Leliaert, M. Dvornik, M. Helsen, F. Garcia-Sanchez, and B. Van Waeyenberge, "The design and verification of MuMax3," *AIP Adv.*, vol. 4, p. 107133, Oct 2014.

[121] F. Büttner, I. Lemesh, and G. S. D. Beach, "Theory of isolated magnetic skyrmions: From fundamentals to room temperature applications - Scientific Reports," *Sci. Rep.*, vol. 8, pp. 1–12, Mar 2018.

[122] L. Caretta, M. Mann, F. Büttner, K. Ueda, B. Pfau, C. M. Günther, P. Hessing, A. Churikova, C. Klose, M. Schneider, D. Engel, C. Marcus, D. Bono, K. Bagschik, S. Eisebitt, and G. S. D. Beach, "Fast current-driven domain walls and small skyrmions in a compensated ferrimagnet - Nature Nanotechnology," *Nat. Nanotechnol.*, vol. 13, pp. 1154–1160, Dec 2018.

[123] Y. Quessab, J.-W. Xu, C. T. Ma, W. Zhou, G. A. Riley, J. M. Shaw, H. T. Nembach, S. J. Poon, and A. D. Kent, "Tuning interfacial dzyaloshinskii-moriya interactions in thin amorphous ferrimagnetic alloys," *Scientific Reports*, vol. 10, no. 1, p. 7447, 2020.

[124] M. G. Morshed, K. H. Khoo, Y. Quessab, J.-W. Xu, R. Laskowski, P. V. Balachandran, A. D. Kent, and A. W. Ghosh, "Tuning dzyaloshinskii-moriya interaction in ferrimagnetic gdco: A first-principles approach," *Phys. Rev. B*, vol. 103, p. 174414, May 2021.

[125] W. E, W. Ren, and E. Vanden-Eijnden, "String method for the study of rare events," *Phys. Rev. B*, vol. 66, p. 052301, Aug 2002.

[126] V. P. Kravchuk, D. D. Sheka, U. K. Rößler, J. van den Brink, and Y. Gaididei, "Spin eigenmodes of magnetic skyrmions and the problem of the effective skyrmion mass," *Phys. Rev. B*, vol. 97, p. 064403, Feb 2018.

[127] B. F. McKeever, D. R. Rodrigues, D. Pinna, A. Abanov, J. Sinova, and K. Everschor-Sitte, "Characterizing breathing dynamics of magnetic skyrmions and antiskyrmions within the hamiltonian formalism," *Phys. Rev. B*, vol. 99, p. 054430, Feb 2019.

[128] J. Wild, T. N. G. Meier, S. Pöllath, M. Kronseder, A. Bauer, A. Chacon, M. Halder, M. Schowalter, A. Rosenauer, J. Zweck, J. Müller, A. Rosch, C. Pfleiderer, and C. H. Back, "Entropy-limited topological protection of skyrmions," *Science Advances*, vol. 3, no. 9, 2017.

[129] L. Desplat, D. Suess, J.-V. Kim, and R. L. Stamps, "Thermal stability of metastable magnetic skyrmions: Entropic narrowing and significance of internal eigenmodes," *Phys. Rev. B*, vol. 98, p. 134407, Oct 2018.

[130] L. Desplat and J.-V. Kim, "Entropy-reduced Retention Times in Magnetic Memory Elements: A Case of the Meyer-Neldel Compensation Rule," *Phys. Rev. Lett.*, vol. 125, p. 107201, Sep 2020.

[131] D. Weller and A. Moser, "Thermal effect limits in ultrahigh-density magnetic recording," *IEEE Trans. Magn.*, vol. 35, pp. 4423–4439, Nov 1999.

[132] E. Chen, D. Apalkov, Z. Diao, A. Driskill-Smith, D. Druist, D. Lottis, V. Nikitin, X. Tang, S. Watts, S. Wang, S. A. Wolf, A. W. Ghosh, J. W. Lu, S. J. Poon, M. Stan, W. H. Butler, S. Gupta, C. K. A. Mewes, T. Mewes, and P. B. Visscher, "Advances and Future Prospects of Spin-Transfer Torque Random Access Memory," *IEEE Trans. Magn.*, vol. 46, pp. 1873–1878, May 2010.

[133] L. Rózsa, E. Simon, K. Palotás, L. Udvardi, and L. Szunyogh, "Complex magnetic phase diagram and skyrmion lifetime in an ultrathin film from atomistic simulations," *Phys. Rev. B*, vol. 93, p. 024417, Jan 2016.

[134] S. Rohart, J. Miltat, and A. Thiaville, "Path to collapse for an isolated N\'eel skyrmion," *Phys. Rev. B*, vol. 93, p. 214412, Jun 2016.

[135] W. Kang, Y. Huang, C. Zheng, W. Lv, N. Lei, Y. Zhang, X. Zhang, Y. Zhou, and W. Zhao, "Voltage Controlled Magnetic Skyrmion Motion for Racetrack Memory," *Sci. Rep.*, vol. 6, pp. 1–11, Mar 2016.

[136] H. T. Fook, W. L. Gan, and W. S. Lew, "Gateable skyrmion transport via field-induced potential barrier modulation," *Scientific Reports*, vol. 6, no. 1, p. 21099, 2016.

[137] R. Gruber, J. Zázvorka, M. A. Brems, D. R. Rodrigues, T. Dohi, N. Kerber, B. Seng, K. Everschor-Sitte, P. Virnau, and M. Kläui, "Skyrmion pinning energetics in thin film systems," *arXiv*, Jan 2022.

[138] T. Gushi, L. Vila, O. Fruchart, A. Marty, S. Pizzini, J. Vogel, F. Takata, A. Anzai, K. Toko, T. Suemasu, and J.-P. Attané, "Millimeter-sized magnetic domains in perpendicularly magnetized ferrimagnetic Mn4N thin films grown on SrTiO3," *Jpn. J. Appl. Phys.*, vol. 57, p. 120310, Oct 2018.

[139] T. Gushi, M. Jovičević Klug, J. Peña Garcia, S. Ghosh, J.-P. Attané, H. Okuno, O. Fruchart, J. Vogel, T. Suemasu, S. Pizzini, and L. Vila, "Large Current Driven Domain Wall Mobility and Gate Tuning of Coercivity in Ferrimagnetic Mn4N Thin Films," *Nano Lett.*, vol. 19, pp. 8716–8723, Dec 2019.

[140] W. Zhou, C. T. Ma, T. Q. Hartnett, P. V. Balachandran, and S. J. Poon, "Rare-earth-free ferrimagnetic mn4n sub-20 nm thin films as potential high-temperature spintronic material," *AIP Advances*, vol. 11, no. 1, p. 015334, 2021.

[141] F. Büttner, I. Lemesh, M. Schneider, B. Pfau, C. M. Günther, P. Hessing, J. Geilhufe, L. Caretta, D. Engel, B. Krüger, J. Viefhaus, S. Eisebitt, and G. S. D. Beach, "Field-free deterministic ultrafast creation of magnetic skyrmions by spin–orbit torques," *Nature Nanotechnology*, vol. 12, no. 11, pp. 1040–1044, 2017.

[142] COMSOL Multiphysics® v. 5.6. www.comsol.com. COMSOL AB, Stockholm, Sweden.

[143] S. S. P. Parkin, M. Hayashi, and L. Thomas, "Magnetic domain-wall racetrack memory," *Science*, vol. 320, no. 5873, pp. 190–194, 2008.

[144] H. Vakili, Y. Xie, S. Ganguly, and A. W. Ghosh, "Anatomy of nanomagnetic switching at a 3D Topological Insulator PN junction," *arXiv:2110.02641 [cond-mat]*, Nov. 2021. arXiv: 2110.02641.

[145] H. Vakili, S. Ganguly, G. J. de Coster, M. R. Neupane, and A. W. Ghosh, "Low power In Memory Computation with Reciprocal Ferromagnet/Topological Insulator Heterostructures," *arXiv:2203.14389 [cond-mat]*, Mar. 2022. arXiv: 2203.14389.

[146] P. Chi, S. Li, C. Xu, T. Zhang, J. Zhao, Y. Liu, Y. Wang, and Y. Xie, "Prime: A novel processing-in-memory architecture for neural network computation in reram-based main memory," in *2016 ACM/IEEE (ISCA)*, pp. 27–39, 2016.

[147] S. Ghose, A. Boroumand, J. S. Kim, J. Gómez-Luna, and O. Mutlu, "Processing-in-memory: A workload-driven perspective," *IBM Journal of Research and Development*, vol. 63, no. 6, pp. 3:1–3:19, 2019.

[148] X. Fong, Y. Kim, K. Yogendra, D. Fan, A. Sengupta, A. Raghunathan, and K. Roy, "Spin-transfer torque devices for logic and memory: Prospects and perspectives," *IEEE Transactions on Computer-Aided Design of Integrated Circuits and Systems*, vol. 35, no. 1, pp. 1–22, 2016.

[149] A. R. Mellnik, J. S. Lee, A. Richardella, J. L. Grab, P. J. Mintun, M. H. Fischer, A. Vaezi, A. Manchon, E.-A. Kim, N. Samarth, and D. C. Ralph, "Spin-transfer torque generated by a topological insulator," *Nature*, vol. 511, no. 7510, pp. 449–451.

[150] Y. Wang, D. Zhu, Y. Wu, Y. Yang, J. Yu, R. Ramaswamy, R. Mishra, S. Shi, M. Elyasi, K.-L. Teo, Y. Wu, and H. Yang, "Room temperature magnetization switching in topological insulator-ferromagnet heterostructures by spin-orbit torques," *Nat Commun*, vol. 8, no. 1, p. 1364.

[151] J. Han, A. Richardella, S. A. Siddiqui, J. Finley, N. Samarth, and L. Liu, "Room-temperature spin-orbit torque switching induced by a topological insulator," *Phys. Rev. Lett.*, vol. 119, no. 7, p. 077702.

[152] J. Han and L. Liu, "Topological insulators for efficient spin–orbit torques," *APL Materials*, vol. 9, no. 6, p. 060901.

[153] Y. G. Semenov, X. Duan, and K. W. Kim, "Electrically controlled magnetization in ferromagnet-topological insulator heterostructures," *Phys. Rev. B*, vol. 86, no. 16, p. 161406.

[154] T. Taniyama, "Electric-field control of magnetism via strain transfer across ferromagnetic/ferroelectric interfaces," *J. Phys.: Condens. Matter*, vol. 27, no. 50, p. 504001.

[155] K. Wang, M. M. Elahi, L. Wang, K. M. M. Habib, T. Taniguchi, K. Watanabe, J. Hone, A. W. Ghosh, G.-H. Lee, and P. Kim, "Graphene transistor based on tunable dirac fermion optics," *Proceedings of the National Academy of Sciences*, vol. 116, no. 14, pp. 6575–6579, 2019.

[156] C. A. F. Vaz, F. J. Walker, C. H. Ahn, and S. Ismail-Beigi, “Intrinsic interfacial phenomena in manganite heterostructures,” *J. Phys.: Condens. Matter*, vol. 27, no. 12, p. 123001.

[157] M. Trassin, “Low energy consumption spintronics using multiferroic heterostructures,” *J. Phys.: Condens. Matter*, vol. 28, no. 3, p. 033001.

[158] P. Manchanda, U. Singh, S. Adenwalla, A. Kashyap, and R. Skomski, “Strain and stress in magnetoelastic co–pt multilayers,” *IEEE Transactions on Magnetics*, vol. 50, no. 11, pp. 1–4, 2014.

[159] E. De Ranieri, P. E. Roy, D. Fang, E. K. Vehsthedt, A. C. Irvine, D. Heiss, A. Casiraghi, R. P. Campion, B. L. Gallagher, T. Jungwirth, and J. Wunderlich, “Piezoelectric control of the mobility of a domain wall driven by adiabatic and non-adiabatic torques,” *Nature Mater*, vol. 12, no. 9, pp. 808–814.

[160] R. Verba, I. Lisenkov, I. Krivorotov, V. Tiberkevich, and A. Slavin, “Nonreciprocal surface acoustic waves in multilayers with magnetoelastic and interfacial dzyaloshinskii-moriya interactions,” *Phys. Rev. Applied*, vol. 9, p. 064014, Jun 2018.

[161] S. Bandyopadhyay, J. Atulasimha, and A. Barman, “Magnetic straintronics: Manipulating the magnetization of magnetostrictive nanomagnets with strain for energy-efficient applications,” *Applied Physics Reviews*, vol. 8, no. 4, p. 041323, 2021.

[162] Y. G. Semenov, X. Duan, and K. W. Kim, “Electrically controlled magnetization in ferromagnet-topological insulator heterostructures,” *Phys. Rev. B*, vol. 86, p. 161406, Oct 2012.

[163] X. Duan, X.-L. Li, X. Li, Y. G. Semenov, and K. W. Kim, “Highly efficient conductance control in a topological insulator based magnetoelectric transistor,” *Journal of Applied Physics*, vol. 118, no. 22, p. 224502, 2015.

[164] S. Manipatruni, D. E. Nikonov, C.-C. Lin, B. Prasad, Y.-L. Huang, A. R. Damodaran, Z. Chen, R. Ramesh, and I. A. Young, “Voltage control of unidirectional anisotropy in ferromagnet-multiferroic system,” *Science Advances*, vol. 4, no. 11, p. eaat4229, 2018.

[165] C.-X. Liu, X.-L. Qi, H. Zhang, X. Dai, Z. Fang, and S.-C. Zhang, "Model hamiltonian for topological insulators," *Phys. Rev. B*, vol. 82, p. 045122, Jul 2010.

[166] M. Götte, T. Paananen, G. Reiss, and T. Dahm, "Tunneling magnetoresistance devices based on topological insulators: Ferromagnet–insulator–topological-insulator junctions employing bi_2se_3," *Phys. Rev. Applied*, vol. 2, p. 054010, Nov 2014.

[167] P. Sengupta, T. Kubis, Y. Tan, and G. Klimeck, "Proximity induced ferromagnetism, superconductivity, and finite-size effects on the surface states of topological insulator nanostructures," *Journal of Applied Physics*, vol. 117, no. 4, p. 044304, 2015.

[168] J. Liu and T. Hesjedal, "Magnetic topological insulator heterostructures: A review," *Advanced Materials*, p. 2102427.

[169] S. Datta, *Lessons from Nanoelectronics.* WORLD SCIENTIFIC, 2012.

[170] A. Ghosh, *Nanoelectronics - a Molecular View.* WORLD SCIENTIFIC, 2016.

[171] A. Manchon, R. Matsumoto, H. Jaffres, and J. Grollier, "Spin transfer torque with spin diffusion in magnetic tunnel junctions," *Phys. Rev. B*, vol. 86, p. 060404, Aug 2012.

[172] P. B. Ndiaye, C. A. Akosa, M. H. Fischer, A. Vaezi, E.-A. Kim, and A. Manchon, "Dirac spin-orbit torques and charge pumping at the surface of topological insulators," *Phys. Rev. B*, vol. 96, p. 014408, Jul 2017.

[173] A. K. Reza, X. Fong, Z. A. Azim, and K. Roy, "Modeling and evaluation of topological insulator/ferromagnet heterostructure-based memory," *IEEE Transactions on Electron Devices*, vol. 63, no. 3, pp. 1359–1367, 2016.

[174] J. Slonczewski, "Current-driven excitation of magnetic multilayers," *Journal of Magnetism and Magnetic Materials*, vol. 159, no. 1, pp. L1–L7, 1996.

[175] H. Vakili, Y. Xie, S. Ganguly, and A. W. Ghosh, "Anatomy of nanomagnetic switching at a 3D Topological Insulator PN junction," *arXiv:2110.02641 [cond-mat]*, Nov. 2021. arXiv: 2110.02641.

[176] J. Z. Sun, "Spin-current interaction with a monodomain magnetic body: A model study," *Phys. Rev. B*, vol. 62, pp. 570–578, Jul 2000.

[177] W. H. Butler, T. Mewes, C. K. A. Mewes, P. B. Visscher, W. H. Rippard, S. E. Russek, and R. Heindl, "Switching distributions for perpendicular spin-torque devices within the macrospin approximation," *IEEE Transactions on Magnetics*, vol. 48, no. 12, pp. 4684–4700, 2012.

[178] Z. Li and S. Zhang, "Thermally assisted magnetization reversal in the presence of a spin-transfer torque," *Phys. Rev. B*, vol. 69, p. 134416, Apr 2004.

[179] D. Bedau, H. Liu, J.-J. Bouzaglou, A. D. Kent, J. Z. Sun, J. A. Katine, E. E. Fullerton, and S. Mangin, "Ultrafast spin-transfer switching in spin valve nanopillars with perpendicular anisotropy," *Applied Physics Letters*, vol. 96, no. 2, p. 022514, 2010.

[180] H. Liu, D. Bedau, J. Sun, S. Mangin, E. Fullerton, J. Katine, and A. Kent, "Dynamics of spin torque switching in all-perpendicular spin valve nanopillars," *Journal of Magnetism and Magnetic Materials*, vol. 358-359, pp. 233–258, 2014.

[181] L. Breth, D. Suess, C. Vogler, B. Bergmair, M. Fuger, R. Heer, and H. Brueckl, "Thermal switching field distribution of a single domain particle for field-dependent attempt frequency," *Journal of Applied Physics*, vol. 112, no. 2, p. 023903, 2012.

[182] V. Krizakova, K. Garello, E. Grimaldi, G. S. Kar, and P. Gambardella, "Field-free switching of magnetic tunnel junctions driven by spin–orbit torques at sub-ns timescales," *Applied Physics Letters*, vol. 116, no. 23, p. 232406, 2020.

[183] W. J. Kong, C. H. Wan, X. Wang, B. S. Tao, L. Huang, C. Fang, C. Y. Guo, Y. Guang, M. Irfan, and X. F. Han, "Spin–orbit torque switching in a t-type magnetic configuration with current orthogonal to easy axes," *Nat Commun*, vol. 10, no. 1, p. 233.

[184] Z. Zheng, Y. Zhang, V. Lopez-Dominguez, L. Sánchez-Tejerina, J. Shi, X. Feng, L. Chen, Z. Wang, Z. Zhang, K. Zhang, B. Hong, Y. Xu, Y. Zhang, M. Carpentieri, A. Fert, G. Finocchio, W. Zhao, and P. Khalili Amiri, "Field-free

spin-orbit torque-induced switching of perpendicular magnetization in a ferrimagnetic layer with a vertical composition gradient," *Nat Commun*, vol. 12, no. 1, p. 4555.

[185] K. M. Habib, R. N. Sajjad, and A. W. Ghosh, "Chiral tunneling of topological states: Towards the efficient generation of spin current using spin-momentum locking," *Physical review letters*, vol. 114, no. 17, p. 176801, 2015.

[186] L. Liu, T. Moriyama, D. Ralph, and R. Buhrman, "Spin-torque ferromagnetic resonance induced by the spin hall effect," *Physical review letters*, vol. 106, no. 3, p. 036601, 2011.

[187] L. Liu, C.-F. Pai, Y. Li, H. Tseng, D. Ralph, and R. Buhrman, "Spin-torque switching with the giant spin hall effect of tantalum," *Science*, vol. 336, no. 6081, pp. 555–558, 2012.

[188] B. Gu, I. Sugai, T. Ziman, G. Guo, N. Nagaosa, T. Seki, K. Takanashi, and S. Maekawa, "Surface-assisted spin hall effect in au films with pt impurities," *Physical review letters*, vol. 105, no. 21, p. 216401, 2010.

[189] S. Ganguly, K. Y. Camsari, and A. W. Ghosh, "Analog signal processing using stochastic magnets," *IEEE Access*, vol. 9, pp. 92640–92650, 2021.

[190] K. Y. Camsari, R. Faria, B. M. Sutton, and S. Datta, "Stochastic p-bits for invertible logic," *Phys. Rev. X*, vol. 7, p. 031014, Jul 2017.

[191] S. Hong, V. Diep, S. Datta, and Y. P. Chen, "Modeling potentiometric measurements in topological insulators including parallel channels," *Physical Review B*, vol. 86, no. 8, p. 085131, 2012.

[192] U. Roy, R. Dey, T. Pramanik, B. Ghosh, L. F. Register, and S. K. Banerjee, "Magnetization switching of a metallic nanomagnet via current-induced surface spin-polarization of an underlying topological insulator," *Journal of Applied Physics*, vol. 117, no. 16, p. 163906, 2015.

[193] Y. Xie, Y. Tan, and A. W. Ghosh, "Spintronic signatures of klein tunneling in topological insulators," *Phys. Rev. B*, vol. 96, p. 205151, Nov 2017.

[194] X. Duan, X.-L. Li, Y. G. Semenov, and K. W. Kim, "Nonlinear magnetic dynamics in a nanomagnet–topological insulator heterostructure," *Physical Review B*, vol. 92, no. 11, p. 115429, 2015.

[195] G. Gupta, H. Lin, A. Bansil, M. B. A. Jalil, and G. Liang, "Role of acoustic phonons in bi_2se_3 topological insulator slabs: A quantum transport investigation," *Phys. Rev. B*, vol. 89, p. 245419, Jun 2014.

[196] M. Z. Hasan and C. L. Kane, "Colloquium: Topological insulators," *Rev. Mod. Phys.*, vol. 82, pp. 3045–3067, Nov 2010.

[197] F. Mahfouzi, N. Nagaosa, and B. K. Nikolić, "Spin-to-charge conversion in lateral and vertical topological-insulator/ferromagnet heterostructures with microwave-driven precessing magnetization," *Phys. Rev. B*, vol. 90, p. 115432, Sep 2014.

[198] T. Chiba, S. Takahashi, and G. E. W. Bauer, "Magnetic-proximity-induced magnetoresistance on topological insulators," vol. 95, no. 9, p. 094428.

[199] Y. Tokura, K. Yasuda, and A. Tsukazaki, "Magnetic topological insulators," vol. 1, no. 2, pp. 126–143.